

Diss. ETH No. 19534

**THE USE OF SURFACE WAVES FOR
SITE CHARACTERIZATION AND
SEISMIC HAZARD ANALYSIS**

A dissertation submitted to
ETH ZURICH

for the degree of
DOCTOR OF SCIENCES

presented by
VALERIO POGGI

Laurea in Geologia,
Università degli Studi di Milano
born September 19, 1976
citizen of Italy

accepted on the recommendation of

Prof. Dr. Domenico Giardini, examiner

Dr. Donat Fäh, co-examiner

Dr. Pierre-Yves Bard, co-examiner

2011

a Sonia.

Contents

Riassunto	1
Abstract	3
Introduction	5
1 Rayleigh ellipticity from F-K analysis	9
1.1 Introduction	10
1.2 Method	12
1.2.1 Basic array processing	13
1.2.2 Classical beamforming	15
1.2.3 High resolution beamforming	17
1.2.4 Noise filtering and diagonal loading	22
1.2.5 Three component f - k spectrum	23
1.2.6 Rayleigh ellipticity function evaluation	23
1.2.7 Resolution capabilities	26
1.3 Results	29
1.3.1 Synthetic datasets	31
1.3.2 Model M2.1	32
1.3.3 Model M10.2	33
1.3.4 Model M11.2	36
1.3.5 Real test case: the town of Visp	36
1.3.6 Visp Array 01	38
1.3.7 Visp Array 02	39
1.4 Discussion and conclusions	40
2 Ellipticity in microzonation	45
2.1 Introduction	46
2.2 Geological setting	49
2.3 Ambient noise measurements	51

2.3.1	General set-up and single station measurements	51
2.3.2	The array survey	51
2.3.3	Error estimation in orienting the horizontal components	52
2.4	Single station processing	53
2.4.1	Classical H/V ratio	53
2.4.2	H/V ratios using the continuous wavelet transform	54
2.4.3	Assessing the SH-wave contribution of the Lucerne area	58
2.4.4	Ellipticity f_0 map	59
2.5	Array processing	60
2.5.1	Three-component frequency-wavenumber analysis	60
2.5.2	Rayleigh ellipticity function from array analysis	65
2.6	Inversion of dispersion curves	67
2.6.1	The inversion scheme	68
2.6.2	Velocity profile in gradient form	71
2.7	Rayleigh wave ellipticity inversion	71
2.7.1	SBB station: inverting the whole ellipticity function	71
2.7.2	Global inversion of ellipticity peaks	74
2.7.3	Comparison with the simplified f_0 -resonance approach	76
2.8	Frequency-dependent amplification model	78
2.8.1	Pseudo-3D modeling of amplification	78
2.8.2	Using the SH-wave transfer function	81
2.8.3	Comparing the ellipticity peak to SH-wave f_0	81
2.8.4	Using the quarter-wavelength amplification	82
2.9	Discussion and conclusions	85
3	T-f-k analysis using wavelet transform	89
3.1	Introduction	90
3.2	Method	93
3.2.1	Multiple shot triggering of continuous records	93
3.2.2	Travel-time covariance matrix estimation	94
3.2.3	Covariance matrix stacking and phase-averaging	97
3.2.4	Note on amplitude normalization	99
3.2.5	The f-v-t power spectrum and grid search	100
3.3	The raised-cosine mother wavelet	101
3.4	Results	104
3.4.1	The synthetic dataset	104
3.4.2	Testing real data: Lucerne (Switzerland)	105
3.5	Discussion and conclusions	109

4 A Reference S-wave Velocity model	113
4.1 Introduction	114
4.2 Selection of V_s velocity profiles for specific station locations . .	117
4.3 The quarter-wavelength velocity approximation	119
4.4 Obtaining site specific amplification	122
4.5 Quarter-wavelength velocity versus computed amplification . . .	127
4.6 Inverting for a gradient model	131
4.7 Comparison with previous reference profiles	133
4.8 Reference amplification model	135
4.9 Back-computation of the amplification functions	139
4.10 Summary and conclusions	141
4.11 Data and resources	143
Conclusions and Outlook	145
Figures and Tables	149
Appendix	153
Bibliography	159
Curriculum Vitae	171
Acknowledgments	175

Riassunto

La pericolosità sismica è tradizionalmente definita attraverso la valutazione probabilistica del moto sismico atteso, per un prefissato periodo di ritorno, rispetto a un sito roccioso di riferimento. Per un sito di diverse caratteristiche, questa stima deve essere corretta per la funzione di risposta sismica locale, o spettro di amplificazione relativo. Al fine di calcolare correttamente la funzione di risposta è però necessario un adeguato grado conoscenza delle caratteristiche strutturali dell'area. Il livello di scuotimento in superficie, infatti, è fortemente controllato dalle proprietà geofisiche delle prime decine/centinaia di metri del suolo in esame. Purtroppo, a causa del notevole investimento di risorse richiesto, questa informazione non è sempre sufficientemente completa. Il perfezionamento dei criteri di stima dei parametri geofisici del suolo - principalmente la velocità delle onde di taglio in funzione della profondità - è quindi un argomento chiave nell'ambito della valutazione della risposta sismica locale.

Lo scopo principale di questa tesi è lo sviluppo e l'ottimizzazione di tecniche, nuove ed esistenti, che permettano la diminuzione delle incertezze nel tracciamento dello scenario di risposta sismica locale. In particolare, questo studio si concentra sulle tecniche di analisi delle onde superficiali, le cui caratteristiche dispersive e di polarizzazione permettono la stima dei parametri geofisici del suolo attraverso procedure d'inversione non lineare. Nel corso della trattazione, saranno introdotte diverse nuove metodologie di studio del campo d'onda microsismico, sia questo di origine naturale (il cosiddetto rumore ambientale), sia esso generato attraverso sorgenti artificiali. L'utilizzo combinato di tali sorgenti permette l'esame delle onde superficiali su un ampio campo di frequenze, sia per il modo fondamentale che per i modi superiori.

Nella prima parte sarà introdotto un metodo innovativo per l'analisi della funzione di ellitticità delle onde di Rayleigh. Tale metodo si basa sul calcolo della trasformata frequenza-numero d'onda di registrazioni sincrone tricomponente. Il metodo è particolarmente utile in campagne di acquisizione di rumore ambientale perché permette di ottenere, congiuntamente alle caratteristiche di dispersione, anche la corrispondente informazione di polarizzazione. Il princi-

pale vantaggio consiste nel poter separare la funzione di ellitticità per i diversi modi di propagazione, qualora sufficientemente energetici. Tale metodo è stato testato con successo in un esperimento di microzonazione sismica condotto nella città di Lucerna. Qui, l'utilizzo della funzione di ellitticità ha permesso d'incrementare la risoluzione sulle caratteristiche geometriche del basamento roccioso, perfezionando quindi il grado di conoscenza del modello tridimensionale di velocità. Questo ha permesso conseguentemente una valutazione più accurata dei livelli di amplificazione sismica attesi per l'area.

L'utilizzo del solo rumore ambientale non è però sufficiente per la caratterizzazione delle porzioni più superficiali del suolo, la cui conoscenza è di contro fondamentale per la corretta definizione della funzione di risposta locale. Ad alte frequenze, infatti, lo scarso contenuto energetico delle sorgenti naturali e i fenomeni di attenuazione anelastica rendono difficoltoso lo sviluppo di un campo d'onda coerente. Per ovviare a questo inconveniente è quindi necessario procedere tramite l'utilizzo di sorgenti artificiali. E' qui presentato un nuovo metodo di analisi delle onde superficiali in esperimenti di sismica attiva, basato sulla trasformata tempo-frequenza. A differenza delle tecniche classiche di acquisizione, il metodo proposto si dimostra particolarmente vantaggioso con stazioni sismologiche e registrazioni continue. Tale approccio è perciò utile in campagne di acquisizione miste, dove l'utilizzo combinato di sorgenti attive e passive consente un più ampio campo di risoluzione sui profili di velocità sismiche, migliorando quindi l'attendibilità nella stima della risposta locale.

E' infine proposto un metodo per la definizione del profilo sismico di riferimento su roccia da utilizzare in relazioni di calcolo dello scuotimento atteso. Il metodo si basa sul confronto, per determinati siti campione, tra velocità medie delle onde di taglio e funzioni di amplificazione empiriche ottenute attraverso modellazione spettrale di eventi sismici. I profili sismici di *input* provengono sia da campagne di acquisizione di rumore ambientale che di sismica attiva. Le velocità medie sono calcolate in funzione della lunghezza d'onda in esame. Questo consente il confronto delle stime di velocità con le funzioni di amplificazione su bande di frequenza discrete. Oltre a produrre un profilo di riferimento *standard* su roccia, il metodo proposto ha permesso di ottenere un insieme di coefficienti utili per ricostruire empiricamente le caratteristiche di amplificazione locale di un qualunque sito roccioso per cui una stima delle velocità medie sia disponibile.

Abstract

Standard approaches to evaluate seismic hazard rely on the evaluation of the expected ground motion with respect to a generic rock site condition. For a sediment site, such estimate has to be corrected for the local seismic response, or the relative amplification spectrum. In order to correctly compute the seismic response, an adequate level of knowledge of the structural characteristics for the site area is necessary. As a matter of fact, the final ground motion is highly controlled by the geophysical properties of the first tens to hundreds of meters of the soil. The available level of knowledge, however, is often insufficient because of the considerable investments required for measurements. Cost efficient methods to estimate soil parameters - mainly shear wave velocity as a function of depth - are therefore the major issues in local seismic response evaluation and site-specific seismic hazard assessment.

The main goal of this thesis is the development and optimization of new and existing techniques to reduce the uncertainty level in the definition of the local seismic response. In particular, this study focuses on surface wave analysis techniques, whose dispersion and polarization features represent a formidable constraint in obtaining the geophysical parameters using non-linear inversion procedures. New methods for analyzing ambient vibration and artificially generated wave-fields are introduced. Combining source types has the advantage of exciting surface waves in a broad range of frequencies, both for the fundamental and the higher modes.

In the first section, a new method to analyze Rayleigh wave ellipticity is presented. The method is based on the frequency-wavenumber transform of three-component synchronous recordings from an array of stations. Such an approach is suitable for ambient noise processing, because it allows the retrieval of dispersion functions and the corresponding polarization information simultaneously. In particular, the main advantage is the capability of separating the contribution of the different modes of propagation, in the case where they are sufficiently energetic. The proposed method has been successfully tested in a microzonation experiment in the city of Lucerne. Using the ellipticity

function increases the resolution on the geometry of the bedrock interface, therefore improving the level of knowledge for a three-dimensional seismic velocity model. This consequently results in a more reliable estimation of the seismic amplification in the study area.

The sole use of ambient noise is, however, insufficient to characterize the shallower part of the soil profile, whose knowledge is fundamental to decrease the uncertainty in the velocity profile. At high frequency, the low energy content of natural sources, together with anelastic attenuation, prevents the development of a coherent wave-field. It is therefore necessary to use artificial sources of controlled energetic content in order to excite energetic high-frequency wave-fields. A new approach for surface wave analysis of active seismic surveying is therefore developed, which is based on time-frequency analysis. With respect to the classic acquisition procedures, the proposed method is convenient in the use with seismological stations and continuous recordings as it does not need a common trigger. The advantage of such a method is in mixed acquisition surveys, where the combined use of active and passive sources allows an optimized depth-resolution range of the seismic velocity profiles. Consequently, the reliability of local seismic response can be improved.

Finally a method for the definition of the reference rock velocity profile of a stochastic ground motion prediction equation is introduced. Such method relies on the comparison between measurements of average shear wave velocity at recording sites and empirical amplification functions from spectral modeling of earthquakes. The input velocity profiles are derived from ambient noise processing and active seismic surveys. The profiles are described in terms of quarter-wavelength velocity as a function of frequency. This allows the comparison of quarter-wavelength velocities with the local amplification functions for a number of discrete frequencies. Together with the definition of a reference rock profile, the proposed approach gives us the possibility to define empirical local amplification as function of the quarter-wavelength velocity for any site for which a shear-wave velocity profile is available.

Introduction

It is widely accepted that the computation of seismic hazard over large areas cannot be conducted without an adequate knowledge of the specific seismic response at a local scale. For a particular site, the amplitude and duration of the ground motion experienced during an earthquake can be significantly modified by local effects, such as focusing and de-focusing of the seismic wave-field, multiple resonance of trapped waves and the amplification of energy induced by a contrast of seismic velocities at depth. In fact, during earthquakes, the effect of local amplification can be comparable with the differences in the hazard estimate between distant regions.

The definition of site-specific hazard is therefore needed for two reasons: firstly because it allows the assessment of more realistic ground-motion estimates. Secondly, it gives the possibility of fine-tuning the hazard at a local scale. This will ultimately lead to a decrease of the uncertainties in seismic hazard computations. It is well accepted that without the knowledge of the local soil condition, ground motion recordings and derived attenuation models are not capable of their full potential. In order to reduce uncertainties in regional ground motion prediction equations (GMPEs), recordings at seismic stations need to be related to shear-wave velocity profiles, and a reference velocity profile has to be defined for seismic hazard maps and site specific uniform hazard spectra.

The correct definition of local response over a particular area relies on an accurate knowledge of soil properties. Unfortunately, a lack of such information is the general situation in Switzerland and Europe, and improvement is hence a major challenge in site-specific seismic hazard assessment. The target of this PhD thesis is therefore the development and optimization of new and existing geophysical methods for site characterization, to derive a generic rock model for Switzerland, and empirical amplification functions. The final goal is to reduce the uncertainties in the seismic response and, consequently, in the final seismic hazard estimate for specific sites.

Geophysical site characterization

Nowadays a variety of approaches to model local site effects exist. The most simple use geological and/or geotechnical classification to group areas of similar expected seismic response. More complicated approaches rely on measuring (directly or indirectly) the geophysical properties of soils, in order to numerically model the amplification function.

If only linear soil response is considered, the most relevant parameters for site characterization are the seismic velocity of body waves (V_p and V_s), the density (ρ) and the quality factors (Q_p and Q_s). The way these parameters are distributed with depth controls the amplification of ground-motion during an earthquake. Shear wave velocity, in particular, is the most important material property driving the amplification phenomena. Shear wave velocity profiles are thus needed for microzonation studies and for the interpretation of recorded earthquake ground motion.

Estimates of soil properties can be obtained by direct in-situ geophysical measurements, such as reflection/refraction seismic, surface-wave measurements, down-hole and cross-hole techniques, or conversely using indirect proxies. Direct investigation methods have high resolution, but are generally expensive. In particular, techniques based on the use of explosion sources are rarely used in densely populated environments, such as urban areas. Nowadays, an increasing interest is therefore in the development of geophysical methods based on passive acquisition of ambient vibrations and micro-tremors. The broadband nature of ambient vibrations leads to a high-resolving power for passive seismic techniques; from the upper meters of soil down to a hundred meters. It is therefore particularly challenging in modern microzonation to use a combination of all these methodologies.

The use of proxies allows the characterization of a site by using a single parameter. The most common proxy for classifying sites for seismic amplification prediction is most probably the travel-time average velocity over the first 30m (V_{s30}), as prescribed by NEHRP (National Earthquake Hazard Reduction Program). V_{s30} is historically derived from the practical limitation of assessing the velocity structure using boreholes, generally at no more than about 30m depth. The large availability of such measurements imposed it as a standard de-facto for geotechnical site characterization.

The main advantage in using V_{s30} is the possibility in linking it to geological and geotechnical maps or to other types of measurements such as SPT (Standard Penetration Test) and CPT (Cone Penetration Test). Due to its simplicity, V_{s30} classification is nowadays prescribed in most buildings codes,

like the Swiss SIA261 (Action on structures, 2001) and the Eurocode 8 (CEN, 2004). Nevertheless, the scientific community is well aware of the limitations of using such an approximation. It is well known that in assessing local amplification, the low frequency content is not well represented by V_{s30} . V_{s30} will not be sufficient in future hazard products because it cannot be related to frequency dependent amplification of the seismic wave.

Seismic amplification functions

As underlined by the analysis of past destructive earthquakes (e.g. Mexico 1985, $M_L = 8.1$; Loma Prieta 1989, $M_L = 7.1$; Kobe 1995, $M_L = 7.2$), strong amplification of the seismic wave-field can be induced the presence of particular geological soil conditions. Consequently, the estimation of ground motion amplification is one of the key elements in defining the seismic hazard in earthquake prone areas.

Seismic amplification can be described by a frequency-dependent local amplification function. Amplification functions can be derived empirically, by direct measurements, or by modeling. All methods need to define a reference rock site. The choice of the reference to be used, however, is not trivial. In most cases a station on outcropping bedrock is used, where no influence of the soft sediments is present. In some cases a reference station is available in a borehole at the sediment bedrock interface.

Modeling of amplification functions is possible only if a sufficiently accurate velocity profile is available. Modeling can be done with different schemes, resolution and level of accuracy, e.g. using simple analytical solutions, like the one-dimensional SH-wave transfer function, or by means of complex numerical simulation of the full 3D wave-field propagation, such as finite differences or the spectral element methods. All these methods present some advantages and disadvantages.

Thesis outline

In this study I focus on the development of new and existing techniques for seismic site characterization. As previously described, a sufficiently accurate assessment of the seismic velocity structure of a site allows a more realistic prediction of amplification of seismic waves. This thesis will deal with measurement techniques that are based on the analysis of surface waves, whose dispersion and polarization features represent a formidable constraint to retrieve

the velocity profiles using non-linear inversion procedures. In the following I outline the content of the chapters.

In chapter 1, advances in frequency-wavenumber analysis of ambient vibrations will be discussed. A method is presented that allows the estimation of the polarization function of Rayleigh waves (ellipticity) from three-component array analysis of ambient vibration recordings. This approach can retrieve, simultaneously, the dispersion and polarization information for different modes of surface waves. To validate the method, the processing of synthetics as well as real recording datasets is presented.

In chapter 2, I discuss the use of Rayleigh wave ellipticity information to improve the resolution of the bedrock geometry of sedimentary basins in seismic microzonation studies. An example for the city of Lucerne is presented for which I provide, other than the final velocity model, an estimation of the expected seismic amplification using pseudo-3D modeling. Moreover, a simple way to retrieve the relative contribution of PSV and SH waves in the ambient vibration wave-field is presented. The method is based on the comparison between horizontal-to-vertical spectral ratios from different single-station methods.

Chapter 3 introduces an alternative approach for surface wave analysis using active seismic experiments. The technique relies on the continuous wavelet transform to decompose an artificially generated wave-field. It is suitable for use with seismological stations and continuous recordings. An example of a mixed active-passive acquisition survey is presented that demonstrates the advantages of the combined approaches to resolve the high and low frequency part of the dispersion curve of surface waves.

Finally, in chapter 4, I derive the reference velocity profile for the Swiss stochastic ground-motion prediction equation. The profile is obtained from the comparison between average shear-wave velocity profiles from the analysis of surface waves, using both active and passive methods, and empirical amplification functions from the modeling of earthquake spectra. The correlation between these parameters gives us the possibility of establishing a set of calibration coefficients, which are also useful to evaluate the generic amplification at sites with measured velocity profile.

Chapter 1

Estimating Rayleigh wave particle motion from three-component array analysis of ambient vibrations

Published in Geophysical Journal International as:
Poggi, V., and Fäh, D. (2009),
Estimating Rayleigh wave particle motion from three-component array analysis of ambient vibrations, *Geophys. J. Int.*, 180, 251-267

Abstract

Several methods have been proposed in the past years to extract the Rayleigh wave ellipticity from horizontal-to-vertical spectral ratios of single station ambient noise recordings. The disadvantage of this set of techniques is the difficulty in clearly identifying and separating the contribution of higher modes. In most cases, only the fundamental mode of ellipticity can be identified. Moreover, it is generally difficult to correct for the energy of SH and Love waves present in the horizontal components of the ambient vibration wave-field.

We introduce a new methodology to retrieve Rayleigh wave ellipticity using high-resolution frequency-wavenumber array analysis. The technique is applied to the three components of motion and is based on the assumption that an amplitude maximum in the f - k cross-spectrum must represent the true power amplitude of the corresponding signal. In the case of Rayleigh waves, therefore, the ratio between maxima obtained from the horizontal (radial-polarized) and vertical components of motion will also represent the frequency-dependent ellipticity function. Consequently, if we can identify the Rayleigh dispersion curves of several modes on the f - k plane, then the corresponding modal ellipticity patterns can also be separated and extracted.

To test the approach, synthetic and real datasets were processed. In all tested cases, a reliable estimation of segments of the fundamental mode ellipticity was obtained. The identification of higher modes is possible in most cases. The quality of results depends on the selected array geometry and the signal-to-noise ratio, with a major improvement achieved by increasing the number of receivers employed during the survey. An experiment conducted in the town of Visp (Switzerland) allowed the retrieval of portions of ellipticity curves up to the second Rayleigh higher mode, using two concentric circular array configurations of 14 and 11 receivers each.

1.1 Introduction

Ambient noise analysis is an easily implemented and economical set of techniques based on passive acquisition and processing of natural and anthropogenic microtremors. These techniques are commonly employed in microzonation and earthquake engineering studies to quickly obtain reliable information about S-wave velocity profiles [e.g., Tokimatsu, 1997] and soil fundamental frequencies of resonance [e.g., Nakamura, 1989]. Despite their poor resolution in discriminating between small variations in geophysical properties, these methodologies are in some cases preferable to other types of high-

resolution seismic surveys. The low frequency energy content of the ambient noise wavefield allows investigation of deep layers [Yamanaka et al., 1994]. This characteristic is particularly suited to site effect analysis and when it is useful to evaluate, even if coarsely, the soil deposit properties up to or sometimes below the bedrock limit. Moreover, employing passive source techniques is preferable in urban areas or in any situation where invasive procedures, such as drilling and cone penetrometer, must be avoided.

Ambient noise analysis rests on the assumption that the noise wavefield from 0.5 to 20Hz is constituted of surface waves, with a minor but significant contribution from body waves [Li et al., 1984; Horike, 1985]. This assumption has been validated by observation and comparison between field measurements and synthetic tests, however the relative proportion of these waves still remains an open issue. Similarly, it is difficult to evaluate with sufficient accuracy the relative contribution of Love and Rayleigh waves [Köhler et al., 2007], and among these to establish a precise proportion between fundamental and higher modes [for a complete literature review see Bonnefoy-Claudet et al., 2006b]. Asten et al. [2004] and Asten [2006], with a technique titled multi-mode SPAC (MMSPAC), specifically recognizes the possibility of the identification of multiple modes. So far, a general agreement is present on the fact that Love waves are in most cases dominant [Okada, 2003]. Nevertheless, a certain number of site-dependent controlling factors can be listed: type, orientation and spatial distribution of shallow and buried sources, as well as seismic impedance and attenuation values for the investigated site.

The predominant contribution of surface waves in the noise wave-field is the main property on which several techniques based on single and multi-station recording were developed. Among these, the ambient noise horizontal-to-vertical spectral ratio [Nogoshi and Igarashi, 1971] is a simple single-station method that has been widely used in the past years to obtain estimations of the fundamental frequency of resonance of soils (f_0). In case of strong velocity contrast between sediments and bedrock, f_0 is close to the first maximum of the Rayleigh ellipticity fundamental mode, most likely always present in the H/V spectrum [e.g., Lachet and Bard, 1994; Fäh et al., 2003]. The simultaneous presence of Love and body waves in the noise wave-field, other than the interaction and superposition of higher modes, makes the identification of the ellipticity function within spectral ratios ambiguous. In practice, only in certain situations it is possible to separate and extract (with acceptable confidence) the stable portion of that curve. These portions, moreover, can be addressed only to the fundamental mode of propagation, but nothing can be said about higher modes. Several attempts to avoid this problem have

been proposed, e.g., modeling the whole H/V spectrum by mixing some contributions of Love and Rayleigh waves and including higher modes [Arai and Tokimatsu, 2005; Parolai et al., 2005]. This method has the advantage of not requiring any previous separation of wave components. However, it strictly depends on a certain number of assumptions (e.g. source type and distribution) that are difficult to be verified.

In this article we propose a new method to evaluate the Rayleigh-wave modal ellipticity function. We modified a version of the high-resolution frequency-wavenumber analysis proposed by Capon [1969]. Our technique rests on the simple fact that the power spectrum calculated with it preserves, along with the phase information, the amplitude characteristics of the investigated signal [Marzetta, 1983]. Being able to perform this transformation both on the vertical and horizontal radial-polarized directions of motion [Fäh et al., 2008] allows us to reconstruct the signal’s in-plane particle motion. Thus, for Rayleigh waves, the modal ellipticity function can be directly evaluated by performing the H/V spectral ratios between f - k power amplitudes. Such amplitudes correspond to a specific and well-defined mode of propagation.

With synthetic and real datasets, we demonstrate that this method allows us to obtain, at one time and with the same elaboration scheme, key data about Rayleigh waves: phase velocity dispersion curves and ellipticity. A combined inversion, together with Love wave dispersion or other constraints, might help in decreasing the non-uniqueness of the problem and avoiding solutions that are trapped in local minima [Fäh et al., 2008].

1.2 Method

Frequency-wavenumber analysis is a spectral technique based on seismic array recording. Such methods have been widely used in determining earthquake direction, in monitoring nuclear explosions and in estimating wave phase velocity. In particular, high resolution beamforming [Capon, 1969], also known as the maximum likelihood or minimum variance method, is a popular data adaptive and alias-free algorithm for computing the frequency-wavenumber spectrum. Applying this method to ambient noise recordings helps us to understand the general composition of the microseismic wavefield: its wave content, propagation and surface wave dispersion.

Since the vertical component of ground motion is affected only by body and Rayleigh wave propagation phenomena (Love component results in an horizontally polarized wavefield), f - k array processing has been employed extensively

to derive data on Rayleigh wave phase velocity dispersion [Kind et al., 2005; Wathelet, 2005]. Recent improvements [Fäh et al., 2008] allow us to analyse full ground motion (both horizontal and vertical components) to identify and separate the two complementary surface wave contributions. This is done through radial/transversal polarization analysis. In addition, we extended the technique to estimate the signal spectral power content with the goal of evaluating frequency-dependent Rayleigh wave particle motion.

1.2.1 Basic array processing

Let us consider a spatial configuration of n seismic vertical receivers located at coordinates $[x_1 \ x_2 \ \dots \ x_n, \ y_1 \ y_2 \ \dots \ y_n]$. In the simplest case, this sensor array samples a narrowband planar wavefield $a(f)$ that propagates along the surface from a source located at infinite distance (far-field approximation) in direction θ , also defined as the direction of arrival (*DOA*). If no attenuation phenomena are assumed, the frequency dependent wavefield amplitude is constant to $|a(f)|$ at each receiver location. However, each sensor samples the plane wave with a certain phase shift depending on its coordinates, the *DOA*, the analysed frequency f and the wave slowness s . In the frequency domain, the i -esim receiver output can therefore be expressed through its constituents as:

$$u_i(f) = g(f)a(f)e^{-2\pi j f s(\cos(\theta)x_i + \sin(\theta)y_i)} \quad (1.1)$$

or, identically, in terms of wavenumber:

$$\begin{aligned} u_i(f) &= g(f)a(f)e^{-2\pi j |\mathbf{k}|(\cos(\theta)x_i + \sin(\theta)y_i)} \\ &= g(f)a(f)e_i(\mathbf{k}). \end{aligned} \quad (1.2)$$

If we define the *true* signal steering vector as:

$$\mathbf{e}(\mathbf{k}) = [e_1(\mathbf{k}) \ e_2(\mathbf{k}) \ \dots \ e_n(\mathbf{k})]^T \quad (1.3)$$

the receiver output can be expressed in vectorial notation as:

$$\mathbf{u}(f) = g(f)a(f)\mathbf{e}(\mathbf{k}). \quad (1.4)$$

A gain scaling factor $g(f)$ is also included to represent the instrumental amplification of the seismometers. However for simplicity and without any loss

of generality, we can set this parameter equal to unity for each station location. Finally, an additional amount of incoherent noise, not addressable to wave propagation phenomena, should be realistically included as a frequency dependent noise vector $\boldsymbol{\eta}(f)$:

$$\mathbf{u}(f) = a(f)\mathbf{e}(\mathbf{k}) + \boldsymbol{\eta}(f). \quad (1.5)$$

Note that the incoherent noise is not related to the ‘‘ambient noise’’ wavefield, which in this case is the coherent signal to analyze. Such disturbance must be considered the true noise of the system, and should therefore be treated statistically [Strobbia, 2003]. Incoherent noise can be generated from an ensemble of different sources, i.e., non-systematic digitization errors, electrical disturbances or local, uncorrelated micro-vibrations of the ground. Later we will demonstrate how this variable amount of noise can drastically influence the efficiency of beamforming methods.

Under the assumption of uncorrelation between signal and noise, the receiver output vector is then used to estimate the signal cross-correlation (or *covariance*) spectral matrix as:

$$\begin{aligned} \hat{\mathbf{R}}(f) &= E\{\mathbf{u}(f)\mathbf{u}^h(f)\} \\ &= E\{\mathbf{e}(\mathbf{k})a(f)a^h(f)\mathbf{e}^h(\mathbf{k})\} + E\{\boldsymbol{\eta}(f)\boldsymbol{\eta}^h(f)\} \end{aligned} \quad (1.6)$$

where the superscript h denotes conjugate (Hermitian) transpose and E stands for expectation. Note that the products between signal and noise are suppressed because of the uncorrelation. In practice, the expected value is obtained from an average between several cross-correlation snapshots of successive time-windows (block averaging).

At a specific frequency, we can assume the noise of the system to be a zero mean Gaussian process with variance $\sigma^2(f)$. Therefore, for a stationary signal the equation 1.6 simplifies to:

$$\hat{\mathbf{R}}(f) = \mathbf{e}(\mathbf{k})|a(f)|^2\mathbf{e}^h(\mathbf{k}) + \sigma^2(f)\hat{\mathbf{I}} \quad (1.7)$$

where $\hat{\mathbf{I}}$ is the identity matrix. From the cross-correlation matrix, the *total array power output* $P(f)$ can then be calculated by summing its elements:

$$P(f) = [\mathbf{1}]^h\hat{\mathbf{R}}(f)[\mathbf{1}] \quad (1.8)$$

where $[\mathbf{1}]$ is a vector of n elements equal to 1.

1.2.2 Classical beamforming

In classical beamforming techniques [Lacoss et al., 1969], the total array power output is weighted with a filter vector $\mathbf{w}(\mathbf{k})$ equal to the *presumed* signal steering vector $\mathbf{e}_p(\mathbf{k})$ divided by the number of sensors:

$$P(f, \mathbf{k}) = \mathbf{w}^h(\mathbf{k}) \hat{\mathbf{R}}(f) \mathbf{w}(\mathbf{k}), \quad (1.9)$$

$$\mathbf{w}(\mathbf{k}) = \frac{\mathbf{e}_p(\mathbf{k})}{n}. \quad (1.10)$$

The true signal steering vector is initially unknown, as are the direction of propagation and the velocity of the investigated wave. However, identifying the correct value is straightforward; a direct grid search over s and θ (or identically over k_x and k_y) can be performed. The presumed steering vector is thus rebuilt every time for each combination of parameters. As a consequence, a maximum in the total array output function is achieved when the presumed and the true steering direction match ($\mathbf{e}_p(\mathbf{k}) = \mathbf{e}(\mathbf{k})$). In such case is:

$$\mathbf{e}_p^h(\mathbf{k}) \mathbf{e}(\mathbf{k}) = \mathbf{e}^h(\mathbf{k}) \mathbf{e}_p(\mathbf{k}) = n \quad (1.11)$$

and then for simple substitution in equation 1.7, 1.9 and 1.10:

$$\begin{aligned} P(f, \mathbf{k}) &= \frac{1}{n^2} \{n|a(f)|^2n + \sigma^2(f)n\} \\ &= |a(f)|^2 + \frac{\sigma^2(f)}{n}. \end{aligned} \quad (1.12)$$

Thus, the array power output corresponds to the true energy of the signal, plus an amount of distortion introduced by the noise variance (Fig. 1.1 a).

As shown, this approach preserves the amplitude characteristics in cases of minimum or null noise variance (or a large number of receivers) and when a perfect match holds between the true and the presumed steering vectors. Unfortunately, it is not robust enough to sufficiently minimize the power output in a situation of progressive steering vectors mismatch. That case results in

a generally poor resolution and can be summarized by analysis of the theoretical array response or *beampattern*. This represents the array power output for a signal of unitary amplitude and zero phase (e.g. the case of a vertically incident plane wave):

$$B(\mathbf{k}) = \mathbf{w}^h(\mathbf{k})[\hat{\mathbf{1}}]\mathbf{w}(\mathbf{k}). \quad (1.13)$$

Here $[\hat{\mathbf{1}}]$ is a square matrix of $n \cdot n$ elements equal to 1. The array power output for any generic wavefield can be obtained by convolving the theoretical response with the signal impulse in the wavenumber domain [Wathelet, 2005]. It is therefore evident that the shape of the beampattern function will be the primary factor in controlling the resolution.

Furthermore, any assumption of a wavefield constituted by only a single plane wave cannot realistically represent ambient noise phenomena. In real situations multiple signals propagate simultaneously, impinge the array from different directions and overlap one another. Let us consider, as an example, the propagation of M surface wave higher modes:

$$\mathbf{u}(f) = \sum_{i=1}^M a_i(f)\mathbf{e}(\mathbf{k}_i) + \boldsymbol{\eta}(f). \quad (1.14)$$

Following from equation 1.6 and under the assumption that the noise and the signals are uncorrelated, the cross-correlation matrix has the form:

$$\hat{\mathbf{R}}(f) = E \left\{ \sum_{i=1}^M \sum_{l=1}^M \mathbf{e}(\mathbf{k}_i) a_i(f) a_l^h(f) \mathbf{e}^h(\mathbf{k}_l) \right\} + \sigma^2(f) \hat{\mathbf{I}} \quad (1.15)$$

However, in case of ambient noise, we can assume the signals are non-stationary over long durations. Consequently, different signals ($i \neq l$) can be reasonably considered to be uncorrelated over successive time window snapshots. In such a case, the mixed products of the previous equation tend to vanish by means of the expectation procedure. Therefore the cross-correlation matrix simplifies to:

$$\hat{\mathbf{R}}(f) \simeq \sum_{i=1}^M \mathbf{e}(\mathbf{k}_i) |a_i(f)|^2 \mathbf{e}^h(\mathbf{k}_i) + \sigma^2(f) \hat{\mathbf{I}} \quad (1.16)$$

It is easy to demonstrate that the total power output is distorted by the reciprocal interference between wavefields as well as noise. As in the previous

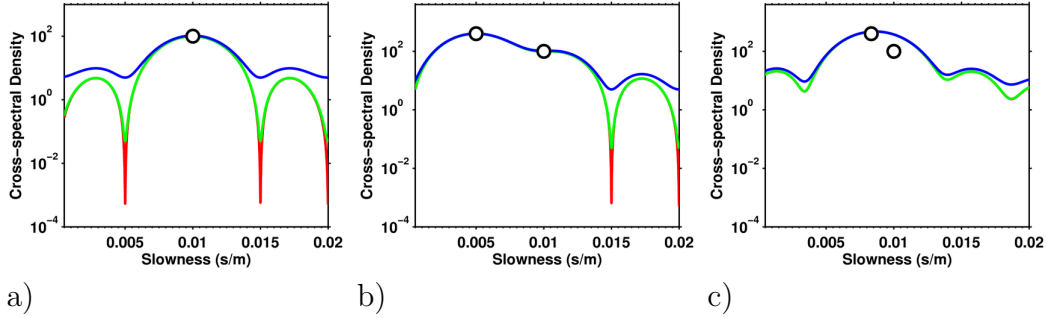


Figure 1.1: Signal identification using classical beamforming: a linear array of 20 receivers with spacing of $5m$ is employed. The power output is calculated for a frequency of $2Hz$ and different noise variances are included for comparison (0.1 in red, 1 in green and 10 in blue). In case a) a single signal with velocity of $100m/s$ and amplitude 10 is analysed. In case b) two signals with velocities of $100m/s$ and $200m/s$ and amplitudes 10 and 20 are considered. In case c) the two signals of b) now have a velocity of $100m/s$ and $120m/s$ respectively. True amplitudes are also presented for comparison (black circles).

example, once the steering vector of the signal of interest is identified (e.g. $\mathbf{e}_p(\mathbf{k}) = \mathbf{e}(\mathbf{k}_1)$), the corresponding amplitude will deteriorate due to the M interfering steering vectors:

$$\begin{aligned}
 P(f, \mathbf{k}_1) &\simeq |a_1(f)|^2 \\
 &+ \sum_{i=2}^M \frac{|a_i(f)|^2}{n^2} \mathbf{e}^h(\mathbf{k}_1) \mathbf{e}(\mathbf{k}_i) \mathbf{e}^h(\mathbf{k}_i) \mathbf{e}(\mathbf{k}_1) \\
 &+ \frac{\sigma^2(f)}{n}.
 \end{aligned} \tag{1.17}$$

Nevertheless, this amplitude approximation has been experimentally demonstrated to be valid if the signals are not too similar (in terms of *DOA* and slowness, e.g. Fig. 1.1 b and c) and the number of receivers is sufficiently large to minimize the beampattern geometry effect [Asten and Henstridge, 1984]. Note as well that the noise variance influences the total power output $P(f, \mathbf{k})$ as a positive amplitude shift of the power spectrum only. Its shape will remain unmodified.

1.2.3 High resolution beamforming

In high resolution beamforming, the target is to weight the array power output with a *data adaptive* filter vector $\mathbf{w}(\mathbf{k})$. This minimizes distortions induced by mismatches between the true and the presumed steering vector, and at

the same time minimizes the influence of uncorrelated noise [Capon, 1969; Marzetta, 1983]. However, the procedure should not affect the signal correlation in the final result. In practice we want to solve the following quadratic minimization problem:

$$P(f, \mathbf{k}) = \min_{\mathbf{w}} \left\{ \mathbf{w}^h(\mathbf{k}) \hat{\mathbf{R}}(f) \mathbf{w}(\mathbf{k}) \right\} \quad (1.18)$$

subject to the amplitude constraint:

$$\mathbf{w}^h(\mathbf{k}) \mathbf{e}_p(\mathbf{k}) = 1. \quad (1.19)$$

The minimization problem can be solved using the Lagrange multiplier in this form:

$$\mathbf{w}(\mathbf{k}) = \frac{\hat{\mathbf{R}}^{-1}(f) \mathbf{e}_p(\mathbf{k})}{\mathbf{e}_p^h(\mathbf{k}) \hat{\mathbf{R}}^{-1}(f) \mathbf{e}_p(\mathbf{k})}. \quad (1.20)$$

Consequently, the weighted power output 1.18 will be expressed for substitution and resulting simplification as:

$$P(f, \mathbf{k}) = \frac{1}{\mathbf{e}_p^h(\mathbf{k}) \hat{\mathbf{R}}^{-1}(f) \mathbf{e}_p(\mathbf{k})}. \quad (1.21)$$

As in the case of classical beamforming, the true signal steering vector can be found with a simple grid search over s and θ . In addition, we now want to evaluate to what degree the total power output can deviate from the true energy of the signal when a perfect match occurs between the true and presumed steering vector. To analyse this we use a singular value decomposition. The steering vector can be factorized into its orthonormal basis ($\hat{\mathbf{J}}$ and L) and singular values (\mathbf{K}) as:

$$\mathbf{e}(\mathbf{k}) = \hat{\mathbf{J}} \mathbf{K} L^h \quad (1.22)$$

where $\hat{\mathbf{J}}$ is a $n \cdot n$ orthogonal matrix containing the basis vector directions of $\mathbf{e}(\mathbf{k})$ and L is a scalar with the only admissible values ± 1 . The decomposition of a steering vector always produces one unique singular value. Consequently \mathbf{K} is a column vector with all elements, except the first, equal to 0. Similarly,

for the steering vector cross-product, an Hermitian positive semidefinite matrix, it is always possible to find an eigen-decomposition that satisfies:

$$\mathbf{e}(\mathbf{k})\mathbf{e}^h(\mathbf{k}) = \hat{\mathbf{J}}\mathbf{K}L^hL\mathbf{K}^h\hat{\mathbf{J}}^h = \hat{\mathbf{J}}\hat{\mathbf{S}}\hat{\mathbf{J}}^h \quad (1.23)$$

where $\hat{\mathbf{S}}$ is the $n \cdot n$ diagonal eigenvalue matrix. Summarizing, the following relations are then valid:

$$\begin{aligned} L &= \pm 1, \\ \mathbf{K}\mathbf{K}^h &= \hat{\mathbf{S}}, \\ \hat{\mathbf{J}}\hat{\mathbf{J}}^h &= \hat{\mathbf{J}}^h\hat{\mathbf{J}} = \hat{\mathbf{I}}. \end{aligned} \quad (1.24)$$

Given the decomposition in 1.23, we have the property:

$$\text{tr}(\mathbf{e}(\mathbf{k})\mathbf{e}^h(\mathbf{k})) = \text{tr}(\hat{\mathbf{S}}) = \text{tr}(\mathbf{K}\mathbf{K}^h) = n \quad (1.25)$$

where tr stands for matrix trace. Therefore the unique singular value in \mathbf{K} will be exactly \sqrt{n} .

The inverse of the cross-correlation matrix of equation 1.7 can then be expressed for substitution as:

$$\hat{\mathbf{R}}^{-1}(f) = \left\{ |a(f)|^2 \hat{\mathbf{J}}\hat{\mathbf{S}}\hat{\mathbf{J}}^h + \sigma^2(f)\hat{\mathbf{I}} \right\}^{-1}, \quad (1.26)$$

$$\hat{\mathbf{R}}^{-1}(f) = \frac{1}{|a(f)|^2} \left\{ \hat{\mathbf{J}}\hat{\mathbf{S}}\hat{\mathbf{J}}^h + \frac{\sigma^2(f)}{|a(f)|^2} \hat{\mathbf{I}} \right\}^{-1}. \quad (1.27)$$

Because $\hat{\mathbf{J}}$ is orthogonal and consequently $\hat{\mathbf{J}}\hat{\mathbf{J}}^h = \hat{\mathbf{I}}$, it is possible to write:

$$\hat{\mathbf{R}}^{-1}(f) = \frac{1}{|a(f)|^2} \left\{ \hat{\mathbf{J}}\hat{\mathbf{S}}\hat{\mathbf{J}}^h + \hat{\mathbf{J}} \frac{\sigma^2(f)}{|a(f)|^2} \hat{\mathbf{I}}\hat{\mathbf{J}}^h \right\}^{-1} \quad (1.28)$$

and using the distributive property of matrix multiplication:

$$\hat{\mathbf{R}}^{-1}(f) = \frac{1}{|a(f)|^2} \left\{ \hat{\mathbf{J}} \left\{ \hat{\mathbf{S}} + \frac{\sigma^2(f)}{|a(f)|^2} \hat{\mathbf{I}} \right\} \hat{\mathbf{J}}^h \right\}^{-1}. \quad (1.29)$$

From the property $\{\hat{\mathbf{A}}\hat{\mathbf{B}}\hat{\mathbf{C}}\}^{-1} = \hat{\mathbf{C}}^{-1}\hat{\mathbf{B}}^{-1}\hat{\mathbf{A}}^{-1}$ it follows that:

$$\hat{\mathbf{R}}^{-1}(f) = \frac{1}{|a(f)|^2} \{\hat{\mathbf{J}}^h\}^{-1} \left\{ \hat{\mathbf{S}} + \frac{\sigma^2(f)}{|a(f)|^2} \hat{\mathbf{I}} \right\}^{-1} \{\hat{\mathbf{J}}\}^{-1} \quad (1.30)$$

and because $\{\hat{\mathbf{J}}^h\}^{-1} = \hat{\mathbf{J}}$ and identically $\hat{\mathbf{J}}^{-1} = \hat{\mathbf{J}}^h$ we obtain:

$$\hat{\mathbf{R}}^{-1}(f) = \frac{1}{|a(f)|^2} \hat{\mathbf{J}} \left\{ \hat{\mathbf{S}} + \frac{\sigma^2(f)}{|a(f)|^2} \hat{\mathbf{I}} \right\}^{-1} \hat{\mathbf{J}}^h. \quad (1.31)$$

Consequently, using the decomposition in equations 1.22, the total power output in 1.21 can be expressed as:

$$P(f, \mathbf{k}) = \frac{|a(f)|^2}{L\mathbf{K}^h\hat{\mathbf{J}}^h\hat{\mathbf{J}}\left\{\hat{\mathbf{S}} + \frac{\sigma^2(f)}{|a(f)|^2}\hat{\mathbf{I}}\right\}^{-1}\hat{\mathbf{J}}^h\hat{\mathbf{J}}\mathbf{K}L^h}, \quad (1.32)$$

and using the properties in 1.24:

$$P(f, \mathbf{k}) = \frac{|a(f)|^2}{\mathbf{K}^h \left\{ \mathbf{K}\mathbf{K}^h + \frac{\sigma^2(f)}{|a(f)|^2} \hat{\mathbf{I}} \right\}^{-1} \mathbf{K}}. \quad (1.33)$$

Therefore, given the characteristics of \mathbf{K} obtained from the considerations in 1.25, the previous equation simplifies to a purely scalar form:

$$P(f, \mathbf{k}) = \frac{|a(f)|^2}{\left\{ \frac{n|a(f)|^2}{n|a(f)|^2 + \sigma^2(f)} \right\}} = \left\{ |a(f)|^2 + \frac{\sigma^2(f)}{n} \right\}. \quad (1.34)$$

As in classical beamforming, if the noise variance is assumed to be small and/or the number of receivers is sufficiently large, this technique can closely reconstruct the original power amplitude with only negligible distortion (Fig. 1.2 a). Note, however, that if the noise variance is too small or even zero, the method cannot be applied. In this case, the signal cross-correlation matrix is singular or close to singularity and consequently cannot be inverted. In such situations it is common practice to introduce some artificial noise to the system using a matrix diagonal load [Capon, 1969]. This procedure stabilizes the inversion, but has the disadvantage of depending on the defined optimal load being applied without considerable signal distortion. Asten [1976] has experimentally

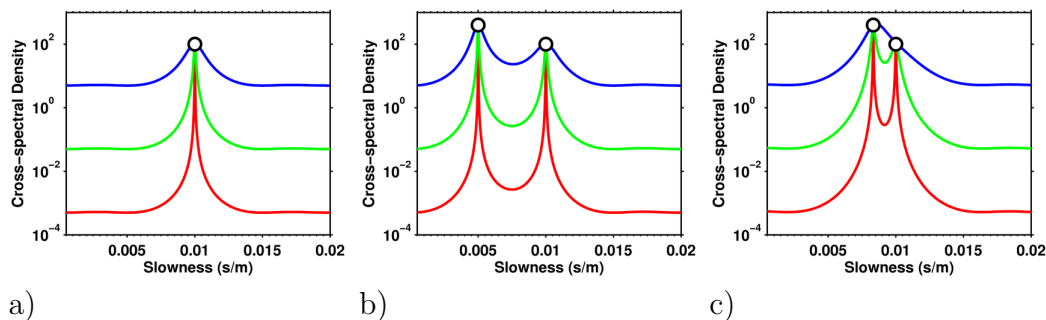


Figure 1.2: Signal identification using high-resolution beamforming: we use the same array configuration as in Fig. 1.1. Compared to classical beamforming, this method allows more accurate identification of single (a) and multiple signals (b), minimizing the effect of the array response. As evident using the three previous noise variances, the total power output level is sensitive to the amount of uncorrelated noise. In case of strong noise variance (blue line), if two signals are too close in slowness (case c) even this method will fail, giving rise to artefact peaks.

investigated the phenomena and proposed a percentual loading value of 1.02 with no significant loss in resolution.

The case of multiple signals is not straightforward to demonstrate mathematically, but has been experimentally investigated. Using synthetic signals, we observe that the performance of high-resolution beamforming is still superior to the classic method whenever the steering vector of the signal of interest is identified (Fig. 1.2 b). However, the amplitude dependence on noise variance, steering vector mismatching and signal interference is no longer linear. In general, incoherent noise most strongly influences the shape of the total power spectrum [Asten and Henstridge, 1984]. Consider the simultaneous presence of two signals coming from the same direction with only slightly different velocities, as for two surface wave higher modes whose dispersion curves are close to apparent intersection. In such situations, if the incoherent noise within the system is large, correctly identifying the signal velocities is impossible (Fig. 1.2 c, blue line), because the adaptive filter is not able to resolve the two contributions separately. Consequently, the corresponding amplitude maxima tend to converge or even merge, giving the impression of a unique signal of average characteristics. The amplitude of this resultant maximum no longer represents one of the original signals. In such a situation, the definition of a general rule that explains at which point the method will fail is not an easy task. Other than on the noise variance of the system, the resolution depends on frequency, on the number of receivers, their configuration and on the relative amplitude of the signals. Note, however, that the true amplitudes are still preserved at

their correct locations. This last point is of fundamental importance because, if the correct velocity is identified in some way (e.g. through a procedure of noise filtering), then the true amplitude, or a good approximation thereof, can be obtained.

1.2.4 Noise filtering and diagonal loading

We use a hybrid singular-value-decomposition approach that combines noise filtering and loading to improve the resolution of the method. Note that for a number of coherent signals smaller than the number of seismic receivers, the smallest singular value of the matrix $\hat{\mathbf{R}}$ approximates the uncorrelated noise variance σ^2 of the system [Kogon, 2003]. Even for a higher number of signals, this approximation is, in most cases, still valid. Based on this assumption, we can hypothetically remove the influence of noise by subtracting this value from each singular value of the signal cross-correlation matrix. In this case, however, the matrix of singular values becomes rank deficient (its last element is equal to 0) and thus $\hat{\mathbf{R}}$ is no longer invertible. We have then two possibilities: the first is to use a Moore-Penrose pseudoinversion that cuts out the null space from the covariance matrix and produce a least squares solution [Sibul, 1984]. The second option consists, by contrast, of loading the singular values of $\hat{\mathbf{R}}$ with a small quantity to make the matrix of singular values artificially full rank. In this second case, unfortunately, identifying the optimum amount of load to apply is not obvious. However, some general rules can be defined: obviously, the final amount of load must be less than the filtered noise variance, by at least one or two orders of magnitude, but must be sufficiently large to be numerically invertible, depending on the characteristics of the software used.

This last approach, theoretically more suitable because it produces sharp maxima in the spectrum, in practice can lead to an undervaluation of amplitudes. This happens with a sampling of the grid search over the slowness-azimuth plane that is too coarse [Asten and Henstridge, 1984]. If the signal peak becomes too sharp and is localized between two consecutive samples, it cannot be correctly identified. In contrast, the first approach, based on pseudoinversion, better preserves the amplitude information but tends toward erroneous localization of maxima. As a direct consequence, we implement a two-step approach: first using a filtering+loading scheme to correctly localize the signal in the slowness-azimuth plane, and then computing the correct amplitude value at the retrieved location with a pseudoinversion approach.

1.2.5 Three component f - k spectrum

Three component f - k analysis [Fäh et al., 2008] extends the original high-resolution algorithm. This is based on the assumption that the superimposed contribution of Love and Rayleigh waves over the horizontal component of motion can be separated with a direction-of-arrival (DOA) decomposition. The horizontal component cross-power spectral matrix is in this case azimuth dependent. Thus, it must be recalculated for each possible direction-of-polarization θ (DOP) as a combination of the North-South and East-West ground motions:

$$\mathbf{u}_H(f, \theta) = \mathbf{u}_{NS}(f) \cos(\theta) + \mathbf{u}_{EW}(f) \sin(\theta), \quad (1.35)$$

$$\hat{\mathbf{R}}_H(f, \theta) = E\{\mathbf{u}_H(f, \theta)\mathbf{u}_H^h(f, \theta)\}. \quad (1.36)$$

The array power output is therefore generated separately for Rayleigh waves (the radial part) as a result of all in-phase contributions with DOA equal to the DOP :

$$P_H^R(f, s, \theta) = \frac{1}{\mathbf{e}_p^h(s, \theta)\hat{\mathbf{R}}_H^{-1}(f, \theta)\mathbf{e}_p(s, \theta)}. \quad (1.37)$$

For Love waves (the transversal part) as a result of all in-phase contributions with DOA orthogonal to DOP :

$$P_H^L(f, s, \theta) = \frac{1}{\mathbf{e}_p^h(s, \theta)\hat{\mathbf{R}}_H^{-1}(f, \theta + \frac{\pi}{2})\mathbf{e}_p(s, \theta)}. \quad (1.38)$$

All previous considerations regarding the amplitude characteristics of the vertical component of motion are thus valid for processing of the two horizontal components.

1.2.6 Rayleigh ellipticity function evaluation

Now we focus on the relation between the amplitude characteristics of spectra calculated for both the horizontal-radial and the vertical components of motion. As previously shown, the Capon algorithm allows us to reconstruct a signal's power content whenever its true location is correctly identified in the s - θ plane. If multiple signals are simultaneously present in the wavefield (e.g. several modes of propagation of surface waves), the method can at least theoretically identify and separate the energy content of each contribution [Marzetta, 1983]. Thus, we can demonstrate that for a signal corresponding

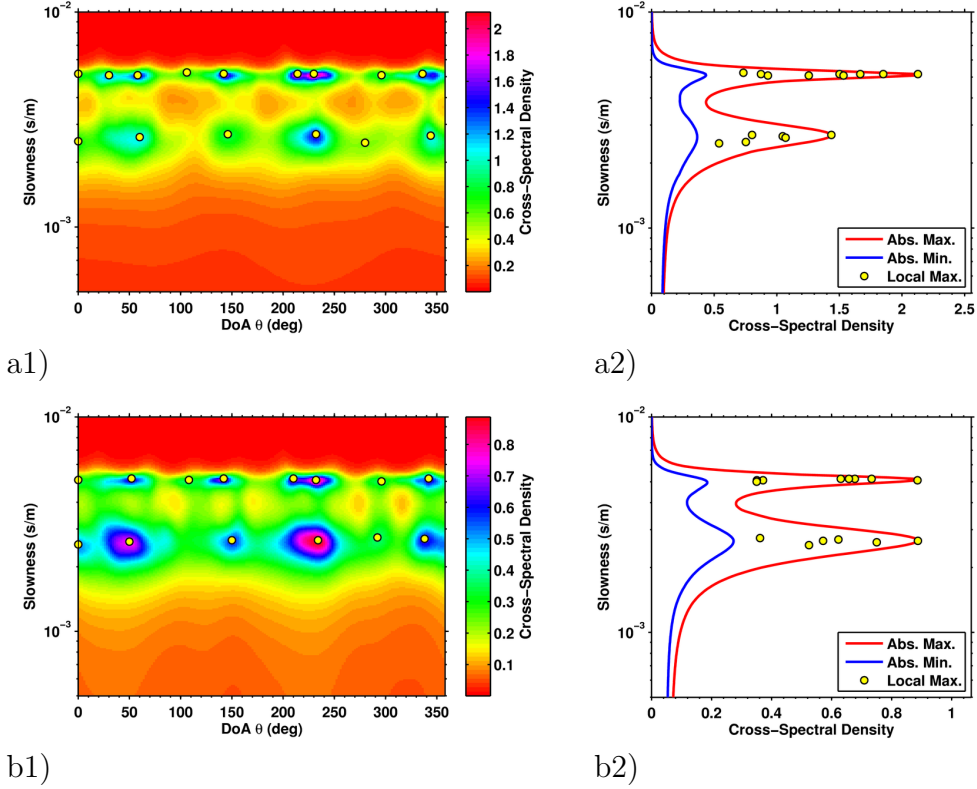


Figure 1.3: Example of three-component f - k processing using synthetic noise data (see SESAME model M2.2 described in paragraph 1.3.1, with array geometry given by the ensemble of all 39 receivers of Fig. 1.7). Identifying multiple signals on the slowness-azimuth plane is performed separately for the vertical (a1, a2) and the horizontal-radial (b1, b2) components and for each frequency (an example given here at 8Hz) using an automatic procedure. It can be observed that the local maxima picked at a specific slowness value (yellow dots) may have different amplitudes within the range of the minimum and maximum cross-power spectrum along azimuth (Abs. Min. and Abs. Max. in a2, b2). Their localization, however, clearly indicate the existence of two separate modes of propagation.

to a specific Rayleigh wave mode, the amplitude ratio between the horizontal-radial (equation 1.37) and the vertical f - k spectra (equation 1.21) will also represent its Rayleigh mode-related ellipticity function. Obviously, the square root of the ratio should be considered, because cross-correlation methods provide an estimation of energy, whereas ellipticity is usually represented in terms of displacement:

$$ell_{H/V}^R \simeq \frac{\sqrt{P_H^R(f, s, \theta)}}{\sqrt{P_V^R(f, s, \theta)}} = \sqrt{\frac{\mathbf{e}_p^h(s, \theta) \hat{\mathbf{R}}_V^{-1}(f) \mathbf{e}_p(s, \theta)}{\mathbf{e}_p^h(s, \theta) \hat{\mathbf{R}}_H^{-1}(f, \theta) \mathbf{e}_p(s, \theta)}}. \quad (1.39)$$

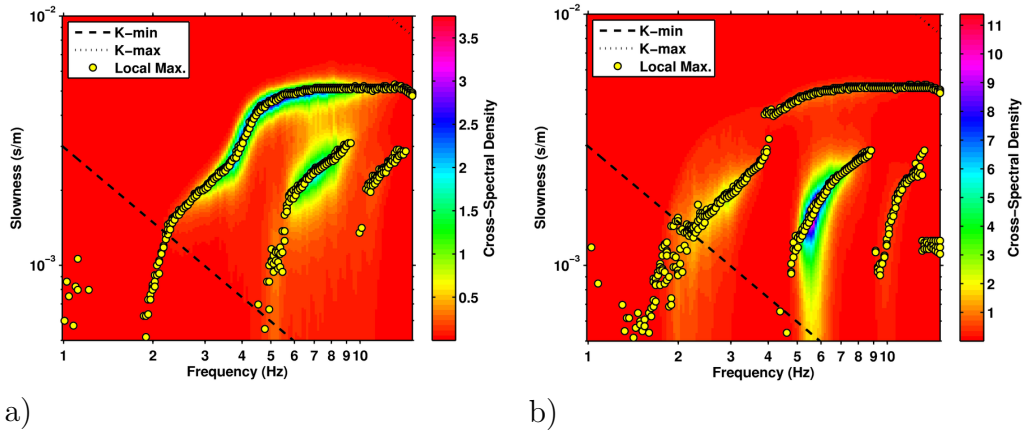


Figure 1.4: Following the example of Fig. 1.3, all the maxima picked on the slowness-azimuth planes at different frequencies are then collected on the corresponding slowness-frequency planes (a, for vertical and b, for horizontal radial component) to extract the modal dispersion curves. The surface of maximum cross-power along azimuth is also presented in background for comparison. It is interesting to notice that even if the modal dispersion curves are comparable between the two components, the distribution of energy is different. Minimum (k_{min}) and maximum (k_{max}) wave-number resolution limits are defined as in paragraph 1.2.7.

Clearly, to avoid numerical scaling errors, the two spectral components must be processed with the same scheme of parametrization (windowing length, tapering type, gain etc.).

However, as we have already stressed, ambient noise can be considered as an ensemble of several signals generated from sources uniformly distributed around the array. In this context, wave packets that belong to the same mode of propagation can exist with very different absolute amplitude, depending on the source distance, type, orientation and intensity. Consequently, to retrieve true ellipticity, we must perform the spectral ratio between picked maxima that belong exclusively to the same signal on the horizontal-radial and vertical components. In this way, any scaling factor induced by source variability is automatically removed by the ratio.

Fig. 1.3 (a1 and b1) shows an example of maxima localization in the slowness-azimuth planes. Two modes of propagation are clearly identifiable and several signals that belong to these modes are picked up from different directions of arrival. Note that identifying these maxima is separate for the horizontal-radial and vertical components of motion. This approach is necessary because the energy carried by Rayleigh waves could drastically vary between the two, or even vanish in certain frequency ranges (Fig. 1.4). Thus,

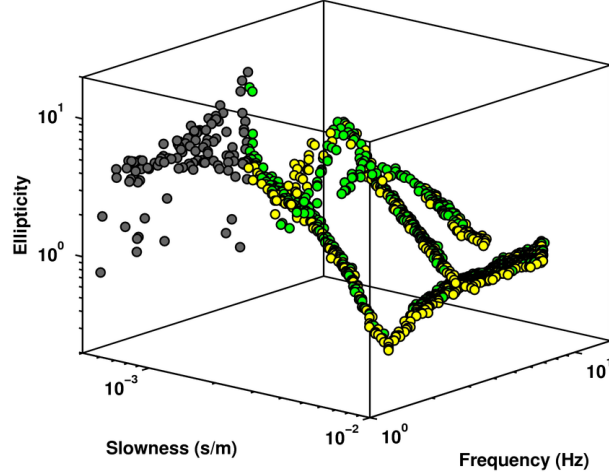


Figure 1.5: Representing the selected ellipticity values in three dimensions helps to identify and isolate clusters of points that belong to the same mode of propagation. This minimizes errors induced by misinterpreting modal jumps and aliasing. The figure presents in green the ellipticity values from signals chosen on the horizontal component only, in yellow those from the vertical and in grey those points beyond resolution limits.

there could be signals that can be identified only in a specific direction of motion. This is common for the frequency range corresponding to the fundamental mode ellipticity first maxima, where the vertical displacement always decreases toward zero. Consequently, once a mode is identified on one component, the corresponding amplitude value in the complementary direction is also extracted. Then the ratio is performed (Fig. 1.5).

Finally, the ensemble of all picked values from both components of motion (Fig. 1.6 a) is analysed statistically by using a normalized probability density distribution. From the histogram representation (Fig. 1.6 b), the expected values of ellipticity are then manually extracted for each frequency.

1.2.7 Resolution capabilities

In classical beamforming techniques and partially in Capon's method, theoretical spectral resolution is controlled by the kind of temporal and spatial sampling that the sensor array performs on the seismic wavefield. Since the temporal sampling is always uniform and generally very dense, simple rules such as the *Nyquist-Shannon* theorem can be applied to define the corresponding frequency resolution limits. In most cases these cover an extremely broad

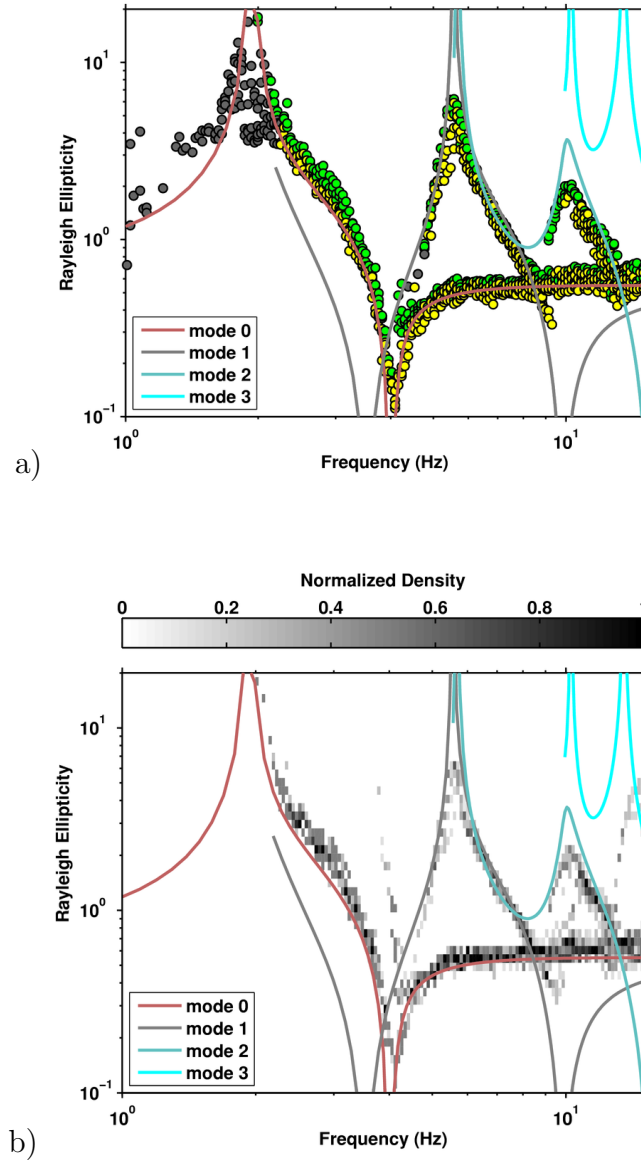


Figure 1.6: The ensemble of all the calculated ellipticity values from the elaboration of both vertical and horizontal-radial components (a: colors as for fig. 1.5) is then statistically analyzed. We used a histogram representation (b) to identify a final average value (manually extracted). To make the statistics comparable over different frequencies, the probability density distributions are normalized to their maximum value. Theoretical ellipticities are also presented for comparison (solid curves).

range:

$$f_{min} = \frac{1}{T}, \quad (1.40)$$

$$f_{max(Nyquist)} = \frac{1}{2dt} \quad (1.41)$$

where dt is the temporal sampling rate and T is the total duration of the record.

By contrast, the receiver spatial configuration is commonly very irregular, since practical obstacles (e.g. buildings inside a city) can force a non-optimal sensor location. Moreover, the number of available seismic detectors is drastically limited by cost. As a direct consequence, special considerations are necessary to reconstruct the correct signal amplitude.

To define the wavenumber resolution limits of beamforming methods, we express the theoretical array response of equation 1.13 in index notation as [Wathelet et al., 2008]:

$$\begin{aligned} B(\mathbf{k}) &= \frac{1}{n^2} \sum_{i=1}^n \sum_{l=1}^n e^{-j(k_x(x_i-x_l)+k_y(y_i-y_l))} \\ &= \left| \frac{1}{n} \sum_{i=1}^n e^{-j(k_x x_i + k_y y_i)} \right|^2. \end{aligned} \quad (1.42)$$

Note that the beampattern function can also be expressed as the squared impulse response of the bidimensional discrete Fourier transform, whose periodicity imposes a wavenumber aliasing limit of:

$$|\mathbf{k}|_{max} = \frac{1}{2D_{min}} \quad (1.43)$$

where D_{min} is the minimum distance between receivers within the array. With some limitations, however, we observed that some results can also be obtained with the high-resolution method in the range:

$$\frac{1}{2D_{min}} \leq |\mathbf{k}| \leq \frac{1}{D_{min}} \quad (1.44)$$

due to partial suppression of aliasing induced by adaptive filtering. Clearly, in this extended range, the number of available receivers most strongly influences the quality of achievable results.

Defining the wavenumber lower resolution bound is a matter of discussion [Tokimatsu, 1997; Park et al., 1999]. We proceed then on the basis of the

following. By substitution of variables, equation 1.42 can also be expressed in the form:

$$B(\mathbf{k}) = \frac{1}{m} \sum_{s=1}^m e^{-j(k_x X_s + k_y Y_s)} \quad (1.45)$$

where $m = n^2$ and $[X_s, Y_s] = [x_j - x_l, y_j - y_l]$ are the coordinates of the new transformed domain (the *lag* domain, see Haubrich 1968 for clarification). Note then that the minimum wavenumber will be controlled by the maximum distance L_{max} between samples in this domain which corresponds to double the maximum existing distance D_{max} between sensors:

$$|\mathbf{k}|_{min} = \frac{1}{L_{max}} = \frac{1}{2D_{max}}. \quad (1.46)$$

Capon's method improves the resolution range at lower wave-numbers. In the pure theoretical case, without any noise influence, the resolution is infinite [Woods and Lintz, 1973]. In practice, rather than the array geometry, the level of incoherent noise is the main factor controlling this lower bound. With microtremors, however, an objective estimation of this influence is not straightforward. Consequently, to avoid bias in evaluating the ellipticity function, we decided to be conservative, using the lower limit imposed by classical *f-k* analysis.

These considerations are theoretically valid for uniform sampling. Nevertheless, given the array's irregular geometry in the two spatial directions, the true resolution becomes azimuth dependent [Zywicki, 1999]. Several high-amplitude side-lobes in the beampattern can interfere with the signal of interest. However, under the assumption that ambient noise sources are equally distributed around the array, the resolution limits we defined can be considered valid as an upper bound of possibilities.

Additionally, consider the energy content of the signal. Even in the best experimental conditions and inside the resolution limits, if the wave energy is too low, identifying the correct propagation mode is difficult and maxima are hardly visible in the slowness-azimuth plane. Therefore, as an additional resolution constraint, we introduce the following empirical rule: compare only those portions of dispersion curves simultaneously identifiable on both the horizontal and vertical *s-f* planes.

1.3 Results

The proposed method has been tested with synthetic and real datasets of ambient noise array recordings. For synthetics, three different models were

	h (m)	V_p (m/s)	V_s (m/s)	ρ (kg/m ³)	Q_p	Q_s
M2.1	25	500	200	1900	50	25
		2000	1000	2500	100	50
M10.2	18	1350	250	1900	50	25
		1350	333	1900	50	25
		2000	1000	2500	100	50
M11.2	4	1350	380	1900	50	25
		1350	360	1900	50	25
		1350	340	1900	50	25
		1350	320	1900	50	25
		1350	300	1900	50	25
		1350	280	1900	50	25
		1350	260	1900	50	25
		1350	240	1900	50	25
		1350	220	1900	50	25
		2000	1000	2500	100	50

Table 1.1: Parameters of the one-dimensional models employed to generate ambient noise synthetics.

employed. To make the results comparable, these models were selected with similar ellipticity patterns but with increasing structural complexity, going from a simple layer over a half space to a multilayered model. In contrast, the real case experiment has been conducted blindly. The experiment location, however, was selected to approximate the best experimental conditions.

For each processed dataset, information about array geometry and resolution, phase velocity dispersion and f - k ellipticity is provided. For synthetics, experimental curves are compared with the corresponding theoretical ones; for real cases, the results from the proposed method are presented together with H/V curves obtained from standard single-station analysis to show the improvement achieved.

For processing synthetic and real datasets, ellipticity and dispersion curves were extracted manually from f - k spectra using the histogram representation presented in Fig. 1.6 b; manual selection allows a more accurate control over the final result than an automatic detection procedure. It usually avoids misinterpretation induced by aliasing or modal jumps.

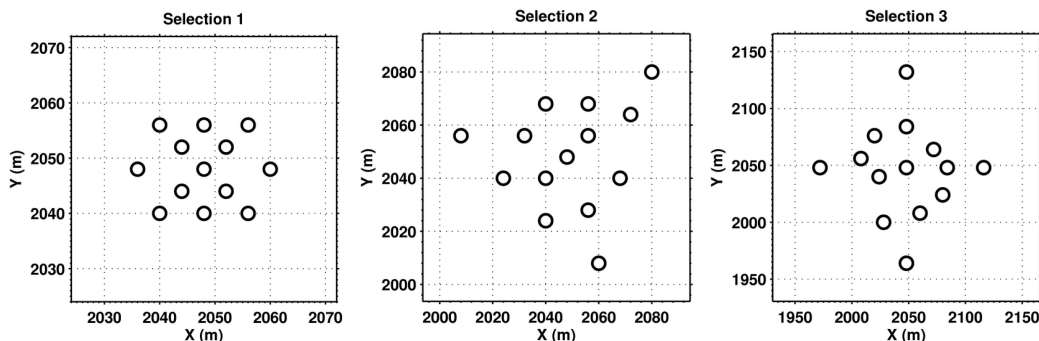


Figure 1.7: Selected receiver configurations we used for the synthetic tests M2.1, M10.2 and M11.2. The three subarrays share the same central station, but the diameter increases progressively from *selection 1* to *3*. An additional configuration was considered, using all the available 39 receivers.

1.3.1 Synthetic datasets

Synthetic datasets employed to test the method were produced within the *SESAME* European Project (“Site Effects Assessment Using Ambient Vibrations”, Deliverable 12.09.2004; Bonnefoy-Claudet et al. 2006a) using a modified version of the finite-difference modelling code proposed by Hisada [1994]. All structural models are one-dimensional (one or more horizontal soft layers of different thickness over a stiff half space, Table 1.1). To realistically simulate the behavior of a sedimentary basin, the layer’s velocity (V_p and V_s), density (ρ) and quality factors (Q_p and Q_s) are set to increase at the bedrock interface. Inside the basin low-velocity zones are also permitted. The noise field is forced to represent a source distribution statistically uniform in space and time (for details see *SESAME* deliverable D12.09-Wp09 “Simulation of seismic noise”). Two different types of source time-functions were employed simultaneously to model the behavior of the expected ambient noise sources: a delta-like impulse and an harmonic wavelet-type function. Point force orientation is allowed to vary (horizontally and vertically) among sources to give rise to both P-SV and SH wave propagation phenomena.

Each synthetic dataset consist of 39 three-components records calculated for different station locations; each trace is approximately 405s long. To test the method under the best experimental conditions, we first used all stations simultaneously to extract dispersion and ellipticity curves. However, employing such a huge number of receivers is not realistic, given the high cost of instrumentation. For this kind of survey, the number of acquisition units usually runs between 8 and 16. Therefore, we decided to additionally test small

configurations of 13 and 14 stations (Fig. 1.7). We selected the relative array geometry from the available station locations and tried to resolve the frequency range between 2 and 15 Hz .

1.3.2 Model M2.1

Model $M2.1$ represents the simplest situation in which a unique horizontal sedimentary layer overlays a high-velocity half-space (the geophysical bedrock). In this case, a unique strong contrast of impedance holds for S and P wave velocities.

For the fundamental mode, using the entire set of available stations, we can obtain a nearly perfect match between the theoretical and experimental ellipticities over the entire frequency range inside the resolution limits of this configuration (Fig. 1.8 a2). A slight overestimation is observed in the middle part of the right flank of the curve; most probably due to the fact that array analysis can minimize the body wave influence, but not entirely remove it. Thus, overestimation can be interpreted as the residual presence of SH waves on the horizontal component.

For the first higher mode, good results are obtained only in the frequency range where the corresponding dispersion curve is clearly identifiable in the slowness-frequency plane. In this case, the energy content of the mode is sufficiently large, especially on the horizontal-radial component, and the peak in the ellipticity curve is consequently well defined. For the second higher mode, however, analysis is not straightforward. Only a small portion of the dispersion curve is clearly visible in a range between 9 and 12 Hz and, from the observation of the theoretical curves, the strong influence of the third mode makes the picked maxima deviate from their true location to lower slowness values. This effect reflects on ellipticity, which shows a good amplitude match only in a limited portion.

If we decrease the number of receivers, the analysis is more complex. Using configuration *selection 1* allows us to obtain the correct value of ellipticity for the fundamental mode only (Fig. 1.8 b2). Nothing can be said for higher modes that are no longer clearly identifiable in terms of dispersion. *Selection 2* gives better results (Fig. 1.8 c2). In this case the resolution limits match the high energy region of the first higher mode, clearly identifiable over a wide range of frequencies. Nothing can be obtained for the second mode, whose dispersion values cannot be picked. Finally, in *selection 3*, aliasing phenomena are unfortunately too close to the high energy region of the dispersion curves. This problem also reflects on ellipticity values for both the fundamental and

first higher modes. Both progressively deviate from the true solution when they approach the Nyquist wavenumber limit (Fig. 1.8 d2).

1.3.3 Model M10.2

The model *M10.2* presents some additional structural complexity. Here, to simulate a moderate gradient of the shear wave velocity, two overlapping sedimentary layers are included. However, the longitudinal wave velocity contrast has been drastically reduced at the bedrock interface, a condition common for water-saturated sand or any analogous high-porosity material.

It is interesting to notice a phenomenon observable at about 5Hz , where the fundamental mode Rayleigh wave gives rise to apparent bifurcation. This is our working hypothesis: the f - k method we use is based on the assumption of plane waves propagation, while in practice close noise sources generate spherical wave fronts. For this reason, on the horizontal component, a small fraction of Love waves will always be decomposed and projected onto the radial component. The array, therefore, will erroneously interpret this residual as a coherent (nevertheless very weak) in-plane wave propagation phenomena. The number of employed receivers and the array geometry influence the final result. It is not surprising that using all 39 available sensor locations, the Love wave contribution is clearly visible and undistorted (Fig. 1.9 a1). Conversely, its influence is too weak to be correctly resolved if we use small configurations (Fig. 1.9 b1, c1, d1). In such cases the result is mainly controlled by the range of resolution (e.g., comparing selections 1 and 3 at 4Hz , respectively outside and inside the resolution limits) and other external factors like the local Rayleigh to Love energy ratio. The effect is less evident in model *M2.1*, even though it has the same receiver configuration and similar type and distribution of noise sources as model *M10.2*. Therefore we assume that an increase in the Love waves energy contribution caused by the different velocity structures might be present.

Our results here are similar to those obtained from the elaboration of model *M2.1* and are to a certain extent better. In particular, in *selection 2*, the second higher mode is now partially identifiable, even if in a narrow range of frequencies (Fig. 1.9 c2). Moreover, in *selection 3*, the first higher mode is closer to the theoretical curve, although the fundamental mode is still slightly overestimated in the right flank of the curve (Fig. 1.9 d2). That overestimation may occur because of the previously mentioned higher energy content of Love waves in this frequency range.

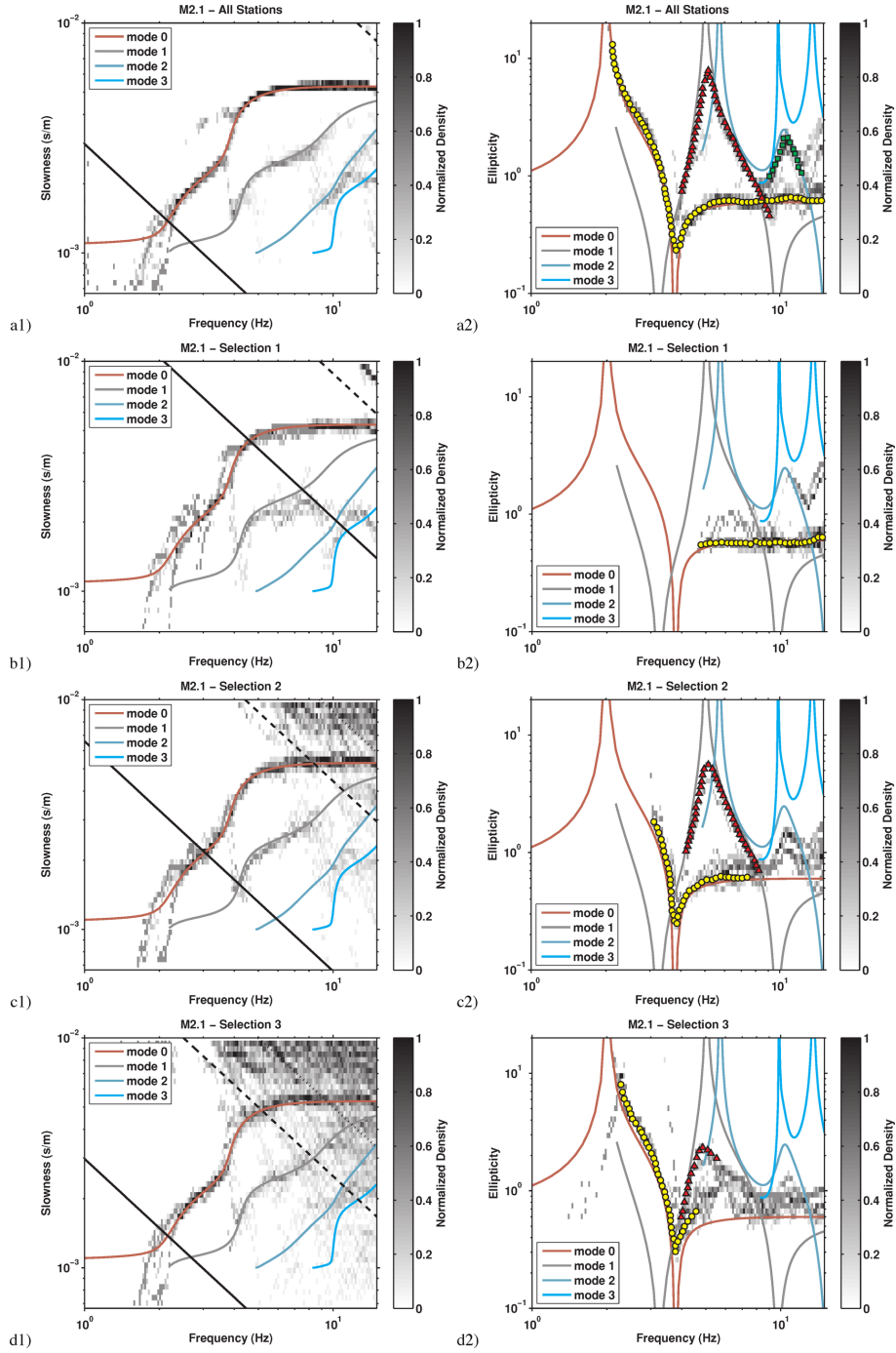


Figure 1.8: Dispersion and ellipticity probability distributions of the model M2.1. Statistics are performed using values picked from both vertical and horizontal-radial components. Resolution limits are included in the dispersion histograms (k_{min} with solid line, $k_{max}/2$ with dashed line and k_{max} with dotted line). For clarity, the ellipticity values out of resolution range are not included. Manually picked ellipticity is thus presented (in yellow the fundamental mode, in red the first higher mode and in green the second higher) with theoretical curves for comparison (solid lines).

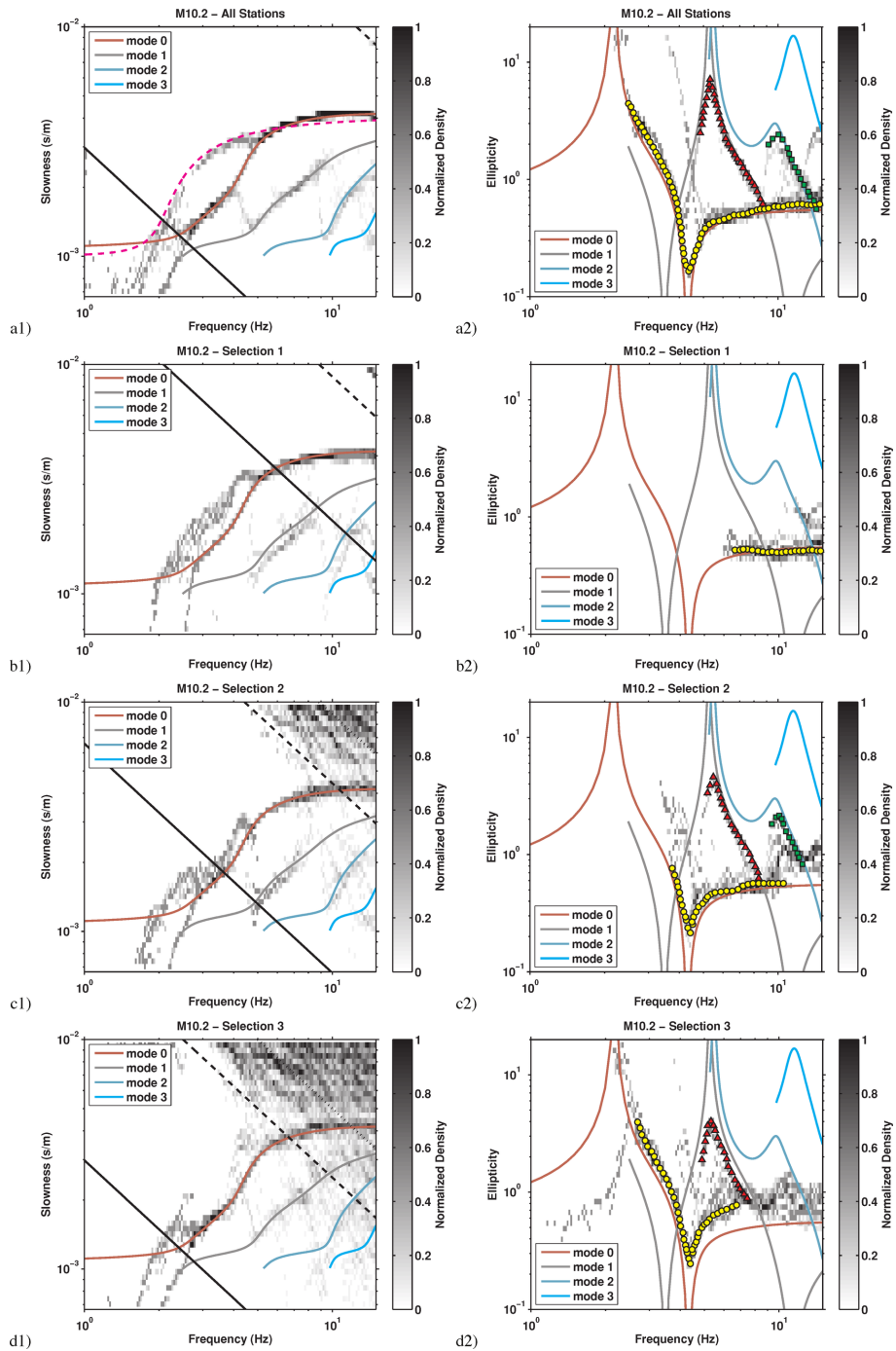


Figure 1.9: Dispersion and ellipticity probability distributions of the model M10.2. Results are comparable to those analyzed in dataset M2.1. Here, however, the influence of Love waves fundamental mode might be stronger (a1, dashed magenta line) and not entirely removable by polarization analysis, as can be inferred from the apparent bifurcation of the observed Rayleigh dispersion curve.

1.3.4 Model M11.2

This last synthetic model is the most complex, consisting of stacked horizontal soft layers with decreasing velocities (a negative gradient) down to the bedrock. Its dispersion pattern shows moderate complexity, with modal curves close to apparent intersection (Fig. 1.10 a1). This sometimes leads to a difficulty in clearly identifying the correct slowness values in the histogram plot. Nevertheless, it is still possible to obtain good results for fundamental and higher modes.

The Rayleigh wave fundamental mode is always clearly identifiable when we use all four types of receiver configurations. The corresponding ellipticity is in most cases close to the theoretical solution (Fig. 1.10 a2). An exception is present in the high frequency region above 12Hz . Here the influence of the first higher mode is strong and reflects on the retrievable ellipticity, which in *selection 1* and *2* is slightly underestimated (Fig. 1.10 b2 and c2). In *selection 2*, additionally, the fundamental mode ellipticity is definitely overestimated between 3 and 4Hz .

Model *M11.2*, however, shows the smallest energy content of higher modes in comparison to the two previous tests. The first and second higher modes are reasonably identifiable if we use all available receivers, but ellipticity is only correctly retrieved for a limited portion of these modes. Furthermore, using the selected configurations 2 and 3, the frequency range where good results are obtainable is drastically reduced, because the dispersion curves of the higher modes are not clearly retrievable from the slowness-frequency plane (Fig. 1.10 c2 and d2). This problem is due to their low energy content. In such situations, we urge a conservative definition of ellipticity to avoid biased results.

1.3.5 Real test case: the town of Visp

To test the method in a real situation, we conducted an experiment at two different locations in the neighborhood of the town of Visp in southern Switzerland. From a geological point of view, this area is a Quaternary sedimentary basin consisting of horizontally layered fluvial deposits [Roten et al., 2006, 2008]. Despite the valley's typical V -shape, it is sufficiently wide to assume one-dimensionality, an assumption required by the f - k method and still valid for the upper layers. The total thickness of the basin progressively varies in relation to the distance from the valley axes. However, for our station locations, the depth of the bedrock can be locally estimated to be 100m for *Array 01* and 160m for *Array 02*. Also the topography at the measurement locations is not particularly irregular and a plane free surface can be assumed. The bedrock,

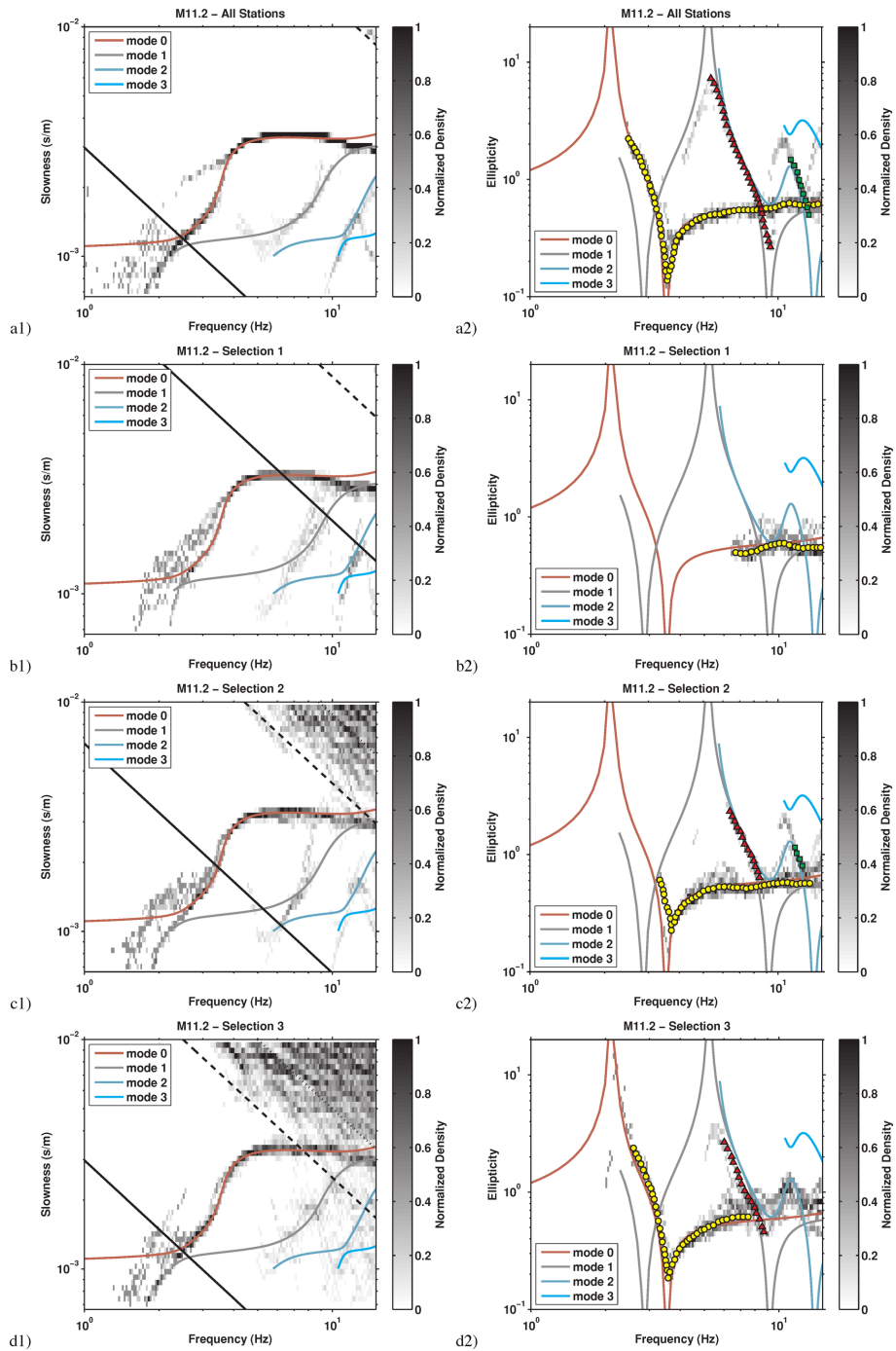


Figure 1.10: Dispersion and ellipticity probability distributions of the model M11.2. This case represents one of the most complex, because the shear-wave velocity has a negative gradient. Identifying the correct dispersion curve is not always possible, especially for higher modes, due to apparent intersection of modes at specific frequencies.

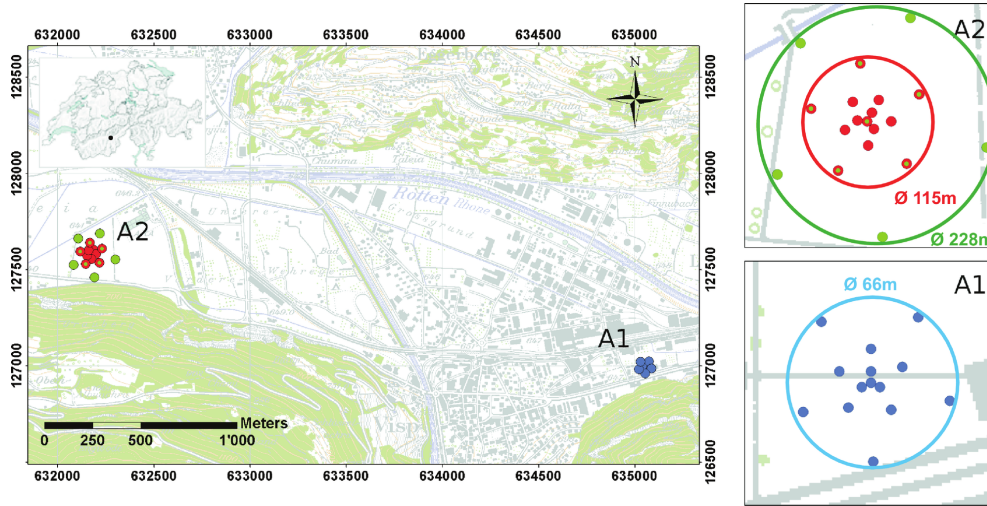


Figure 1.11: Location of the two array measurement sites in the area of Visp (Switzerland). Units are in Swiss coordinates. For the *array 01* test, a single configuration of 14 receivers was used (in blue). For the *array 02* test, two overlapping configurations of 14 (in red) and 11 receivers (in green) were employed separately.

constituted by gneiss in the northern part of the basin and metamorphosed mesozoic limestone in the south, ensures a moderate contrast of impedance at its interface.

For the first test location, a single array of 14 stations has been set up (Fig. 1.11). For the second, two separate array configurations with different radii were employed, of 14 (*configuration 1*) and 11 (*configuration 2*) stations respectively. The acquisition was performed using 5s triaxial velocimeters. For each array, together with dispersion curves and ellipticity results, the receiver geometry, the geographical location in the area of Visp and the results from single-station H/V spectral ratio analysis (Fig. 1.12) are thus presented.

1.3.6 Visp Array 01

After frequency-wavenumber analysis of this dataset, the Rayleigh dispersion curve for the fundamental mode is clearly retrievable in the frequency range between 3 and 12 Hz (Fig. 1.13 a1). Although the histogram shows a moderate scattering of the picked values, the corresponding ellipticity is well identified. Most probably, higher modes are present in the wavefield, as indicated by the presence of high amplitude values in the ellipticity plot. However, the difficulty in following the corresponding dispersion curves in the slowness-frequency

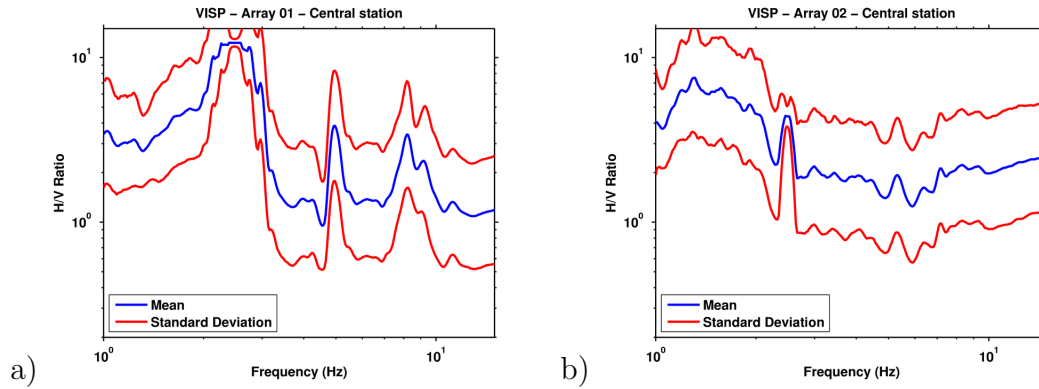


Figure 1.12: Standard single-station H/V spectral ratios from the central sensor of *array 01* and *array 02* in Visp. The two curves are visibly affected by disturbances around 2.5 Hz and 5 Hz , presumably of industrial origin (a pump or a compressor), which are also observed on the entire Rhone plain.

plane makes identifying the ellipticity extremely questionable. Nevertheless, we can separate these contributions from the fundamental mode, a feature not possible using single-station H/V spectral ratios [Fäh et al., 2008].

1.3.7 Visp Array 02

To extend the frequency range of resolution, the *Array 02* experiment was performed with two separate configurations of increasing diameter. From the analysis of *configuration 1*, we obtained good results. The fundamental mode dispersion curve is clearly identifiable, and the corresponding ellipticity is also well defined (Fig. 1.13 b1 and b2). In contrast, identifying higher mode dispersion is more complex but possible if we compute and compare several different elaborations. We must adjust progressively the processing parameters such as the tolerance level for relative maxima identification in the slowness-azimuth plane, and the number of aggregation classes of the histogram distribution. The ellipticities of the first and second higher modes appear reliable, showing a pattern similar to those obtained from synthetic models.

Configuration 2 extended the resolution limits of the previous elaboration to lower frequencies (Fig. 1.13 c1 and c2). The fundamental mode matches reasonably well the results obtained from *configuration 1* for dispersion and ellipticity. For higher modes, the same scheme of elaboration previously introduced has been employed. However, slight differences are observable. In particular, the amplitude of the first higher mode is shifted to lower values, when compared with the corresponding curves obtained from *configuration 1*.

In practice this can be induced, other than by the influence of aliasing, because in real cases approximating a perfect $1D$ structure is not strictly valid. Indeed, an array of such large aperture may sample the wavefield at points where the ground conditions are not perfectly identical. This would influence the higher modes that are generally more sensitive than the fundamental to small-scale variability.

1.4 Discussion and conclusions

The frequency-wavenumber method we propose can retrieve the ellipticity of Rayleigh waves for the fundamental and, with some limitations, higher modes. In comparison to single-station H/V spectral ratios, we can now distinguish and separate the different wave types and, consequently, minimize the influence of Love waves. The amplitude distortion due to SH standing waves is automatically removed within beamforming by destructive interference of the out-of-phase contributions.

Reliable results are obtainable for the fundamental mode of Rayleigh waves, but reasonable results are also achievable for higher modes, whenever the corresponding dispersion curve is well identified in the slowness-frequency plane. We notice some slight difference between the values of ellipticity obtained from separately identifying maxima on the vertical and the horizontal components. Amplitude ratios from signals picked on vertical components are generally more stable over the whole frequency range and closer to theoretical ellipticity. By contrast, results obtained from analysing the horizontal-radial direction tend to be slightly overestimated (approx. $5 \sim 10\%$, depending on the number of receivers), especially at high frequencies. This result is probably due to the residual influence of SH waves on that component. In this second case, however, identifying higher mode dispersion is generally more accurate. We suggest the combined and simultaneous use of the two components to compensate for the contributions and improve the final statistics.

The quality of retrievable ellipticity curves depends on the complexity of the structural model, the array geometry and the noise level. We notice that dispersion curves close to apparent intersection (phase velocity differs less than about $50m/s$) can produce deviations of the amplitude values, due to the difficulty that the adaptive filter has in separating the different contributions. Signals with a low energy content that can hardly be resolved in the slowness-frequency plane can lead to unreliable ellipticity values. As a general rule, signals with a power amplitude lower than about two times the average noise

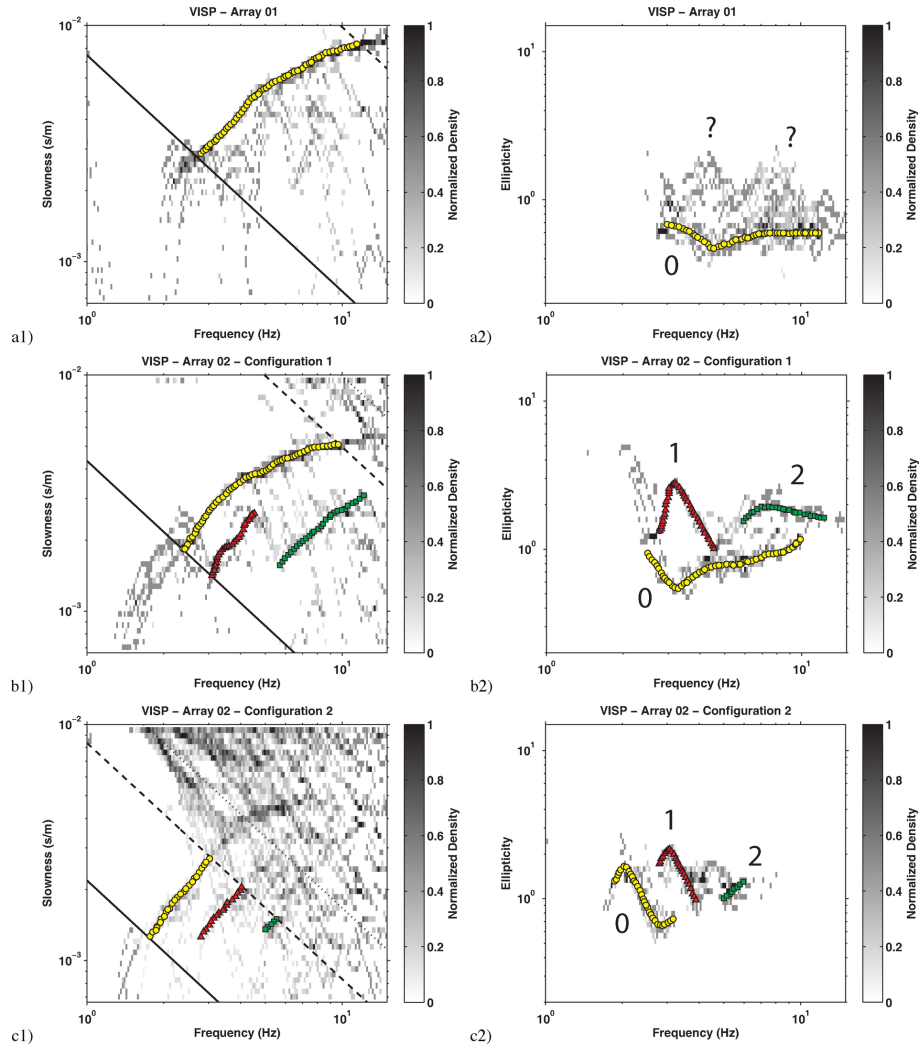


Figure 1.13: Dispersion and ellipticity probability distributions of the two array measurements performed in Visp. As in the previous cases, the curves are manually extracted for dispersion and ellipticity (in yellow the fundamental mode, in red the first higher mode and in green the second). To make results qualitatively comparable, all graphs are presented with the same scale used for synthetics. As expected from the corresponding receiver geometry, curves from *configuration 1* and *2* partially overlap.

power level should be rejected. A progressive reduction in the number of the employed seismic receivers drastically restricts the resolution of the method. This will occur for resolution bounds and amplitude distortion. Sparse spatial sampling can lead to insufficient minimization of the body waves, as well as progressively increased distortion induced by uncorrelated noise. We suggest the use of a number of receivers higher than 15, but in any case not less than 10, to reconstruct the correct ellipticity. Moreover, if the receiver configuration is too irregular, the presence of high-amplitude sidelobes in the beampattern cannot be completely minimized by the adaptive filtering. That effect introduces a progressive scattering in the results. Thus, we suggest optimization of the array geometry.

When different array configurations of increasing size and overlapping resolution bounds are available, we must compare the corresponding segments of ellipticity and dispersion curves to place additional quality control on the final results. Portions of curves that present a good agreement between different configurations can be considered a reasonable measure of true ellipticity. In contrast, we suggest a conservative approach in cases of progressive mismatch: avoid those curves that lack a clear behaviour or those whose corresponding mode of propagation cannot be unequivocally defined. This is particularly important with real complex structures, where the local variability might lead to large deviations in surface wave velocity and energy content (especially for higher modes) within small distances.

The possibility of including the retrieved ellipticity as a constraint for inverting structural models is, at the moment, in the testing phase and no definitive conclusions are yet possible. A more accurate analysis in this direction is planned, and the improvement in using this technique for site characterization will be examined. However, further investigations must be performed on the proposed method to explore its full possibility and application.

Acknowledgments

This research was supported by the Swiss National Science Foundation within the project HAZARD 2010 (No. 200021-112284) and also by the projects NERIES (Network of Research Infrastructures for European Seismology, task JRA4 - *Geotechnical site characterization*) and COGEAR (Coupled seismogenic Geohazards in Alpine Regions). A special thank you to Marc Wathelet for providing the software package *Geopsy* (<http://www.geopsy.org>) that enabled us to test our results. I appreciate all his hints during this last year

of work. I also acknowledge our GJI anonymous reviewers, for their helpful comments and suggestions, and our English editors, Dr. Kathleen Jackson and Dr. Benjamin Edwards. A final thanks goes to Jan Burjanek and Stefano Maranò for reviewing the linear algebra of the paper.

Chapter 2

The use of Rayleigh wave ellipticity for site-specific hazard assessment and microzonation. Application to the city of Lucerne, Switzerland.

Submitted in Geophysical Journal International as:
Poggi, V., Fäh, D., Burjanek, J. and Giardini, D. (2010),
The use of Rayleigh wave ellipticity for site-specific hazard assessment and microzonation. Application to the city of Lucerne, Switzerland.,

Abstract

The sediments underlying the city of Lucerne (Switzerland) consisting of fluvio-lacustrine deposits of Quaternary age have the potential to produce strong amplification of the seismic wavefield. To obtain a reliable estimation of the deep soil structure, we combine different methodologies based on ambient noise recording, such as single station horizontal to vertical ratios and three-component array analysis. Two new techniques to estimate Rayleigh wave ellipticity from ambient noise recordings are tested. These are based on a single- and a multi-station approach, respectively. The first utilizes the continuous wavelet transform to perform a decomposition of the noise wave-field and to isolate and extract the PSV contribution. The second, conversely, relies on a high-resolution f - k method to achieve the same result. We compare the results from the two techniques to provide an evaluation of their capabilities and limitations. Comparing the classic method to compute H/V ratios and the wavelet-based approach, it is possible to estimate the relative energy contribution between the SH and PSV components. From such ratios we provide a confirmation of the imperfect equivalence between f_0 from ellipticity (or better the singularity of the ellipticity curve) and f_0 from the SH transfer-function.

To improve resolution on the bedrock depth a two-step inversion scheme is presented. In particular, the surface wave dispersion information is initially used to constrain the soft sediment part, while the Rayleigh wave ellipticity is subsequently used for constraining the bedrock depth. It is shown that such approach is beneficial to map the bedrock geometry over dense urban areas. The output velocity model is then used to compute the local seismic amplification by means of gridded 1D approximation. Two different approaches are compared, the SH-wave transfer function formalism and the quarter-wavelength approximation.

2.1 Introduction

Seismicity in central Switzerland is moderate [Gisler et al., 2004]. Earthquake activity has been very low for the time period of modern instrumental observation. The largest known earthquakes in the past are the September 18, 1601 (Mw 5.9), the September 10, 1774 (Mw 5.7) and the earthquake swarms of 1777 and 1964. The epicenters of these events indicate a concentration of activity around Altdorf (1774, 1775) and Sarnen (1601, 1777, 1964), whereas recent instrumentally observed earthquakes are distributed more evenly over the whole area. Moreover, earthquake activity was extraordinarily low since

the beginning of modern instrumental observations in the 1970s. The irregular episodes of stronger earthquakes, both in space and time, characterize the seismicity of central Switzerland. Identified evidence for three large paleo-earthquakes in central Switzerland with moment magnitudes (M_w 6.5–7.0) significantly exceed historically known values [Strasser et al., 2006].

The 1601 earthquake is the strongest historical event in central Switzerland of the past millennium and amongst the seven strongest events in Switzerland known from historical sources [Schwarz-Zanetti et al., 2003]. The main shock of September 18 with $M_w=5.9$ produced rockfall at many places in central Switzerland. Of these, however, only those on the mount Hahnen near Engelberg and the mount Bürgenstock are described in historical sources. Rockfall at Bürgenstock into the lake Lucerne and the earthquake triggering of a sub-aquatic landslide caused a tsunami and a seiche. The seiche in Lake Lucerne caused the river Reuss in Lucerne to flow back six times during the first hour after the earthquake, with the result that each time the riverbed was empty for several minutes [Schwarz-Zanetti et al., 2003]. In the whole of Lucerne, chimneys and tiles fell and walls cracked. However, most seriously affected was the so-called little town, in particular the towers of the city wall. This area of the little town is the main focus of our work. Only a small part of the marshland was developed at the time of the historical earthquakes. Urbanization started at the end of the 19th and beginning of the 20th century. Today, buildings and infrastructure cover the whole area (Fig. 2.1). Together with the evidence of a dense population of the area, a seismic characterization of the Lucerne city is of primary importance. Adequate risk mitigation measures have to be undertaken [Basler and Partner, 2007].

To obtain a sufficiently accurate estimation of the seismic local response on a larger area, a considerable number of measurements are necessary. Calculation of the (deterministic) amplification factors is based on an accurate knowledge of the elastic properties of the constituting materials down to a sufficient depth, preferably into the bedrock. These can be assessed directly, by means of boreholes measurements and sampling, and resulting laboratory analysis, or indirectly, through the use of non-invasive geophysical techniques. The first approach is not easily applicable in practice. The high costs of implementation and the difficulty in reaching larger depths (the basement can be located at several hundreds of meters) make direct investigation not always sustainable for engineering site-response analysis. A real problem is the sampling of undisturbed material for laboratory measurements. Conversely, the alternative use of geophysical techniques can lead to reliable results over wide areas and large depths, with a comparatively lower effort. Seismic based

techniques are in general preferable, due to their resolution. Among these is possible to distinguish between active source methods, like refraction or reflection seismics, and techniques based on passive noise recording. The primary difference consists in the type of the employed source and its frequency band. That is artificial and high frequency in the former (e.g. shotgun, explosive), and natural and low frequency (anthropogenic or environmental) in the latter. The spatial resolution is also affected. The two groups, to a certain extent, are complementary. Active methods are suitable for investigations where a high degree of spatial accuracy is required. However, their use is limited in urbanized environments due to the high noise level. On the other hand, passive techniques provide coarser results due to the surface waves that are analysed. But they can be used even in densely populated areas. This is often the case in microzonation studies. Ambient noise methods, moreover, are cheap and easy to implement, which makes them suitable for most engineering purposes.

In this paper, a method is presented for evaluating the local seismic response of wide areas using ambient noise techniques. We focus on the linear elastic properties down and into the bedrock. In particular we propose a technique using Rayleigh wave ellipticity information to obtain a simple but reliable assessment of the bedrock depth. The method basically consists of the separate assessment of the velocity structure of the sediment and the bedrock depth, and also includes an estimate of the bedrock velocity. The method is similar to what has been proposed by Arai and Tokimatsu [2008]. In a first stage, a generic velocity profile (in terms of P and S velocities) is established for the soft-sediment part from the dispersion analysis of ambient noise array measurements. Subsequently, the Rayleigh wave ellipticity from single and multi-station measurements is used to resolve the geophysical bedrock properties in terms of depth and velocity. Two new methodologies to retrieve the Rayleigh wave ellipticity information from ambient vibration are tested. A first approach, proposed by Poggi and Fäh [2010], which is based on a modification of the high-resolution method proposed by Capon [1969] to estimate the Rayleigh particle motion from three-component array recordings of ambient noise. The second approach, developed during the NERIES project (Network of Research Infrastructures for European Seismology, JRA4 “Geotechnical Site Characterization”), tries to achieve the same goal by means of the wavelet time-frequency analysis of single station recordings. Both methods present some advantages and disadvantages. It is the target of this paper to compare capabilities and limitations of such techniques, and to show how their combined use can provide important information for the characterization of the seismic response of a site.

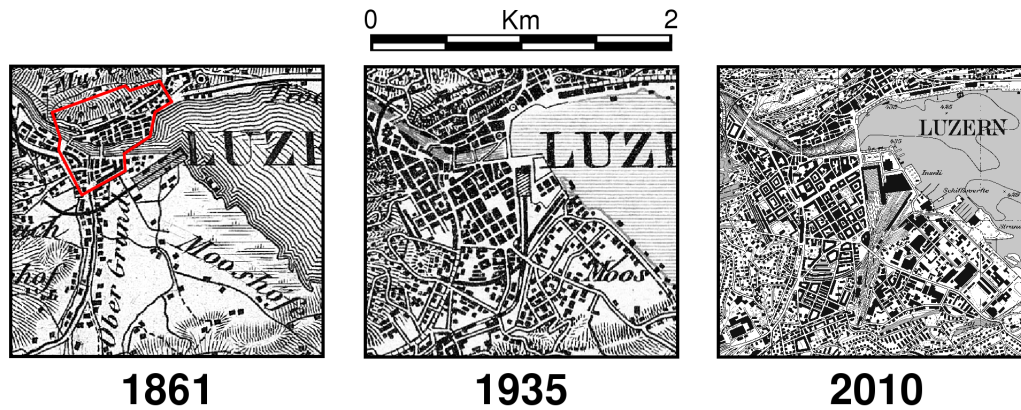


Figure 2.1: Historical evolution of the city of Lucerne from 1861 up today. The red line indicates the possible borders of the old settlement in the 16th century.

The study focuses on the derivation of a generic velocity model of the entire sediment cover in the basin area of Luzern. Due to the strong variability of the near-surface low-velocity part, with a material that is also expected to respond non-linearly, such layer is not yet the target of our investigations. In the last section of the paper, the seismic velocity model obtained from ambient noise analysis has been employed to map the seismic amplification response of the study area. Due to the level of uncertainty in the surface part of the input model, a simplified approach has been preferred. The basin area was divided horizontally in a regular grid of 100x100 cells. For each grid cell a vertical one-dimensional S-wave velocity profile was established and the corresponding amplification function computed. For the calculation, two approaches were used: the SH-wave transfer function for vertical propagation and quarter-wavelength amplification method. While the first method models the SH resonance, the latter provides a generic impedance-based amplification function only. These approaches may be considered as the lower and upper bounds of possibility for the expected 1D amplification.

2.2 Geological setting

The sedimentary basin underlying the city of Lucerne (Switzerland) consists of an alternation of fluvio-lacustrine deposits of Quaternary age. Thick sand layers are alternated with coarse gravels and fine-layered deposits (mostly silt and clay). Alluvial fans had a major influence in the structure of the outer basin, where the material is generally coarser and large-grained. Outside the

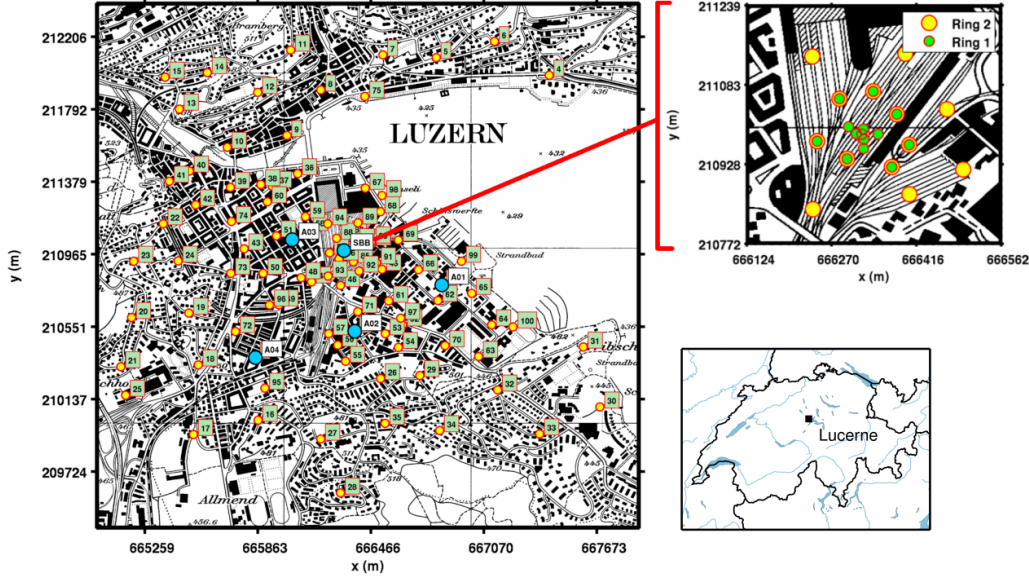


Figure 2.2: Ambient noise measurement location performed in the city of Lucerne (Switzerland). On the left, the map of the 101 single station measurement locations (yellow dots) and five array measurements (blue dots). On the top-right, particular of the large-aperture array deployment within the main train station (SBB array). Units are in Swiss Coordinates (CH1903+).

basin edges, the basement bedrock is largely exposed. It consists of a mixture of clastic sedimentary materials, which originated through sin-orogenic accretion during the Alpine evolution (the subalpine Molasse basin). The bedrock interface geometry, as well as the surface morphology, is the heritage of an alternation of successive inter- and intra-glacial events.

From the geotechnical point of view, the basin area has been defined by previous investigations [Mengis and AG, 2007b] predominantly as category D and C, or F1 of the Swiss Building Code classification (SIA261 - action on structures, 2001). The soil classes are fairly comparable to the classification in EC8 (CEN, 2004), however with some slight difference in the S-wave velocity bounds. From borehole measurements, the first ground water table has been found to be generally shallow, often at less than $5m$ in depth, depending on the proximity to the lake and the topographic elevation.

2.3 Ambient noise measurements

2.3.1 General set-up and single station measurements

In order to reconstruct the seismic velocity structure of the basin of Lucerne, an extensive ambient noise survey was performed, consisting of 101 single station measurements and a large-aperture array deployment within the central area of the basin (Fig. 2.2). Some smaller arrays were set-up at different sites, however not all were successful due to the dense urbanization in certain parts of the city and the proximity to the basin borders. For single station measurements, noise was recorded for a duration varying between 20 and 40 min., depending on the level of urban disturbances. The measurement survey was set-up in two separate stages. In a first round about 60 sites were investigated within the innermost area of the basin, with the goal of characterizing the larger part of Quaternary sediments underlying the city. In a second stage, the remaining measurements were set up in order to refine the contact between soft sediments and outcropping bedrock at the basin edge.

2.3.2 The array survey

To investigate the velocity structure of the sediments beneath the urban area, five array installations of different sizes were deployed. The largest array deployment was set up in the innermost part of the basin (Fig. 2.2), using the widest open space in the city, in order to achieve the highest possible resolving power at depth. A general rule connecting array aperture with depth of resolution is not straightforward to obtain before a measurement. Several empirical relations have been proposed in the literature [Tokimatsu, 1997; Okada, 2003]. Most of these, however, are reliable only as a first approximation. The largest depth reachable during a survey is influenced, apart from the array diameter, by the elastic characteristics of the material and the signal-to-noise ratio in the frequency range of interest [e.g. Jongmans et al., 2005].

In the case of Lucerne, it was possible to use the available space within the track area of the Swiss Federal Railways (SBB) main station (the SBB array). Measurements were conducted overnight and train traffic was stopped during the recordings. The installation consisted of two concentric rings of increasing diameter and 14 receivers each. The first ring (smaller and internal) had a diameter of about 200m, while the second had a diameter of about 350m. Exact station positioning had to be carefully considered. Since the array methods rely on phase-delay estimation, high positioning accuracy is

necessary in order to correctly process the data. Generally, the location error should not be higher than 1-2% of the total array radius [e.g. Jongmans et al., 2005]. To achieve this accuracy in station location, a telemetric survey was performed using a laser theodolite.

An additional four arrays were installed in the surrounding areas of the SBB array, with the aim of mapping any lateral variation of seismic velocity in the uppermost layers. However, due to the location of these installations, the results were biased due to the high level of disturbances in the urban environment. In particular, array 03 failed completely while array 01 only provided sufficiently consistent results over a limited frequency band. Consequently, for the characterization of a generic soil profile, we rely mostly on the results from the SBB array.

2.3.3 Error estimation in orienting the horizontal components

For the elaboration of three-component recordings, special attention has to be paid to the correct alignment of the sensor. An external reference is required for the horizontal components, common to all stations. Usually the magnetic North is used, detected by compass. In the case of the SBB array, however, the possibility of detecting the magnetic North direction with sufficient accuracy was limited by the presence of ferromagnetic material (e.g. rail lines, wagons) and electric-power lines within the station. To avoid biased results, we implemented a quality control procedure on the recordings. Based on the assumption that the very-low frequency content of the recorded motion is nearly in-phase over the whole area of interest, we proceeded as follows. Recordings of the two horizontal components are band-pass filtered for each station location. Different frequency bands can be used depending on the instruments. Since we deal with 5s sensors, a band between 0.5 to 1 Hz was applied in this specific case. This frequency band is below the fundamental frequency of resonance of the sedimentary cover in this area. If broadband sensors are available, however, lower frequencies should be used. Anyhow, the analysed frequencies should not go below the eigen-frequency of the instrument, as in this range phase distortion might affect the result.

The recordings are subsequently divided in 50% overlapping windows of equal length (around 10s). For each window and at a specific station location, the horizontal components are progressively rotated over different azimuths. The result is then compared to a calibration record from the reference station, using the L2 norm. In this case the central station of the array was used as

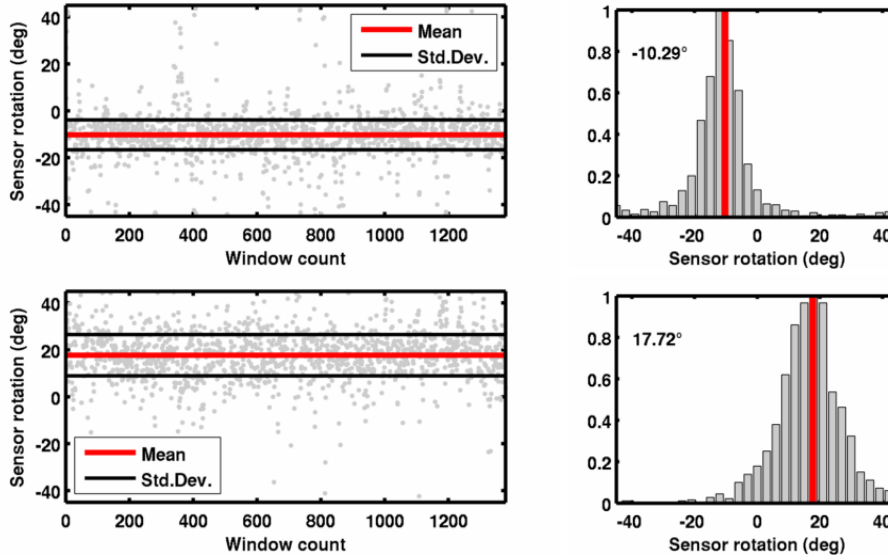


Figure 2.3: Example of the orientation error on the horizontal components of a sensor using a compass for two stations. The analysis is relative to a base station (central station of array SBB) aligned to North. The total error between stations can be quite high e.g. about 27 degree in this example.

the reference. Finally, the azimuths corresponding to maximum of correlation are collected for all windows, and statistical analysis is performed by means of a histogram representation. For the SBB array, large discrepancies were found in the sensor alignment, with deviation up to 27 degrees in total (e.g. Fig. 2.3). An error of such magnitude, if not corrected, would produce considerable deviations in the results from the f - k analysis of the horizontal components.

2.4 Single station processing

2.4.1 Classical H/V ratio

The horizontal-to-vertical spectral ratio (Nogoshi and Igarashi 1971, and see Bonnefoy-Claudet et al. 2006a for an exhaustive reference list) is a technique nowadays widely used in seismic site characterization. It has been applied to earthquake signals, however the most common application is with ambient noise recordings. The major advantage of the method is the possibility of easily obtaining the fundamental frequency of resonance of SH waves (f_0) for a site (e.g., Haghshenas et al. 2008 and references therein). Such estimation is

particularly accurate in all those situations where a large contrast of seismic impedance is present at depth (e.g. sediment-bedrock interface). Following the explanation of Nakamura [1989] the shape of H/V spectra can be controlled by the effect of SH-waves resonating along the structure. It has been demonstrated, however, that even if the f_0 value is correctly retrieved from the H/V curve, the shape and the amplitude of the spectral ratio is generally not representative of the site SH-wave transfer function [e.g. Haghshenas et al., 2008].

The contribution of surface waves in the ambient vibration wave-field is dominant with respect to any body wave contributions in the presence of shallow sources and a strong velocity contrast between sediments and bedrock [e.g. Horike, 1985]. This has been demonstrated for the one-dimensional case [Bonney-Claudet et al., 2006b]. Among surface waves, Rayleigh waves seem to have a major role in controlling the shape of H/V spectral ratios. Nevertheless, in some cases the Love wave contribution might still be significant [Bonney-Claudet et al., 2008]. Taking this into account, the maximum in the H/V spectra have to be carefully considered as a proxy for the estimation of the SH-wave frequency of resonance, since deviations can be experienced due to the contribution of different types of body waves and surface waves. Defining the relative proportion of SH- to PSV-phenomena contribution still represents a major issue to be clarified [e.g. Bonney-Claudet et al., 2006a; Endrun, 2010]. Different techniques have been proposed to face the problem of separating the different wave contributions. However, the answer depends on the velocity structure and the noise sources, and the problem is therefore non-trivial.

2.4.2 H/V ratios using the continuous wavelet transform

H/V ratios obtained from classical analysis suffer from the effects of SH and Love waves on the horizontal components. For this reason, even in case of predominance of Rayleigh waves in the wave-field, the ratio cannot be directly used as Rayleigh ellipticity, if some offset correction that account for SH-wave influence is not applied. A common correction consists in assuming equal contribution of Love and Rayleigh waves on the horizontal plane [e.g. Fäh et al., 2001]. In such case, if the NS and EW horizontal components are combined using vector sum, the correction factor is simply a normalization for square root of two (that is equivalent to applying the quadratic mean on the components). This approximation might be acceptable in most cases, but in

some situations where SH influence becomes stronger in some frequency band, it can lead to overestimations of the ellipticity amplitudes [Fäh et al., 2008].

H/V spectral ratios obtained by means of time-frequency analysis have the advantage of minimizing the effect of SH waves [Fäh et al., 2001]. A method that was developed during the NERIES project basically implements a continuous wavelet transform to produce an accurate time-frequency representation of the noise signal (Fäh et al. 2009b, NERIES JRA4, B2-D4 report). The Morlet wavelet is used [Goupillaud et al., 1984], due to its well-defined central frequency and the possibility to extract phase information. The three components of motion are evaluated separately. The technique is based on the evidence that the vertical component is free from SH propagation phenomena in laterally homogeneous structures. Therefore, once a P-SV transient signal is identified on this component (through a maximum in the time-frequency amplitude spectra), the time-corresponding amplitude is extracted from the horizontal components and the H/V ratio performed. The horizontal components are combined using vector summation. Averaging over long time series statistically increases the robustness of the result. This procedure provides a better representation of the P-SV wave-field polarization, assuming a major contribution of Rayleigh waves (e.g. in Fig. 2.4). The method does not guarantee the possibility of separating out the contributions of higher modes that, when present and sufficiently energetic, might affect the shape of the output H/V ratio. In most cases, however, the energy of the fundamental mode strongly dominates.

Due to the minimization of the SH contribution on the horizontal component, curves obtained with the wavelet technique are shifted to lower amplitude values with respect to classical H/V ratios. This shift, as introduced, might show a frequency dependency, since the SH contribution may not be constant. Comparing the amplitude of H/V spectral ratios from wavelet analysis and those from the classical approach gives the possibility to roughly estimate the relative proportion of SH waves over frequency. If the PSV and SH sources are uniformly distributed around the measurement point, the H/V ratios from the two methods can be represented as follows:

$$\left(\frac{H}{V}\right)_{Classic} = \frac{\sqrt{H_{PSV}^2 + H_{SH}^2}}{V_{PSV}}; \quad \left(\frac{H}{V}\right)_{Wavelet} = \frac{H_{PSV}}{V_{PSV}}. \quad (2.1)$$

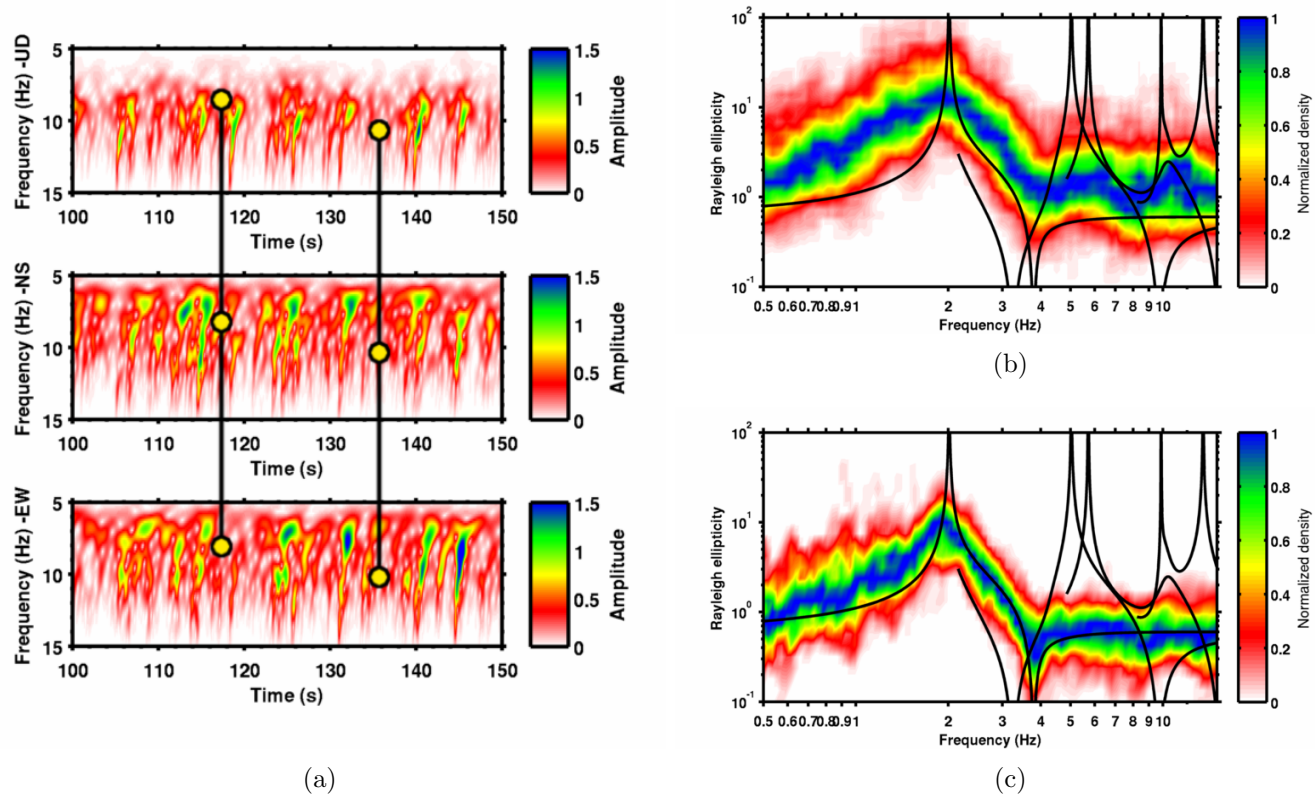


Figure 2.4: In (a) an example of noise-wavefield decomposition using the continuous wavelet transform is given. With respect to the classic method (b), the wavelet based H/V spectral ratio analysis (c) provides a better resolution on the Rayleigh wave ellipticity function in a broad range of frequencies. The SESAME synthetic data-set M2.1 is used for this comparison. The theoretical Rayleigh wave ellipticity function is presented in background for the first four modes (in black).

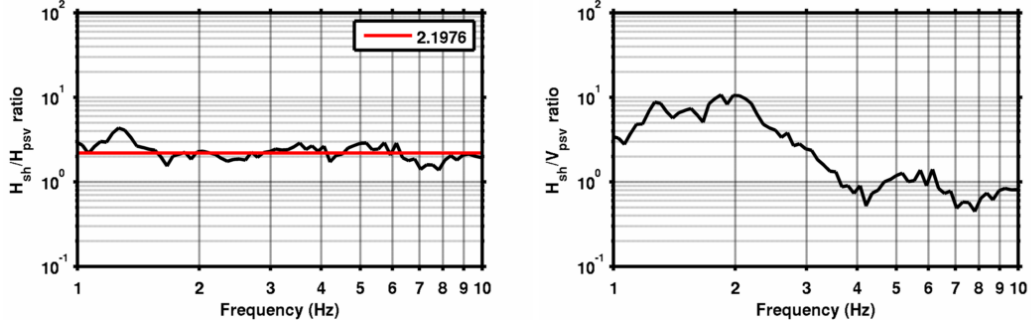


Figure 2.5: SH contribution ratio relative to PSV-horizontal (on the left) and to PSV-vertical (on the right) for the SESAME synthetics of model M2.1. Of the former, the average value is also provided in red colour and can be used as proxy to estimate the average Love to Rayleigh contribution from the horizontal components. The total Love to Rayleigh contribution is discussed further on in Fig. 2.8.

Consequently, the SH contribution relative to PSV (horizontal and vertical) can be written as:

$$\frac{H_{SH}}{H_{PSV}} = \sqrt{\frac{\left(\frac{H}{V}\right)_{Classic}^2}{\left(\frac{H}{V}\right)_{Wavelet}^2} - 1} \quad (2.2)$$

$$\frac{H_{SH}}{V_{PSV}} = \sqrt{\left(\frac{H}{V}\right)_{Classic}^2 - \left(\frac{H}{V}\right)_{Wavelet}^2}. \quad (2.3)$$

The total Love to Rayleigh contribution can then expressed as follows:

$$\frac{H_{SH}}{\sqrt{H_{PSV}^2 + V_{PSV}^2}} = \frac{1}{\sqrt{\left(\frac{H_{SH}}{H_{PSV}}\right)^{-2} + \left(\frac{H_{SH}}{V_{PSV}}\right)^{-2}}}. \quad (2.4)$$

Additionally, if we assume pure surface-wave propagation in the noise wavefield, these equations can be used to approximate the relative energy contribution between Rayleigh and Love waves (e.g. Fig. 2.5).

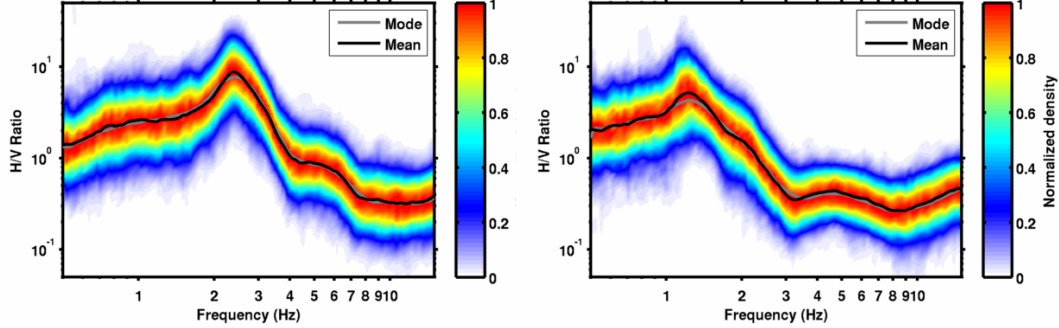


Figure 2.6: Example of wavelet based H/V spectral ratio of single station measurements in Lucerne (station ID 4, on the left, and ID 32 on the right). A Morlet coefficient of 10 is used. Statistic is computed over about 30min. recordings, with 10maxima/min. averaging.

2.4.3 Assessing the SH-wave contribution of the Lucerne area

For Lucerne, H/V spectral ratios were computed using both the techniques for all single station measurements. The influence of the SH contribution has then been tested through comparison between the classic and wavelet-based method. However, only the results from the wavelet approach have been used for further processing (e.g. Fig. 2.6), since we want to work with Rayleigh wave ellipticity in the subsequent sections. Every measurement location is characterized by a different fundamental frequency (Fig. 2.7a). Consequently, the frequency range of computation must be normalized to the specific ellipticity f_0 value (f_0 -Ell) at the site, to make the different elaborations comparable. The average for the whole set of curves has then been produced (Fig. 2.7b). An interesting result comes from the analysis of the ratio curve (Fig. 2.8, green curve). In this case it is possible to observe a considerable decrease in the relative SH-wave energy content at frequencies below the fundamental frequency (f_0 -SH) determined from the H_{SH}/V_{PSV} , with a minimum peak around the ellipticity f_0 . This might be due to the polarization of Rayleigh waves on the horizontal component and not to a change in the total SH energy, indicating the singularity of the ellipticity curve of the fundamental mode. This is also seen when looking at the SH to total P-SV ratio (magenta curve). By analysing the curve (in blue), it is then possible to notice that the frequency peak of the SH-wave (f_0 -SH) is shifted with respect to the one from P-SV (f_0 -Ell) toward higher values. Summarizing, we divided the normalized frequency range into three main regions. In frequency range A of Fig. 2.8, below the fundamental

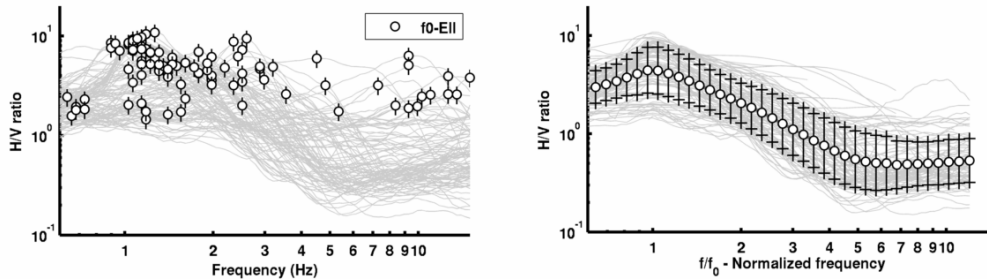


Figure 2.7: In (a), the ensemble of all H/V curves measured in Lucerne using the continuous wavelet transform is shown. The fundamental frequencies (f_0 -Ell) vary in a broad range between about 0.6 and 15 Hz. In (b), the average of all the H/V curves after normalization of the frequency axes to f_0 -Ell is shown.

frequency f_0 -Ell, the contribution of SH- and PSV-waves on the horizontal component is comparable. Here, most probably, the energy of surface waves decreases progressively, and the wavefield is controlled by body-wave propagation [Scherbaum et al., 2003; Albarello and Lunedei, 2009]. In frequency range B, above f_0 -Ell, the SH contribution increases progressively until it becomes dominant around f_0 -SH. Finally, in frequency range C the contribution of SH and total PSV (including vertical and horizontal) is comparable. From the H_{PSV}/V_{PSV} ratio we expect Rayleigh waves to be dominant on the vertical component.

2.4.4 Ellipticity f_0 map

It is a common procedure to use the H/V spectral ratios to map the variability of the SH-wave fundamental frequency of resonance over large areas. This parameter is clearly connected with velocity structure of the basin, and it is consequently used to obtain information about the bedrock depth through simplified approaches [e.g. Hinzen et al., 2004]. In the present work we work on a different assumption, using that the wavelet-based H/V spectral ratios provides an estimation of the Rayleigh-wave ellipticity function. Extracting the first maximum from these curves gives then the possibility of mapping the Rayleigh-wave ellipticity maximum (or singularity) for the fundamental mode (f_0 -Ell) over the area of interest. In case of large velocity contrasts between bedrock and sediments f_0 -Ell is close to f_0 -SH [e.g. Konno and Omachi, 1998; Malischewsky and Scherbaum, 2004] but not necessarily coinciding, as it was observed in Fig. 2.8. For each processed single station measurement, a picking procedure was conducted manually, since a certain level of interpretation was

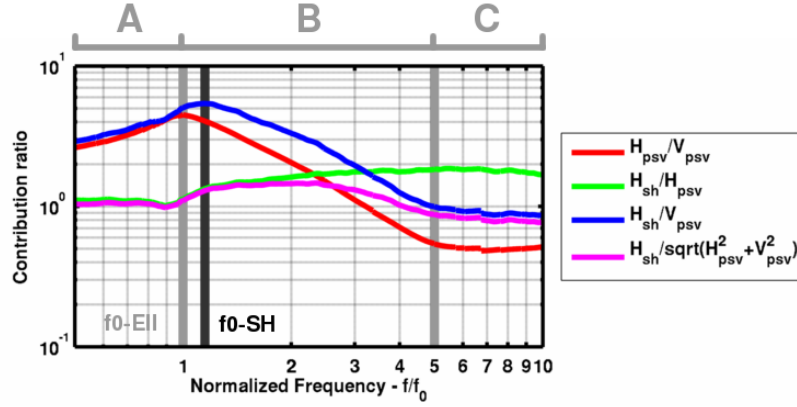


Figure 2.8: SH to PSV contribution ratios from the average of all the single station measurements performed in Lucerne. To make the result comparable between different locations, a normalized frequency axes to the PSV-fundamental frequency (f_0 -Ell) is used.

required. A quality control procedure was then applied on the H/V spectra, considering the width of the H/V peak, the standard deviation of the curve at this frequency range and the level of noise. Some points were discarded when no clear or unique peak was identifiable. Some cases needed some additional interpretation, especially for those sites close to the basin edges, where the f_0 value is generally at quite high frequency. From the ensemble of these values, a map of Rayleigh-wave ellipticity fundamental maximum was then created (Fig. 2.9). To cover the area where no measurements were available, cubic interpolation in the log domain has been employed. Additionally, to produce a smoothed representation of the f_0 variability and to minimize the effect of measurement and processing errors, a low pass filter has been applied to the interpolation result.

2.5 Array processing

2.5.1 Three-component frequency-wavenumber analysis

Frequency-wavenumber analysis is a spectral technique based on multi-station array recording widely used with earthquake and ambient vibration processing to estimate azimuth and phase velocity of horizontally propagating waves (e.g., reviews by Tokimatsu 1997; Okada 2003). For this reason, it is especially suitable for surface wave analysis, such that the phase-velocity dispersion information can be retrieved. The f - k method (also called beamforming,

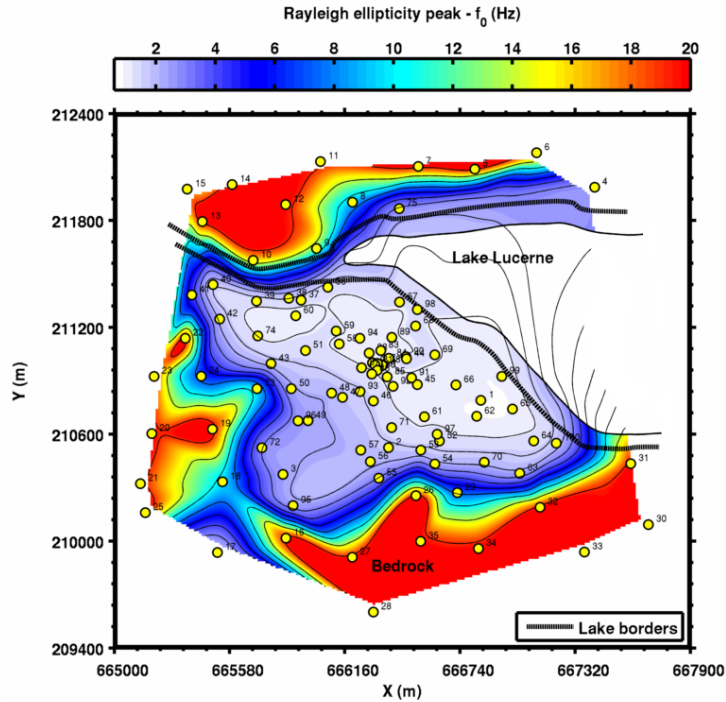


Figure 2.9: Ellipticity- f_0 (f_0 -Ell) map of Lucerne from wavelet based H/V ratios. Cubic interpolation (in log domain) has been used to map the f_0 over points not directly covered by measurement. The result under the lake, due to the lack of sampling points, must be considered only as interpretational. Units of the map are in Swiss Coordinates (CH1903+).

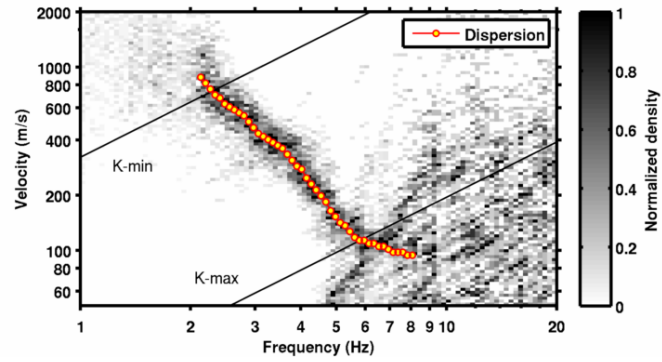
Lacoss et al. 1969) basically implements a sum-and-delay procedure on signals recorded at each station location to induce interference at defined velocities of propagation (VOP) and directions of arrival (DOA). Generally a direct grid search over different VOPs and DOAs is performed, until interference maximum is reached. At this stage the best estimate of the signal properties is detected.

In spite of its simplicity, the major issue of the method is related to its limited resolution capabilities. These are mostly related to the array size, geometry and number of receivers. To partially overcome this limitation, different high-resolution techniques have been proposed with the aim of increasing the resolving power of the array. This is achieved, however, at the expense of an increased computational complexity. A widely used high-resolution technique was proposed by Capon [1969]. This is based on the use of data adaptive filters to minimize the smearing effect of the array response function, and

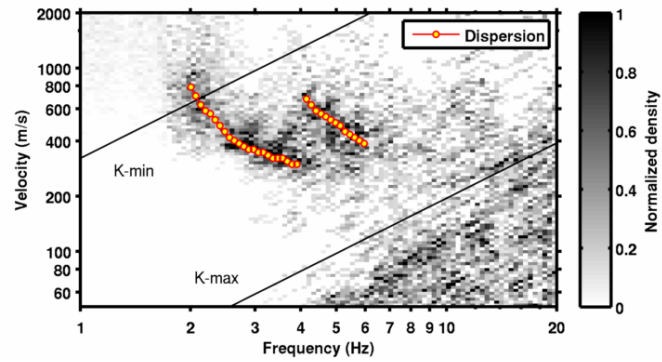
consequently increase the resolution. The main disadvantage is the strong sensitivity of the method to the level of uncorrelated noise. Fäh et al. [2008] extended this technique to the three-component of motions, in order to identify and separate the concurring contributions of Love and Rayleigh-waves on the horizontal direction.

Three-component high-resolution f - k analysis has been used to process the data from the SBB array survey in Lucerne. Array resolution limits were defined as in Poggi and Fäh [2010]. Processing was performed separately for the two concentric ring configurations. In both cases, the ambient vibration records were divided in equal time windows of about one minute each. For each window, a complete f - k elaboration has been performed. The result from all time windows is then represented by means of a normalized histogram (e.g. Fig. 2.10) to account for the statistical uncertainties. Picking of the dispersion curves is performed automatically in the frequency-velocity domain. Next, the mode identification and separation is manually refined, since a certain level of interpretation is necessary at this stage (Fig. 2.11). From the analysis of SBB ring 1, both Rayleigh- and Love-wave dispersion curves were retrieved. Regarding the former, the vertical component is well defined in a frequency range between 2 and 8 Hz, while the radial direction gives less resolution, but allows the identification of higher modes. Mode addressing is clear for the Rayleigh fundamental and the first higher modes. These are close to mode intersection at about 4 Hz. An additional mode is present, but it has not been used during the inversion, because of the unknown mode number. The interpretation of the two Rayleigh modes is generally confirmed by the results from ring 2. The fundamental mode Love-waves dispersion can be retrieved from ring 1 in a frequency range between 2.2 and 4.5 Hz. Ring 2 extends the resolution down to about 1.5 Hz. Some small deviations are clearly noticeable when comparing the results from the two array configurations. This is however expected, since the identical ground conditions are not sampled and some local variability of structure has to be assumed.

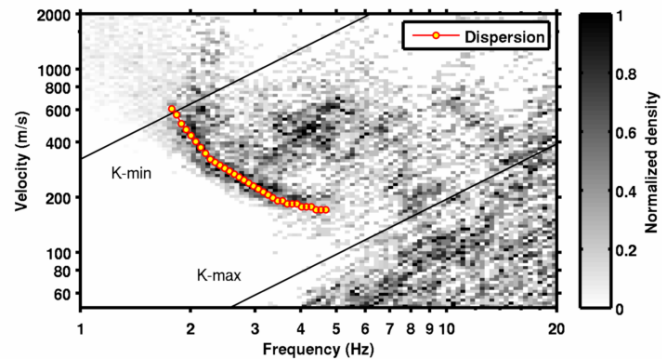
Fig. 2.12 compares the dispersion curves of the arrays 01, 02 and 04 in Lucerne with the dispersion curves of the large array in the train station area for the fundamental mode of Rayleigh waves. Array 03 did not produce any useful results, due to the high level of disturbances of the town. The differences in velocity of array 02 with respect to the SBB and 01 array reflect the different bedrock location under these measurement points (close to basin edges). Most probably, array 04 identifies a higher mode only. Due to the difficulty in mode addressing, then, results from this array were also rejected.



(a)



(b)



(c)

Figure 2.10: Wave-field decomposition using high-resolution f - k analysis. The contribution of Rayleigh and Love waves can be separated and extracted from the three components of motion. Here an example from the elaboration of the ring 1 of the SBB array. In (a) the vertical, (b) radial and (c) transversal components. Resolution limits (K-min, K-max) are also indicated.

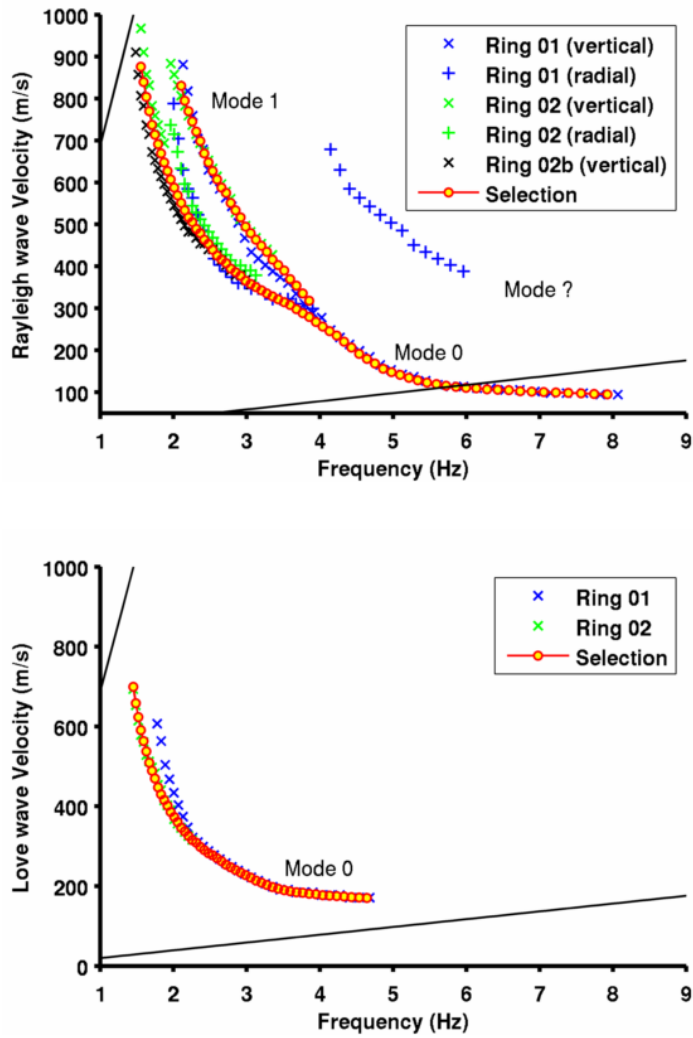


Figure 2.11: Summary of dispersion information obtained from f - k analysis of the array SBB (ring 1 + ring 2). For Rayleigh waves (on top), three modes were found. The third mode, however, mode labelling was not possible. For Love wave (on bottom) the fundamental mode only was clearly identifiable. Resolution limits are indicated as black solid lines.

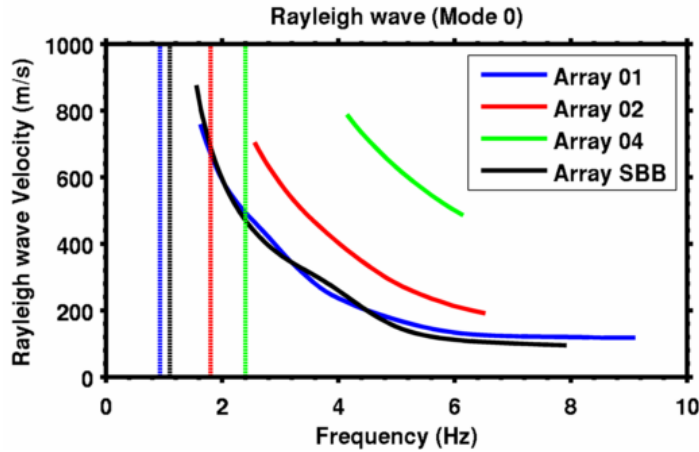
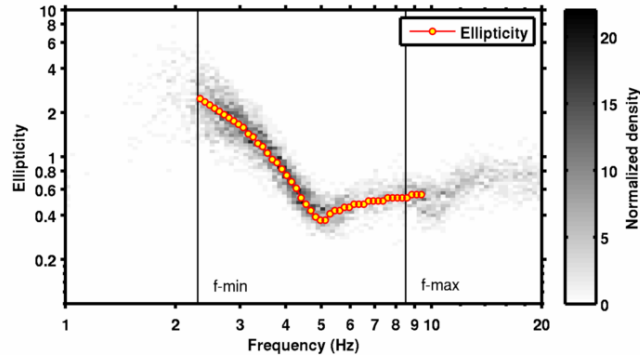


Figure 2.12: Comparison of the Rayleigh wave fundamental mode obtained from Array 01, 02 and 04 with the results from the SBB array. The differences in velocity are explained by the different location. Arrays 02 and 04 have been setup at the basin edges, where the bedrock is at shallow depth. With vertical lines are indicated the fundamental frequencies at each array location.

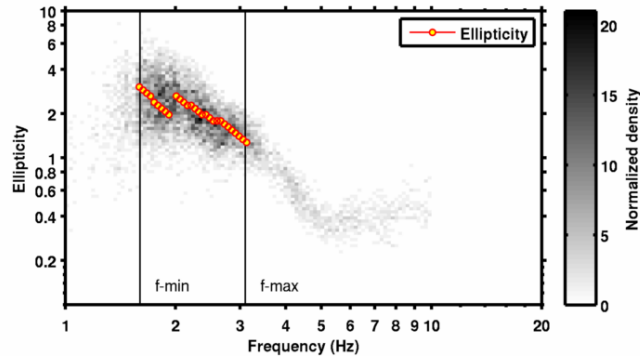
2.5.2 Rayleigh ellipticity function from array analysis

Poggi and Fäh [2010] demonstrated the possibility of using the spectral information from the three-component f - k transform to obtain an estimation of the Rayleigh-wave ellipticity function. The method relies on the assumption that a maximum in the f - k spectrum is statistically representative of the power amplitude of the picked signal. If three components analysis is performed, the particle motion can then be evaluated for each wave contribution separately. The main advantage of such a procedure is the possibility of separating out the contributions of higher modes, when they are present and sufficiently energetic. The frequency range where such a procedure to obtain an estimation of ellipticity is possible, however, is controlled by the resolution of the f - k method, which in turn is limited by the array geometry (e.g. the minimum and maximum inter-station distances). The number of receivers, in particular, has the strongest impact on the result. It controls the capability to distinguish between close signals in the f - k domain. In this case, the 14 receivers used for the survey appeared to be sufficient to retrieve the ellipticity information.

From the analysis of Ring 1's configuration, good results were retrieved (Fig. 2.13a). In this frequency region, only the Rayleigh fundamental mode is observable. The corresponding ellipticity is well defined, with a clear minimum trough at 5 Hz. A good match is found by comparison with the ellipticity



(a)



(b)

Figure 2.13: Rayleigh-wave ellipticity from three-component array analysis of ambient noise. In a) the result from ring 1 of the SBB array and in b) the one from ring 2 is shown. Frequency bounds f -min and f -max are derived from the resolution limits of the f - k method.

function estimated using the wavelet-based approach (Fig. 2.14). With this method, a mean curve was obtained by log-averaging all the H/V curves from the stations of the array. Ring 2's configuration results were less clear (Fig. 2.13b). In the range of resolution, two branches for possible Rayleigh waves can be identified with f - k analysis. The phase velocity curves (Fig. 2.11) of the fundamental and first higher mode are very close between 2 and 4 Hz and close to apparent intersection at 4 Hz. This situation leads to a certain difficulty in separating out the energy of the two contributions using the f - k method, and the ellipticity is here not easily identifiable. The result is in disagreement with that from wavelet H/V spectral ratios. Most probably, using an increased number of receivers, the ellipticity of the two modes could be better resolved. To avoid biased results and misinterpretations, we did not the use of the results

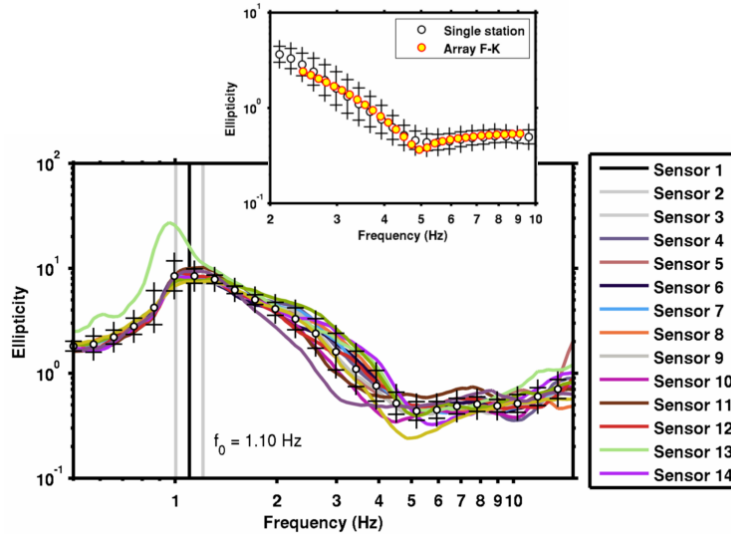


Figure 2.14: Results from wavelet H/V spectral ratio performed on all the 14 stations constituting the SBB array. The average value from all curves is considered as representative of the Rayleigh-wave ellipticity function in this area. A good match is found with results from the array analysis on ring 1.

from Ring 2.

2.6 Inversion of dispersion curves

The inversion of surface-wave dispersion curves consists in a multiple dataset fitting procedure to provide an estimation of the local velocity structure. As also required by array processing, one-dimensionality is assumed for the inversion model. This is generally valid for real structures in case of insignificant basin edge effects and weak lateral variations. In the case of Lucerne, such approximation is acceptable in most parts of the urban area. Due to the high non-linearity and non-uniqueness of the problem to solve, the most common approach is simply to perform a direct search over the parameter space, until some minimization criteria - that described the fitting with the input data - is reached. Bounding the parameter search space and/or providing some additional a-priori information help to reduce the spread of the final solutions. Each dispersion mode, from both Rayleigh and Love wave dispersion, represents a different dataset to be fitted. Each dataset can be characterized by a different length (number of data points) and sensitivity to the models parameters. This effect can be overcome by the use of a data-weighting scheme

that, on the other side, is generally difficult to quantify. Very often a simple trial-and-error approach is used to define the weights. Search parameters are usually, in the case of purely elastic models, the thickness, V_p , V_s and density of each layer. The sensitivity of dispersion curves to the density parameter is however very low, and commonly it is defined a-priori. The number of layers is selected in relation to the expected complexity of the model and the maximum investigated depth.

2.6.1 The inversion scheme

To invert dispersion curves for the one-dimensional velocity profile, a hybrid Monte-Carlo optimization scheme was developed. It combines different types of direct search methodologies to drive the inversion to converge to a minimum misfit solution. At first, a pure Monte Carlo search is performed to investigate the whole parameter space. In this stage, about 100000 models are randomly generated and the best fitting model extracted. The parameter space search boundaries are then refined with respect to the best fitting model, according to a specified rate of convergence. Following this, the random search is iterated several times and for a given number of models. As it was experienced with synthetic and real datasets, reliable results were obtained with 200 iterations of 500 models each, with a convergence rate of the parameter bounds of 0.005%. In a final stage, the data fit is refined through a Nelder-Mead simplex search approach (Lagarias and al. 1998). In order to do this, it is assumed that the n-dimensional misfit function is strictly convex in the proximity of the retrieved minimum, where the exact solution is expected.

For the inversion, both the Rayleigh-wave (fundamental and first higher mode) and Love (fundamental) dispersion curves from array analysis were used. In addition the ellipticity information was used. Our first goal is the derivation of generic smooth velocity profile down to and into the bedrock. The uppermost low-velocity layer is variable in the study area. From the geological interpretation of borehole data [Mengis and AG, 2007b] we can assume that the site of the train station corresponds to the area where this soft layer has its maximum thickness. Combining the different datasets helped in reducing the scattering (and consequently the uncertainty level) of the final solution. Love-wave dispersion, in particular, represents a formidable constraint for the shear-wave velocity profile. Indirectly, this reflects also on the P-wave information during the combined inversion. As a matter of fact, both the V_s and V_p parameters non-uniquely control Rayleigh-wave dispersion. Constraining the first one will then increase the sensitivity of the second, refining the solution

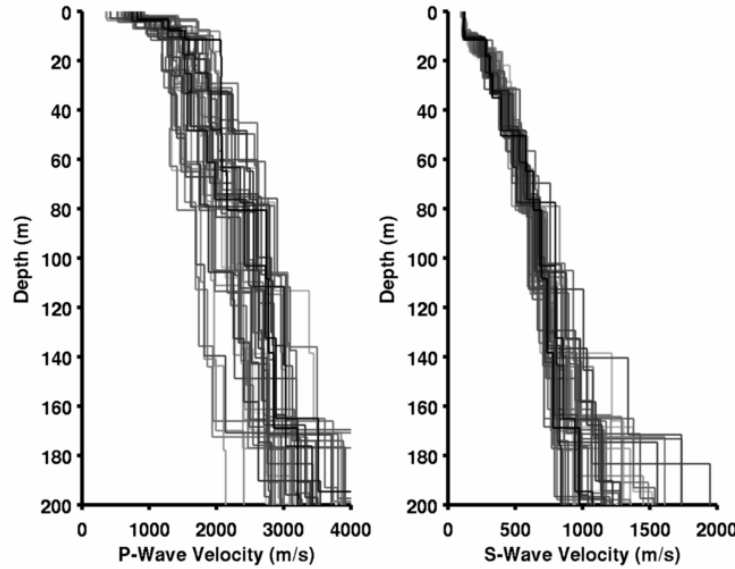


Figure 2.15: Vs and Vp velocity models from the inversion of surface wave dispersion. The profiles are realistic down to a depth of approximately 120~140m. Below this depth, the inversion is no more constrained from the available data. In the plot, the best-fitting models of 50 separated runs are shown. It is interesting to notice that the velocity jump at about 10-15m is a common feature.

to a narrower parameter space. Furthermore, the Rayleigh part has been weighted by a factor 2 during the inversion. This value has been established after several trials and provides a faster convergence to the solution.

A large number of inversion tests have been performed (about 50 runs with random initial seed), to minimize the risk of relying on solutions trapped in some local minimum of the misfit function. The two inverted velocity profiles smoothly increase the velocity with depth (Fig. 2.15). The fit between inverted and original curves is good overall (Fig. 2.16). The velocity jump at around 4Hz in the fundamental mode of Rayleigh waves is explained by a velocity contrast (in both Vp and Vs profiles) at a depth of about 10-15m. Both profiles appear to be reliable up to depths of approximately 120~140m. Beyond this value, the dispersion information is progressively incapable to correctly constrain the velocity profile. No resolution is obtained on the interface between soft sediments and the bedrock.

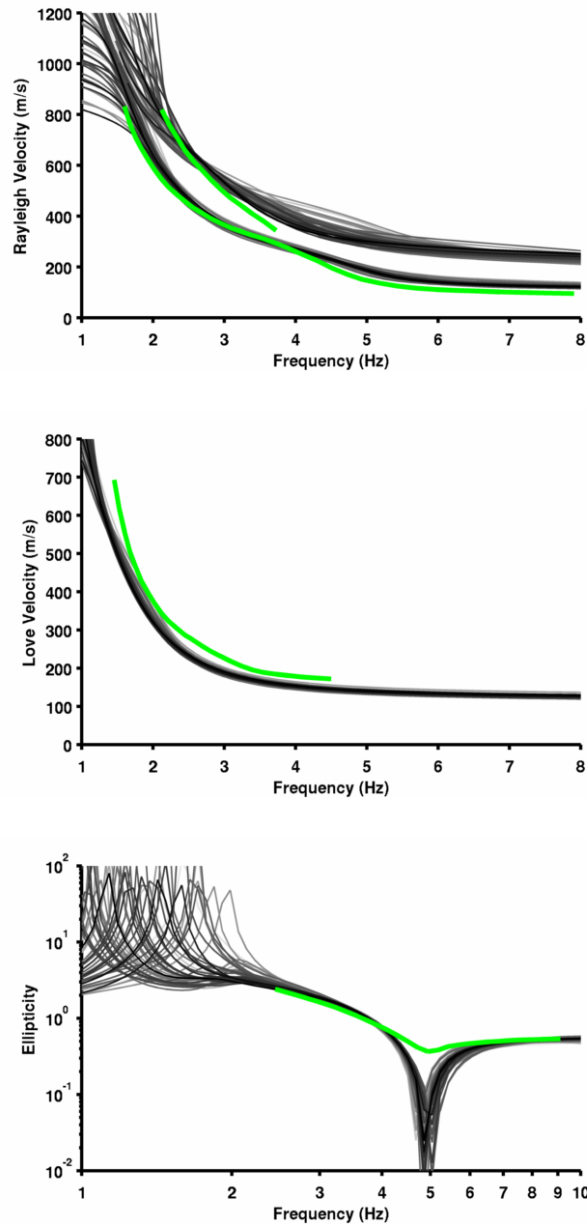


Figure 2.16: Combined inversion of dispersion and ellipticity information. In green the measured data, in gray the inverted models from the separate 54 runs are shown.

2.6.2 Velocity profile in gradient form

In order to characterize the seismic response of the entire sedimentary basin, it is necessary to define a generic velocity model (V_s or V_p) that describes the general variation of the seismic velocity as function of depth in the sediments. The model should be simple and sufficiently general to be extended over the whole basin structure. As a base for building this generic model, we used the velocity estimates from inversion of surface-wave dispersion. However, some simplifications were necessary. The inverted profiles, as they are, include some characteristics that are undesirable for a generic model. For such a reason, it was decided to simplify the retrieved model using some functional form capable to describe the general trend of velocity variation, but without being affected by too large complexity. To do so, a gradient equation has been established in the form [Poggi and Fäh, 2010]:

$$V_s(z) = (V_{sMax} - V_{sMin}) \left[1 - a \left(\frac{z_0 - z}{b} \right) \right] + V_{sMin} \quad (2.5)$$

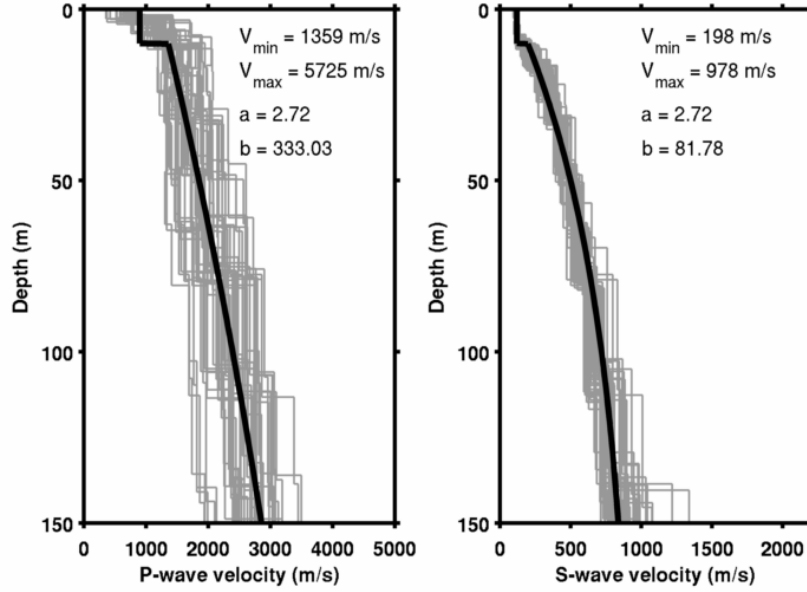
where V_{sMax} and V_{sMin} are respectively the expected maximum and minimum shear-wave velocities for the sediments, while a and b are curvature coefficients. The shallower low-velocity layer is then modelled by mean of a single layer of constant velocity and 10m thickness.

Fitting the gradient function to the inverted velocity model is done by means of a simple optimization procedure. Free parameters for the search are the velocity bounds (V_{sMin} and V_{sMax}) and the curvature parameters a and b of the function. The optimal model minimizes the velocity residuals between the input profile and the gradient in a depth range between 0.5 and 200m. In Fig. 2.17 the V_p and V_s gradient velocity profiles obtained with such a procedure are presented. The gradient is selected to have a reasonable fit also with the dispersion and ellipticity information.

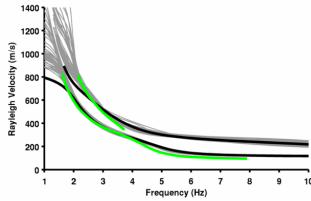
2.7 Rayleigh wave ellipticity inversion

2.7.1 SBB station: inverting the whole ellipticity function

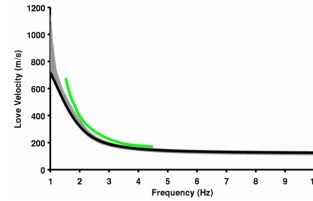
It was observed that inverting Rayleigh wave ellipticity together with surface wave dispersion information helps in reducing the variability of the inverted models, excluding some solutions incompatible with such a constraint [e.g. Arai and Tokimatsu, 2005]. Combined inversion of the ellipticity function and



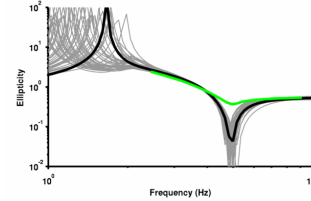
(a)



(b)



(c)



(d)

Figure 2.17: Approximating the inverted V_s (left) and V_p (right) velocity profile by mean of a simplified gradient function (a, black line). The fit is obtained through a global optimization procedure, accounting also for the consistency with the dispersion and ellipticity data (b,c,d).

dispersion characteristics clearly improves the resolution of the bedrock on simple models, with a few layers over a half space. In more complex models, with an increasing number of layers, the inversion often results in a smoothed profile, where the bedrock interface is not clearly identifiable [Fäh et al., 2009a].

To face such a drawback we adopted a two-step inversion approach. As already stressed, the velocity profiles of the soft sediment part (in term of V_p and V_s) are obtained from the combined inversion of Love and Rayleigh wave dispersion, and the ellipticity function. The velocity model was then

simplified using a generic model with a shallow constant-velocity layer and a velocity gradient. This describes the general variation of velocity over depth, not accounting for local variability (small velocity inversion and/or jumps). In a second stage, the singularity or peak of the ellipticity function f_0 -Ell (obtained from array analysis and/or single station wavelet-H/V) and the derived average ellipticity as shown in Fig. 2.14 are added as additional information, and are used together with the derived generic gradient model to constrain the bedrock depth and velocity.

Fitting the ellipticity information is done using a combined minimization procedure. A total misfit is computed as the result of fitting the fundamental frequency f_0 -Ell and the whole ellipticity function separately. Only the low-frequency part of the ellipticity function is used for the fit, since the high frequency part is already constrained in the profile. The idea behind such an approach is that fitting f_0 -Ell will constrain the bedrock depth, while fitting the amplitude of the ellipticity function helps in refining the velocity contrast between the soft sediment section and the basement. Additional weights (W^0 and W^1) can be moreover provided to drive the inversion.

$$M_{Fit} = W^0 \left| f_0^{Dat} - f_0^{Syn} \right| + W^1 \sum_{i=1}^N \frac{\left(\log \left(Ell_{f_i}^{Dat} \right) - \log \left(Ell_{f_i}^{Syn} \right) \right)^2}{N} \quad (2.6)$$

Finally, in order to reduce the number of free parameters for the inversion, a constant Poisson ratio of 0.3 was used to constrain the V_p velocity of the bedrock.

Clearly, by using such a simplified approach, not all features of the measured ellipticity can be reproduced and fit all the small features of the measured data. However a reasonable approximation is obtained (Fig. 2.18). In particular, other than the peak corresponding to the singularity of the ellipticity, a secondary peak is visible around 2.5Hz . This peak is compatible with the irregularity of the measured ellipticity function in this frequency range, where a moderate inflection of the right flank is observed. The inverted model is well constrained from the data at high frequencies.

Several tests were performed for the location of array SBB. In most of the cases we found a bedrock depth of about $130\sim 150\text{m}$ and a bedrock average V_s velocity of about 2200m/s . The result is compatible with a geological survey performed on the area [Mengis and AG, 2007a]. The most important test relates to the frequency band of the ellipticity curve derived from H/V with the wavelet-based method, which is most reliably corresponding to the real ellipticity. During the NERIES project the wavelet-based method has been

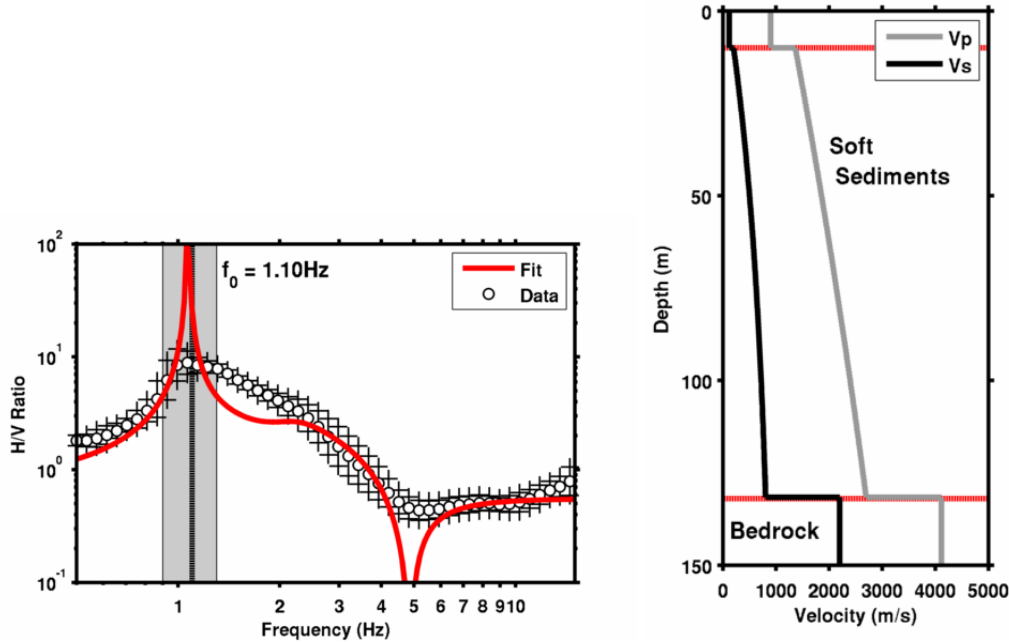


Figure 2.18: Inverting the bedrock depth and velocity for the SBB array from wavelet-based H/V ratios (assuming that we measured ellipticity). Inverted depth is in agreement with interpretations from previous geological and geophysical surveys [Mengis and AG, 2007a].

tested on synthetic noise, with resulting ellipticity estimates much closer to the theoretical ones than the raw H/V curves. Reliable results were obtained for all models for the right flank of the H/V curve, between the first peak at the fundamental frequency of resonance and the first trough at higher frequency. This restriction of the ellipticity information to the right flank of the H/V curve was therefore also tested, also including the peak to constrain the singularity of ellipticity function at f_0 -Ell. The results obtained (not present in this paper) were very similar to the ones shown in Fig. 2.18, with a depth and velocity in rock that is almost the same.

2.7.2 Global inversion of ellipticity peaks

From the analysis of the SBB array, a generic velocity model of the sedimentary structure below the train station of Lucerne has been obtained from inversion of surface waves information. Using ellipticity, then, it was possible to constrain the bedrock depth and velocity under this area. Because of the limited size of

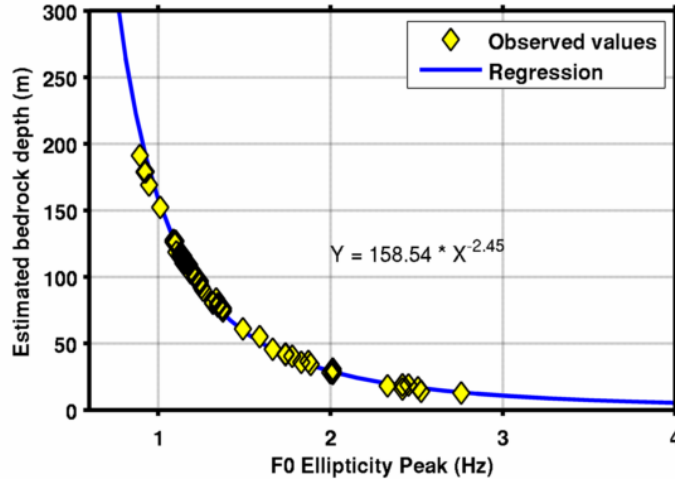


Figure 2.19: Globally inverting the ellipticity peaks (f_0 -Ell) from wavelet-based H/V ratios helps in minimizing the uncertainties introduced by the inversion procedure. An exponential regression is used to describe the relation between the frequency value and inverted depth.

the basin, similar depositional conditions and geological settings are expected over the whole area. For this reason it appears reasonable to assume the retrieved velocity model to be roughly representative, not only of the area surrounding the train station, but also for the generic basin profile. Clearly, local variations might be present (e.g. lateral variations, ground water), but these are assumed to be in the order of the error of the method.

Under this assumption, the only variable and unknown parameter is the bedrock location under the different parts of the basin. To reconstruct the 3D bedrock geometry, the ellipticity peaks from single station measurements were used. A subset of single station measurements was selected within regions of the sedimentary basin where no strong 2D/3D effects are expected (basically the inner part). The selection was chosen setting an approximate upper-bound for the ellipticity f_0 -Ell of about 4Hz . For these stations then, the ellipticity peak was inverted using the generic velocity model in gradient form and the bedrock velocity of 2200m/s . Consequently, the only free parameter of the inversion is the bedrock depth at each station location.

As proposed by Parolai et al. [2002] for f_0 -SH, a functional correlation between the inverted depths and the corresponding ellipticity f_0 -Ell was then established (Fig. 2.19) using regression. The relation is exponential as follows:

$$Z_{\text{Bedrock}} = 158.54(f_0^{\text{Ell}})^{-2.45} \quad (2.7)$$

Establishing such relation allows the rapid inversion of the bedrock depth in wide areas for which an estimation of the ellipticity f_0 -Ell is available, without the necessity of a complex inversion approach. The relation has then been used to convert the f_0 -Ell map of Fig. 2.9 into the corresponding bedrock map (Fig. 2.20). We do not expect the correlation to be strictly valid at high frequencies ($>4Hz$). Therefore, portions of the f_0 -Ell map with frequencies above $10Hz$ have been considered outcropping bedrock. The retrieved bedrock geometry reflects the distribution of f_0 -Ell along the area. The largest depth obtained from the correlation is $212m$ in the eastern part of the basin. The central area of the basin has variable thickness, with an average value of about $120m$. Bedrock depth is clearly decreasing while approaching the basin edges (e.g. profiles in Fig. 2.20).

2.7.3 Comparison with the simplified f_0 -resonance approach

A common approach to estimate the bedrock depth from H/V spectral ratios is to assume the peak of the ellipticity function to be a proxy for the SH-wave fundamental frequency of resonance [Yamanaka et al., 1994; Hinzen et al., 2004]. In such a way, if the velocity model is simplified to a one-dimensional case of a single soft-sediment layer over the bedrock half-space, the following equation is valid [Roesset, 1970]:

$$f_0^{SH} = \frac{V_{Soft}}{4 \cdot Z_{Bedrock}} \quad (2.8)$$

This equation relates the SH-wave fundamental frequency of resonance f_0 -SH with the V_s velocity of the equivalent layer and the bedrock depth $Z_{Bedrock}$. Such an approach, however, often results in an oversimplification of the problem [Dobry et al., 1976]. In particular, the choice of the proper “average” V_s velocity is not straightforward. In most cases, shear-wave velocity is estimated at shallower depths only (e.g. $30m$) from geotechnical characterization or small-scale geophysical surveys, and then assumed to be constant down to bedrock. This approach systematically underestimates the velocities of basins having thick sedimentary cover, resulting in an underestimation of the bedrock depth.

In order to underline the entity of such deviations, bedrock depths obtained by the proposed method have been compared with those from the simplified

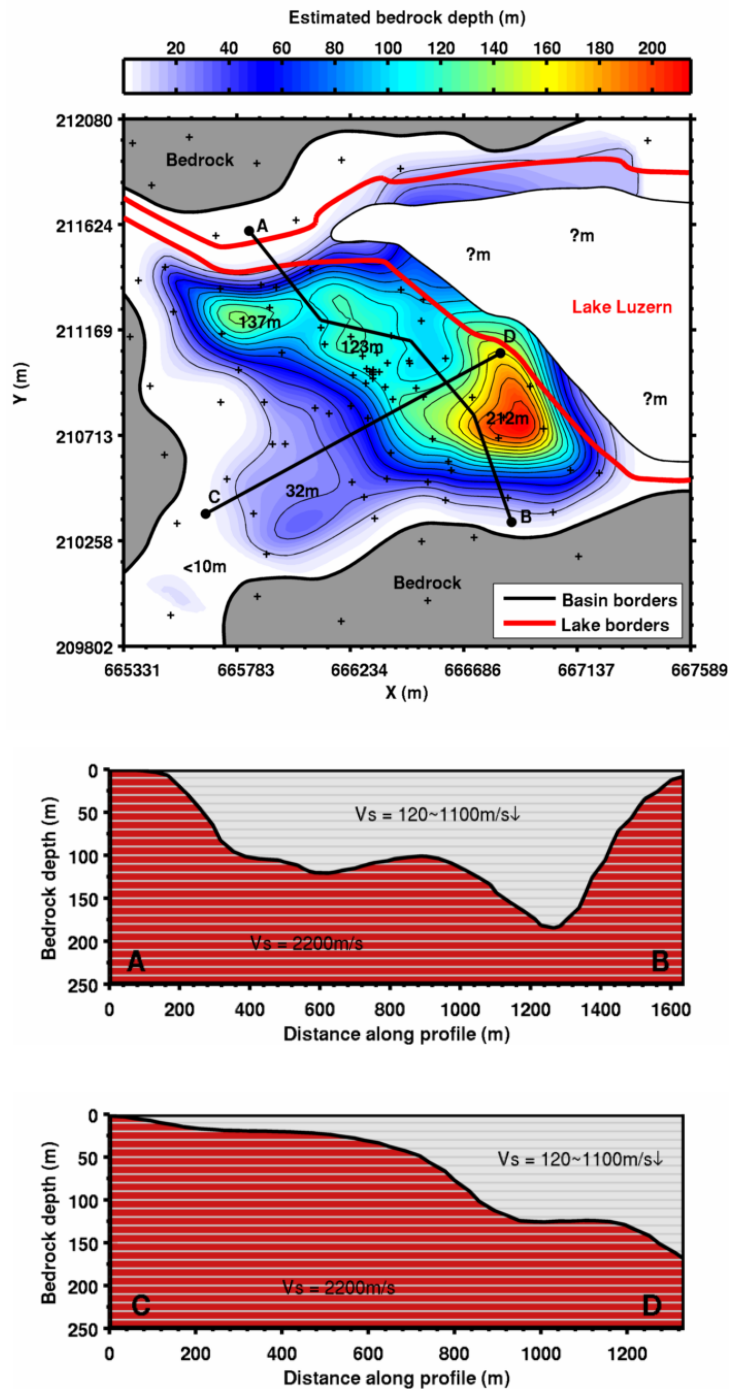


Figure 2.20: The functional correlation between ellipticity peak and inverted bedrock depth allows the reconstruction of the bedrock geometry, from the interpolated f_0 -Ell map.

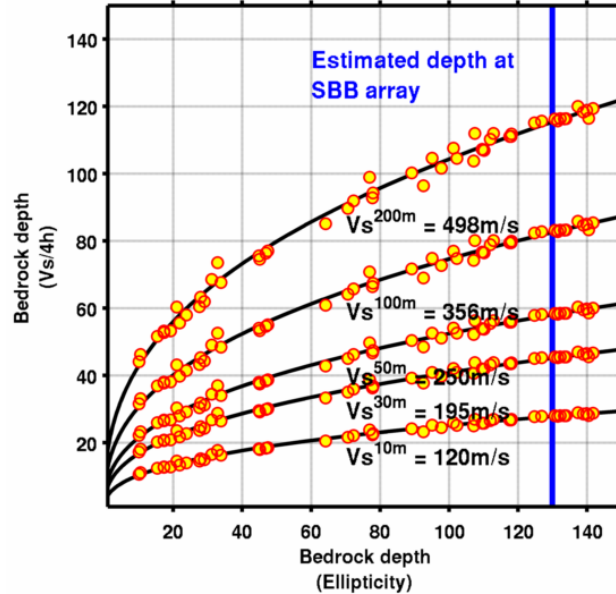


Figure 2.21: Bedrock depths estimated using the ellipticity peak have been compared with those obtained from the simple equation $F_0 = Vs/4h$ assuming a layer over half-space. Different average velocities were used for the comparison, averaging velocity over the depths 10, 30, 50, 100, and 200m. For the site of the SBB array, the results of this simplified method always underestimate the one from the proposed one. The correct bedrock depth of 140m at the location of seismic survey cannot be retrieved with such oversimplified approach. Black lines are lognormal regressions to underline the trend of each set.

approach (Fig. 2.21). Different V_s velocities were used for the test, averaging the available velocity profile at the depths of 10, 30, 50, 100 and 200m. As expected, large differences are present. In particular, if compared with our reference array location, for which the bedrock depth is estimated to be about 140m, the common V_s30 averaging (common in engineering applications) produces a significant underestimation of depth. The error however decreases while increasing the averaging depth.

2.8 Frequency-dependent amplification model

2.8.1 Pseudo-3D modeling of amplification

The frequency-dependent S-wave amplification map of Lucerne is computed using the 3D model derived from ambient vibration techniques. Considering

the uncertainties of the model and the assumptions, it was decided to first not to use any 2D/3D wave-propagation simulation for the computation. The level of knowledge on the model is not yet sufficient, specifically lacking the information related to the variability of the shallow low-velocity layer in the first 10-15m.

A robust approach, nevertheless simple, is to use a gridded one-dimensional modelling. This approach consists in subdividing the three-dimensional model in vertical soil-column. The basin area has been discretized using a horizontal grid of 100 by 100 cells. For each of these, a one-dimensional modelling of the SH-wave amplification is done. This approach is generally valid in cases of moderate variation of the elastic and geometric properties of the model. Since 2D resonance patterns involve both vertical and horizontal interferences, they can only appear in relatively deep valleys. To identify valleys whose seismic behavior is characterized by 2D resonance, Bard and Bouchon [1985] introduced the concept of the critical shape ratio. Assuming a sine-shaped basin, the shape ratio is defined as the ratio of the maximum sediment thickness h to the valley half-width l . For arbitrarily shaped valleys, this parameter is replaced by the 'equivalent' shape ratio $h/2w$, where $2w$ is defined as the total width over which the sediment thickness is greater than half its maximum value. The critical shape ratio depends on the velocity contrast between bedrock and sediment fill. If the shape ratio of a valley is above the critical value, its seismic behavior at low frequencies will be characterized by 2D resonance. The critical shape ratio depends also on the wave type; its value is higher for P-waves than for SH- and SV-waves. Using 800m for $2w$ and 200m for h in Luzern, we can assign a shape ratio of about 0.25. The velocity contrast between bedrock and sediment is in the ranges from 2 to 5. This site is clearly located outside in the domain of 2D resonance for the SH-case. However, basin edge effects still play a major role in the Luzern area, and they are not modelled by 1D site response.

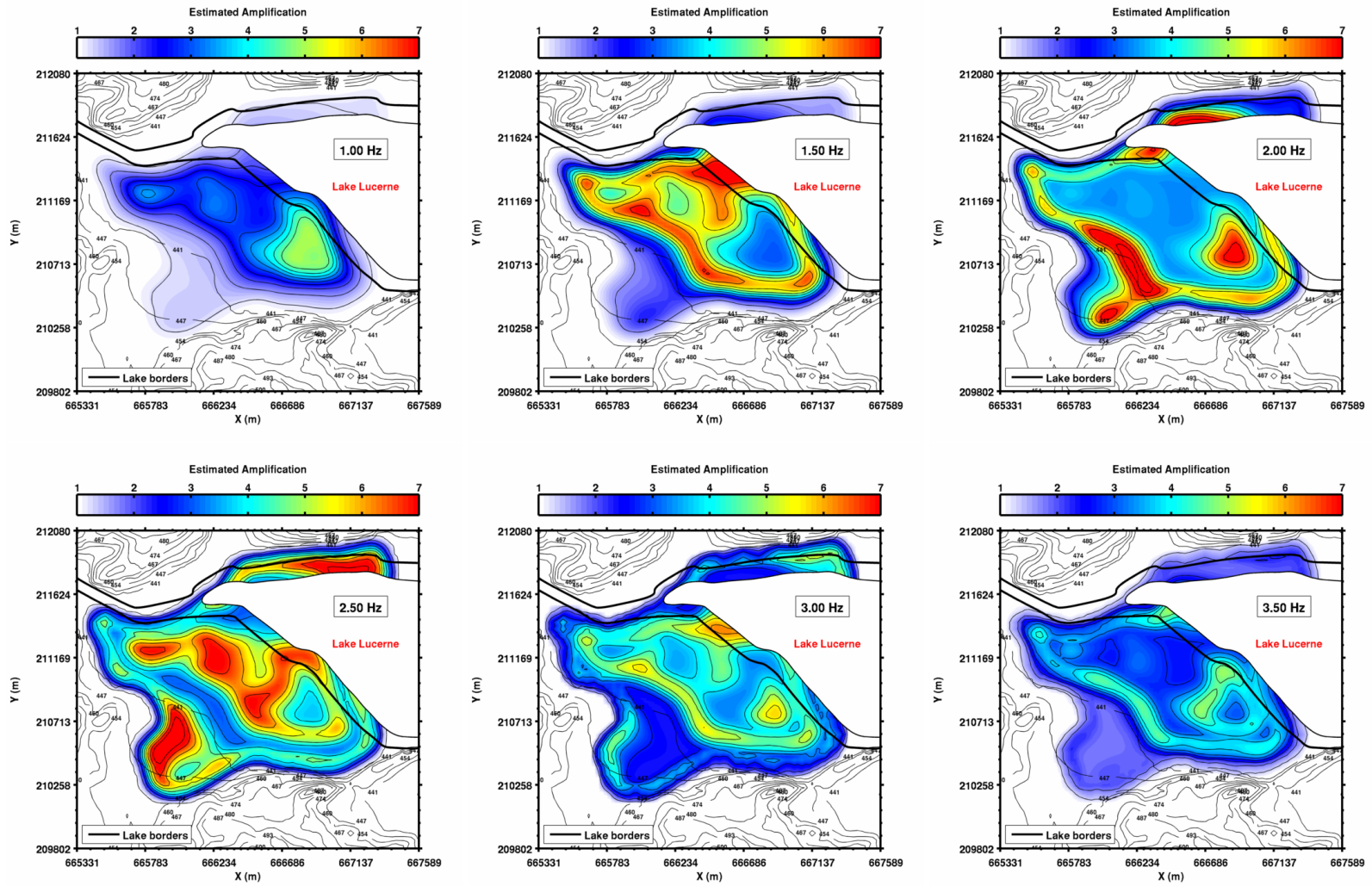


Figure 2.22: SH-wave transfer function amplification model of the Luzern basin using a gridded pseudo-3D approach. Here some frequency snap-shots from 1 to 3.5Hz are shown. It is clearly possible to observe the migration of the first two resonance modes from the centre to the basin edges with increasing frequencies.

2.8.2 Using the SH-wave transfer function

To compute the one-dimensional amplification function at each cell, we used the SH-wave transfer function formalism for vertical wave propagation, following the Knopoff layer-matrix formulation [Knopoff, 1964]. The constant bedrock velocity of 2200m/s and density of 2500kg/m^3 are used as reference rock condition. No information about anelastic attenuation is available from ambient vibration analysis. We establish for the sediment part a generic profile of the S-wave quality factor (Q_s) by mean of an exponential function. The profile varies between $Q_s=10$, in the shallow layers, to 30 at 150m . For the bedrock, a constant Q_s value of 50 was used. Amplification functions were computed for a frequency range between 0.5 and 15Hz .

The simple one-dimensional modelling shows interesting results. From low to high frequencies, it is possible to follow the development of the fundamental mode of resonance, progressively moving from the basin centre to the edges (Fig. 2.22). Higher modes of resonance are also developed. Mapping the maximum amplification at the fundamental frequency of resonance shows that the highest amplification (about 9) is found in the south-western part of the basin (Fig. 2.23), where the bedrock depth is estimated to be between about 30 and 60m . Large parts of the basin show amplifications between a factor of 6 and 7. These values of amplification depend strongly on the sediment-bedrock velocity jump of the adopted model. The amplification at higher frequencies is depending on the Q model. Only earthquake observations can help to better define these uncertainties.

2.8.3 Comparing the ellipticity peak to SH-wave f_0

The map of the ellipticity fundamental-frequency from wavelet analysis is now compared with the variation in the SH-wave fundamental-frequency modelled using the transfer function formalism (Fig. 2.25a). Away from the basin edges, it is possible to observe a generally good match between the two. The strong differences at the borders can be justified by the limitations of the proposed method, where the one-dimensional approximation (for the ellipticity inversion and transfer function modelling) might not be fulfilled, and measured f_0 -Ell are affected by 2D/3D effects. For this reason, we decided to define an f_0 value of 4Hz value as a limit to separate the more reliable part of the model. This roughly corresponds to a bedrock depth of about 20m .

Comparing more accurately the two frequency parameters (Fig. 2.24b and 2.24c) in a range between 1 and 4Hz , some small local deviations can be observed. In particular, the SH-wave f_0 tends to be slightly (but consistently)

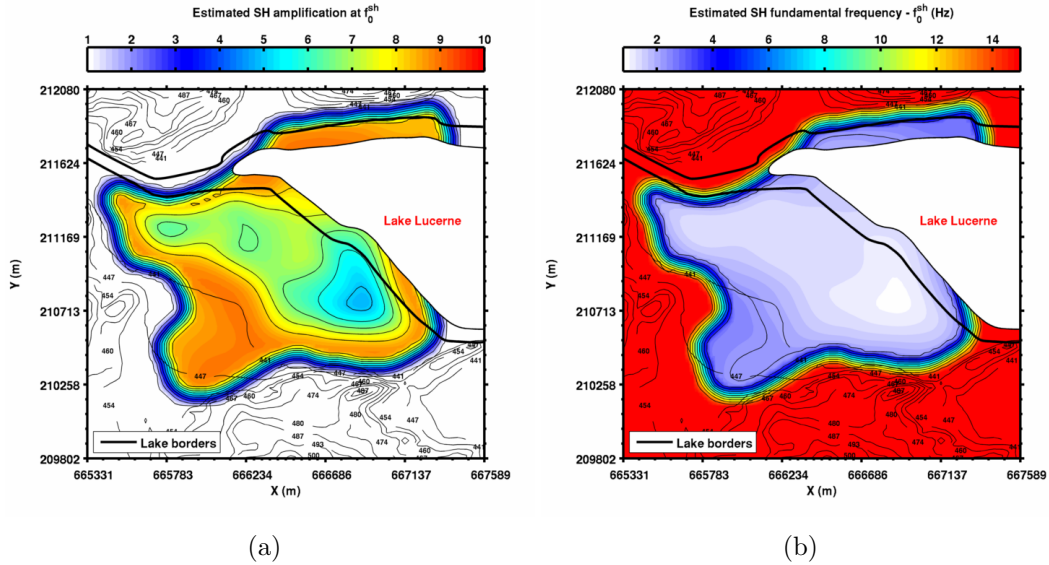
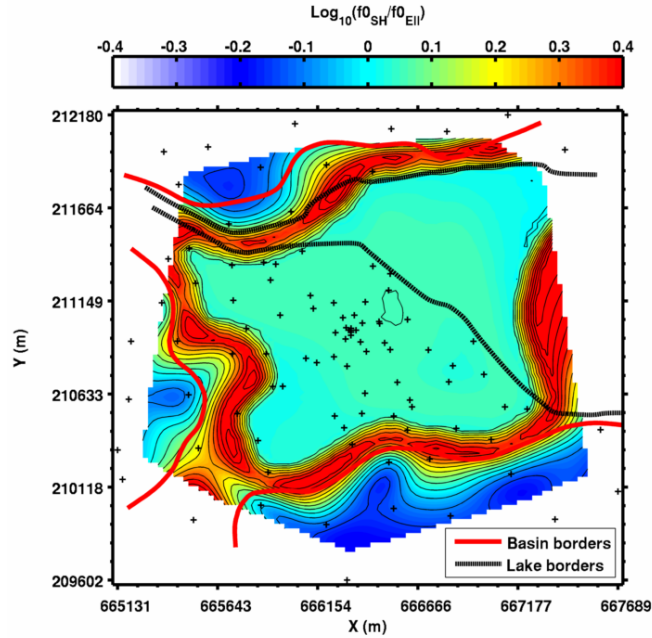


Figure 2.23: Maximum amplification expected (a) at the fundamental frequency of resonance of (b) the SH-wave transfer function in the study area. Maximum amplification is experienced where the bedrock depth is roughly between 30 and 60m.

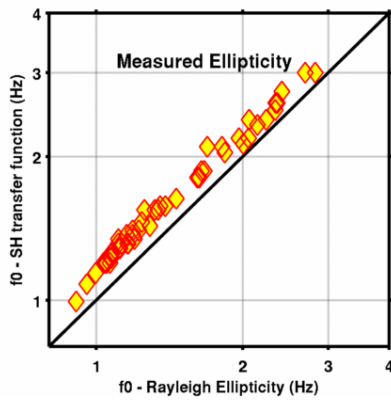
larger than that from ellipticity in a range between 1 and 3Hz. This is generally in agreement with what already was observed in Fig. 2.8 by comparison of different H/V spectral ratio methods. This provides also a confirmation of the imperfect equivalence between f_0 from ellipticity (or better the singularity of the ellipticity curve) and f_0 from the SH transfer-function. As outlined by Malischewsky and Scherbaum [2004] these two parameters, often considered equivalent in literature, belong to different phenomena and might consequently show some deviations. Nevertheless this is not relevant for practical application, because such deviations are usually within the range of uncertainties of the methods. These findings, however, might be used in future applications as additional information.

2.8.4 Using the quarter-wavelength amplification

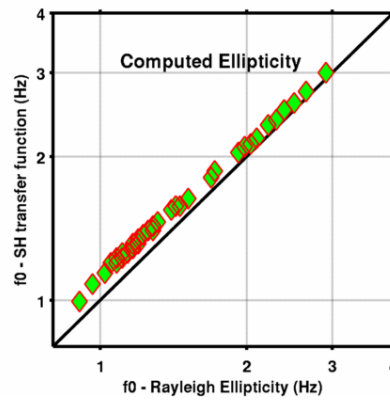
The main disadvantage in using the SH-wave transfer function is the presence of very sharp resonance peaks when strong contrasts of seismic impedance are present along the velocity profile. This is usually the case of the layered models obtained from inversion of geophysical data. This behavior, however, is often not observed in nature where the lithological interfaces (e.g. con-



(a)



(b)



(c)

Figure 2.24: Comparison between ellipticity f_0 -Ell from single station measurements and computed SH-wave fundamental frequency of resonance for the basin area (a). Strong deviations are experienced close to the basin edges, where the ellipticity f_0 is usually higher than 3Hz . Below 3Hz , deviations are less pronounced, and only a slight overestimation of the f_0 -SH can be observed (b,c). In (b) theoretical f_0 -SH are compared to the observed f_0 -Ell, and in (c) theoretical f_0 -SH are compared to the theoretical f_0 -Ell at the site of the measurements.

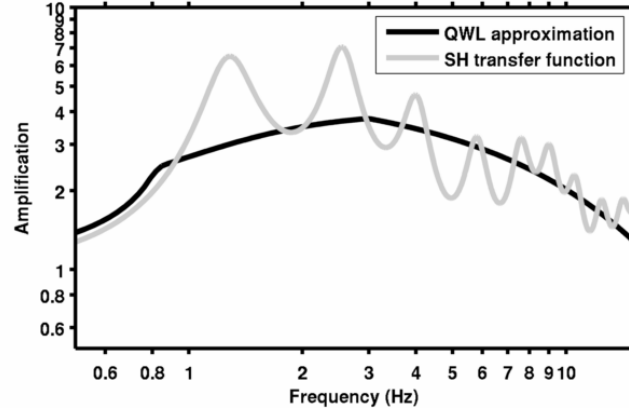


Figure 2.25: Comparison of seismic amplification functions using the SH transfer-function formalism and the quarter-wavelength approximation (QWL). For this last approach, attenuation has been applied separately using a travel-time decay function.

tact bedrock-soft sediments) are characterized by smoother variations of the velocity properties, and wave-fields are not composed only of vertically propagating SH waves, but also surface waves and body waves of different kinds. To model smooth amplification behavior, the quarter-wavelength approximation has been applied [Joyner et al., 1981].

$$A^{QWL}(f) = \sqrt{\frac{\rho^C V_s^C}{\bar{\rho}^{QWL}(f) \bar{V}_s^{QWL}(f)}} \quad (2.9)$$

Here \bar{V}_s^{QWL} and $\bar{\rho}^{QWL}$ are the quarter-wavelength average velocity and density of the sediment part, while V_s^C and ρ^C those for the bedrock reference.

This method has the advantage of being relatively insensitive to sharp velocity contrasts. The amplification functions obtained with this method are usually smoothed variants of the SH-wave transfer function for the elastic case, nevertheless preserving the general trend in amplification. Conversely, the disadvantage of the method is the impossibility of identifying any resonance. Attenuation has to be added separately to the function by means of frequency-dependent decay functions. We use a travel-time approach, such that the final amplification results in:

$$A(f) = A^{QWL}(f) e^{-\pi f \left\{ \sum_{n=1}^N \frac{H(n)}{V_s(n) Q_s(n)} \right\}} \quad (2.10)$$

where $H(n)$ is thickness, $V_s(n)$ the velocity and $Q_s(n)$ the quality factor of

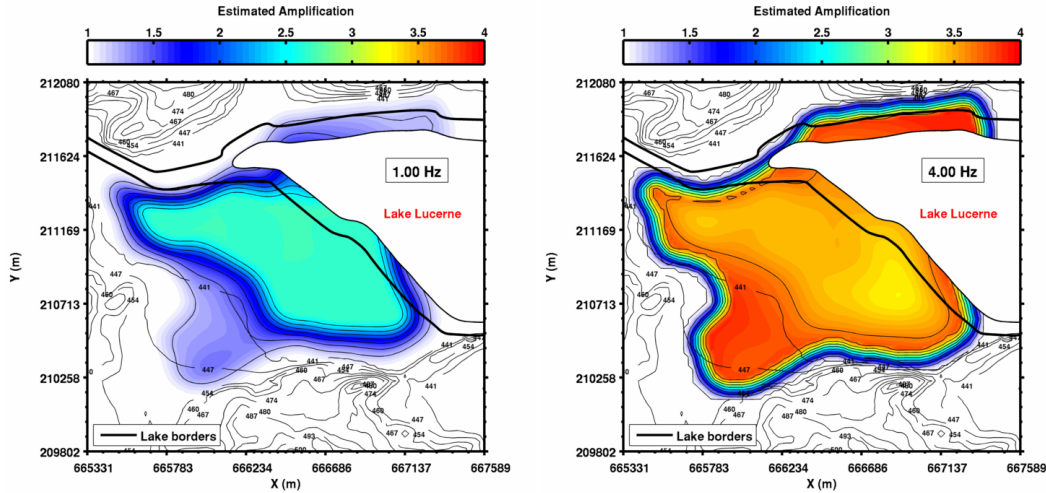


Figure 2.26: Map of seismic amplification computed using the quarter-wavelength approximation and travel time attenuation. In respect to the SH-transfer function modelling, the average level amplification is lower and no resonance peaks can be identified.

the n^{th} layer.

Mapping amplification using the quarter-wavelength shows considerable differences in respect to the transfer function approach. The average level of amplification is strongly reduced and no resonance modes are visible any more (Fig. 2.25). While this last point is advantageous for some aspects, the decrease in the amplification level will underestimate the true response of the basin shown in Fig. 2.26. Within this context it is then reasonable to consider the presented methods as complementary, being the quarter-wavelength amplification a lower bound when assuming vertically propagating SH waves.

2.9 Discussion and conclusions

In the present study we deal with the problem of optimizing the characterization and subsequent use of the Rayleigh wave ellipticity information from ambient noise recordings. The main goal is to improve the level of accuracy in assessing the velocity structure of sedimentary basins, in particular the bedrock depth. As a direct consequence, more realistic amplification can be modelled.

Two techniques to evaluate the Rayleigh ellipticity function have been tested, a single station method and an array method. The two approaches provide comparable results, in the limit of resolution of the methods. Elliptic-

ity information obtained in this way can be used as an additional constraint to invert for the velocity structure. The use of wavelet time-frequency analysis to perform H/V polarization analysis has the clear advantage of minimizing the effect of SH-wave contribution, compared to the classical H/V method. In cases of large velocity contrasts between sediments and bedrock, the result can be reasonably considered representative of the Rayleigh-wave ellipticity function. The inverted models are well explained by the curves produced in such ways. Additionally, by comparison between the classic method to compute H/V ratios and the wavelet-based one, it is possible to estimate the relative energy contribution between the SH and PSV components. The method, however, is not capable to separate the contribution from different modes. We provided a confirmation of the imperfect equivalence between f_0 from ellipticity (or better the singularity of the ellipticity curve) and f_0 from the SH-wave transfer-function, as outlined by Malischewsky and Scherbaum [2004]. The two parameters, often considered equivalent in literature, belong to different phenomena and might consequently show some deviations. Nevertheless this is not relevant for practical engineering applications, because such deviations are usually within the range of uncertainties of the methods. These findings, however, might be used in future applications as additional information.

Estimating the Rayleigh wave ellipticity function by means of array analysis provided comparable results with respect to those obtained from wavelet approach. The main disadvantage, however, is the limited frequency resolution of the method. This strictly depends on the number of sensors employed for the surveys and the array size. In this case, the 14 receivers employed appear to be sufficient, but not optimal. To improve the final result, we recommend an increased number of receivers.

A two-step approach is presented for the combined use of dispersion and ellipticity information from ambient noise recordings. Such an approach enhances the resolution of classical array techniques on deep structures, especially on the depth of the bedrock. This is particularly suitable in densely populated areas, where only single station measurements are possible and more sophisticated techniques are generally difficult or even impossible. Moreover, it is cost effective, which makes it suitable for investigations over large areas. Uncertainties are the local variability in the velocity structure (e.g. in the uppermost low-velocity layer in the Lucerne area), the influence of 2D/3D effects at the basin edges or the uncertainties in attenuation might affect the quality of the 3D structural model and therefore the estimated amplification. In particular, estimation of confidence bounds for the inverted velocity profiles has to be defined by further independent measurement.

The evaluation of the local seismic response has been carried from the inverted velocity model using the 1D approximation. The amplification functions have been calculated using both the SH-wave transfer function approach and the quarter-wavelet approximation. The former provide an estimation of amplification based on resonance phenomena. Consequently, the modes of 1D vibration can be tracked along the basin at different frequencies. The latter gives explanation of the amplification induced by the velocity contrast between the bedrock and soft sediments only. Effects such as basin edge effects or 3D resonances might play a major role in the Luzern area, and they are not modelled by 1D site response. Further studies will focus on improving the knowledge of the variable surface layer, and on modelling wave propagation in 3D. Two permanent strong motion sensors are presently installed in Lucerne that will further help to improve the structural model. In dealing with strong motion events, non-linear behavior of the soils is expected which needs geotechnical measurement and techniques that will allow us to model non-linear phenomena.

Acknowledgments

The research was supported by the Swiss National Foundation within the project HAZARD 2010 (S.N.F. No. 200021-112284) and also by the project NERIES (Network of Research Infrastructures for European Seismology, task JRA4 - 'Geotechnical site characterization'). We would like to thank René Graf (Kanton Lucerne, Verkehr und Infrastruktur, Naturgefahren) and Beat Keller (Keller+Lorenz AG, Lucerne) who supported this study. We are also grateful to SBB (Schweizerische BundesBahnen), which made possible the measurement in the train station of Lucerne. A special thank you also to Gabriela Gassner-Stamm, Han Havenith, Irena Löw and Marcella Völgyi for their support in performing the ambient noise measurements.

Chapter 3

T-f-k analysis of surface waves using the continuous wavelet transform

To be submitted in Pure and Applied Geophysics as:
Poggi, V., Fäh, D. and Giardini, D. (2011),
T-f-k analysis of surface waves using the continuous wavelet transform

Abstract

A new approach to surface-wave dispersion analysis using active sources is proposed. The method is based on continuous recordings, and uses the continuous wavelet transform to analyze the phase velocity dispersion of surface waves. The proposed approach is particularly suitable when using seismological equipment (e.g. together with passive acquisition of ambient vibrations), since it does not require any hardware-based source triggering. This can be subsequently done with the proposed method. Estimation of the surface wave phase-delay is performed in the frequency domain by mean of a covariance matrix averaging procedure over successive wave-field excitations. Thus, no record-stacking is necessary in the time domain and a large number of consecutive shots can be used. This leads consequently to a certain simplification of the field procedures.

To decompose the seismic wave-field, the continuous wavelet transform is applied. This gives the possibility of accurately localize the phase information in time, and to isolate and extract the most significant contribution of surface-waves. To process wavelet transform, a new mother wavelet is presented and compared to the classical Morlet type. The proposed wavelet is obtained from a raised-cosine envelope function (Hanning type). To extract the dispersion information, then, a hybrid technique is applied to the narrow-band filtered seismic recordings. The technique combines the flexibility of the slant-stack method in identifying waves that propagate in space and time, with the resolution of f - k approaches. This is particularly beneficial for higher modes identification in case of high noise level. To demonstrate the effectiveness of the method we tested it on synthetics as well on real field data. For the real case we combine dispersion curves from ambient vibration and active measurements.

3.1 Introduction

Surface wave analysis can be done with various techniques, applicable at different scales, spanning from global tomography [e.g. Shapiro et al., 2005] to the geotechnical site characterization [e.g. Stokoe and Nazarian, 1985; Tokimatsu, 1997]. All of these may differ in the type of employed source (active or passive), frequency range (thus resolution depth), number of receivers and analyzed component of motion. However, they all basically rely on the comparison between synchronous recordings to extract the phase or group velocity dispersion characteristics of the surface waves. This information can be used

to invert for the velocity structure of the site [e.g. Xia et al., 1999]. If compared to other seismic methods, like reflection and refraction seismic, the large diffusion of these techniques can be addressed to their simplicity, reliability and low cost of implementation. In spite of the substantially low resolution on geometrical discontinuities (the layers interfaces), surface-wave inversion is capable of a robust estimation of the average seismic velocities, especially for shear waves [Wathelet et al., 2008]. This is of primary importance in geotechnical engineering and local seismic hazard assessment.

In the paper we present an alternative way of performing active seismic acquisition, based on the continuous recordings of seismological stations (Fig. 3.1). Such approach arise from the practical exigence of optimizing the use of the available instruments for passive acquisition, with that of investigating shallower velocity structures. As a matter of fact, in surface wave analysis, the resolution on depth is controlled by the frequency range of investigation and the seismic velocity structure of the site [Aki and Richards, 1980]. Ambient noise, in general, is suitable for the investigation at relatively low frequencies only, roughly $<10\sim 20\text{Hz}$, [Horike, 1985]. This is mostly because of the strong attenuation of the wave-field generated by too far and scarcely energetic sources (natural or anthropogenic). To improve the resolution on the shallower depths then, high-energy artificial sources have to be used [Park et al., 2005]. This gives the possibility of exciting surface wave higher modes, that are rarely identified with passive seismic [Poggi and Fäh, 2010].

Nowadays, several techniques are available to analyze the surface-wave dispersion from simultaneous recordings. Most of them belongs to the so called domain-transformation methods and consists in two main categories: the τ - p [e.g. McMechan and Yedlin, 1981; Xia et al., 2007] and the f - k transforms [e.g. Lacoss et al., 1969; Nolet and Panza, 1976], with their respective variants. All of these methods present some advantages and disadvantages, and thus it is difficult to generalize which could be the best performing at a specific site and for a specific task. For example, τ - p methods performs generally better than f - k for short-duration transient signals, but have conversely limited frequency resolution. On the other side, f - k is more sensitive to uncorrelated noise. This is crucial especially for the identification of surface-wave higher modes [Strobbia, 2003]. Therefore, we combine the features of the two approaches into an hybrid time-frequency-wavenumber method, based on the continuous wavelet transform.

In the f - k methods like the classical beamforming [Lacoss et al., 1969], the signal's covariance matrix is obtained, at specific frequencies, from the complex conjugate cross-products between Fourier transformed signals over the different



Figure 3.1: Example of linear array of seismological stations during a mixed active/passive acquisition survey. Each station is an independent high-resolution recording unit.

offset locations. Thus, if a single wave propagate with a certain phase velocity, the elements of the covariance matrix will provide the relative phase-delays information between all receiver pairs. If several waves propagates at the same time but with similar phase-velocities, however, such approach can hardly separate out the different phase contributions. We propose therefore a different way to estimate the covariance matrix. We make use of the time-frequency analysis using wavelet transform to account for travel-time delays induced by wave propagation over the different offsets. Basically, the covariance matrix is obtained from extracting and correlating only those values of the complex spectrogram that satisfy a specific velocity of propagation. The procedure is similar to a τ - p analysis, but applied here to the estimation of the instantaneous phases.

For a given frequency and velocity, then, the single elements of this covariance matrix can be phase re-corrected to a common (and relative) reference time, according to the relative travel-time delays. In case of multiple shots, moreover, successive covariance matrices can be stacked and averaged, to enhance the phase-delay estimation with respect to background uncorrelated noise. Finally, the f - k power spectrum can be computed, using either the simple beamforming technique [Lacoss et al., 1969] or any other high-resolution

method, based e.g. on data weighting [e.g. Burg, 1967; Capon, 1969] or signal eigen-decomposition [e.g. Schmidt, 1986].

In the proposed technique, the seismic recordings are band-pass filtered using a wavelet decomposition. The complex spectrogram is therefore computed for each trace separately. This gives the possibility to localize in time the instantaneous phase of all wave contributions, in the different analyzed frequency bands. In the wavelet transform, the trade-off between resolution in time and frequency is controlled by the type of mother wavelet employed. In the present study, alternatively to the classic Morlet wavelet, we propose a new complex mother wavelet type, based on a raised-cosine envelope function (or Hanning taper). With respect to the simple Morlet type [Farge, 1992], the proposed wavelet is advantageous because it allows an increased resolution in time, since it satisfies the admissibility conditions [Daubechies, 1990] for smaller values of the non-dimensional central frequency (see Sheng 1995 for more details about wavelet properties).

The proposed method has been tested on active seismic records, both synthetic and real, for which we provide example results.

3.2 Method

3.2.1 Multiple shot triggering of continuous records

Continuous recording comes from the exigence of optimizing the use of our acquisition equipment for passive seismic in combination with active experiments. The main practical disadvantage in using seismological stations stays in the difficulty in triggering the initial time (t_0) of the artificial source. In practice, however, in all approaches based on cross-correlations (in the time or the frequency domain) the knowledge of an absolute t_0 is not necessary, since only the relative phase-delay information between traces is analyzed. For each shot, then, a simple “relative reference” initial time can be used instead of an absolute one.

To estimate a relative reference time of a particular shots, we implemented an automatic triggering procedure based on energy distribution localization. We first define a reference trace $u(x_{Ref}, t)$ (e.g. offset 1) for which the amplitude envelope A is computed as modulus of the analytical representation of the input signal (Fig. 3.2). From this envelope function, all relative maxima are then picked and sorted according to their energy level:

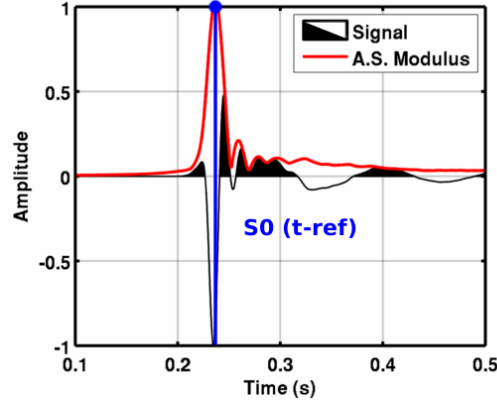


Figure 3.2: Automatic triggering of a single shot reference time (t_0 , in blue) using the modulus amplitude of the analytical signal (A.S., in red). The obtained t_0 is the relative reference for phase correction, however does not represent the true shot time.

$$A(t_0, t_1, \dots, t_n) = \left| u(x_{Ref}, t) + j \left[u(x_{Ref}, t) * \frac{1}{\pi t} \right] \right|_{Max} \quad (3.1)$$

Therefore, for n consecutive shots performed during the survey, the time instants (t_0, t_1, \dots, t_n) corresponding to the first n most energetic amplitudes are extracted (Fig. 3.3).

With respect to a simpler approach based on amplitude picking, the advantage in using the modulus of the analytical signal stays in the minimization of the bias introduced by the random phase interaction, that might produce peaks at different relative times of the consecutive shots.

3.2.2 Travel-time covariance matrix estimation

In all beamforming type techniques (classical or high-resolution), the signal covariance (or cross-correlation) matrix has to be computed over the different discrete frequencies to estimate of the f - k power spectrum. Thus, a Fourier analysis of the recordings is required. If we indicate with s the complex Fourier spectrum of the recorded signal u at the frequency f and offset x as:

$$s(f, x) = \int_{-\infty}^{\infty} u(x, \tau) e^{-2\pi i f \tau} d\tau \quad (3.2)$$

and the vector of spectra at different offset as:

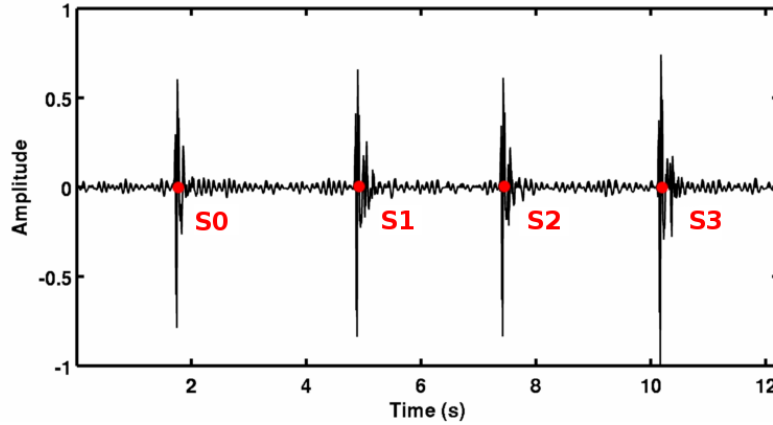


Figure 3.3: Detection of multiple shots (S_0 - S_3) on continuous recording of seismic data. The corresponding picked times will be used, then, as relative reference for the elaboration.

$$\mathbf{S}(f) = [s(f, x_1), \dots, s(f, x_n)]^T \quad (3.3)$$

then the covariance matrix can be simply estimated as:

$$\hat{\mathbf{R}}(f) = E \{ \mathbf{S}(f) \cdot \mathbf{S}(f)^h \} \quad (3.4)$$

where h stands for Hermitian conjugate. Usually, the whole record window is used for the computation of the Fourier spectra. In such way, however, the influence of body waves and other contributions (e.g. noise, air blast) can significantly affect the final result, introducing some bias on the phase estimate of surface waves. To avoid this problem, it is common procedure to manually select some appropriate windows (tapering in the time-offset domain) to exclude the direct and refracted arrivals and emphasize therefore the surface wave content. Such approach, however, is influenced by the subjectivity of the operator who defines the window, since no strict rules are (and can be) established for this procedure. In some cases, portions of the traces cut out by manual windowing can still contain usable surface wave information. Moreover, the length of the selected windows can be very different at different offsets, affecting the robustness of the covariance matrix elements estimate.

To overcome this problem, we perform a time-frequency analysis of the records, using the continuous wavelet transform (Fig. 3.4). Such approach has the advantage to make the phase information separable in time (as instan-

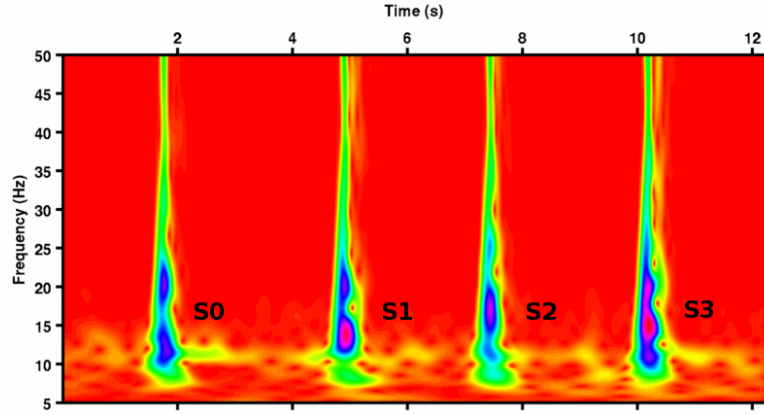


Figure 3.4: Wavelet spectrogram (absolute value) of the four shots recorded at the first receiver location. As it will be explained more in detail in section 3.3, the raised-cosine mother wavelet is used for this example.

taneous estimation) and thus for the different wave contributions. Therefore, once a propagating wave is identified, its instantaneous phase can be extracted at a specific frequency. Clearly, the quality of the result is controlled by the trade-off between the resolution in time and frequency of the wavelet transform. In general, the higher is the resolution in time, the lower is in frequency and vice versa (following the Heisenberg uncertainty principle).

The problem is therefore how to automatically isolate the propagation of a particular wave on the complex spectrogram obtained from the wavelet decomposition. For surface waves this cannot be simply done by travel-time picking, since the surface-wave arrival-time cannot be localized because of the dispersion. To solve this, we implemented a direct search approach, based on the idea of τ - p analysis (or the slant-stack), but applied here to wavelet filtered signals. If we define the wavelet-transform w of the signal u at a specific frequency f and offset x as:

$$w(f, x, t) = \int_{-\infty}^{\infty} u(x, \tau) w_m^h(f, t, \tau) d\tau \quad (3.5)$$

where w_m is the filter bank base to be used (or the mother wavelet, see section 3.3), then the offset-vector obtained by those complex values that satisfy a specific velocity of propagation v and source delay-time t at the different offsets can now be written as:

$$\mathbf{S}(f, t, v) = \left[w \left(f, x_1, t + \frac{(x_1 - x_{Ref})}{v} \right), \dots, w \left(f, x_n, t + \frac{(x_n - x_{Ref})}{v} \right) \right]^T. \quad (3.6)$$

Therefore, the covariance matrix is:

$$\hat{\mathbf{R}}(f, t, v) = E \{ \mathbf{S}(f, t, v) \cdot \mathbf{S}(f, t, v)^h \}. \quad (3.7)$$

In practice, $\hat{\mathbf{R}}(f, t, v)$ is computed as the Hermitian cross-products between those instants on the complex spectrograms that correspond to a specific wave (see examples in Fig. 3.5). With respect to the classic way of estimating the covariance matrix - using Fourier transform - the correlation depends now on three independent variables and thus is *travel-time dependent*. However, since the t and v parameter pairs are not known a-priori, the matrix has to be recomputed for any possible combination, within a given reasonable range of expectation. The delay-time search parameter t , in particular, is necessary because we might expect the surface waves not to develop immediately at the shot time, and higher modes not to be simultaneous with the fundamental.

As last step, then, each element of $\hat{\mathbf{R}}(f, t, v)$ can be phase-corrected back to a reference time common to all traces (e.g. t_{Ref} obtained by triggering), to compensate the effect of travel-time delay over the different offsets:

$$\hat{\mathbf{R}}_{i,j}^{\phi}(f, t, v) = \hat{\mathbf{R}}_{i,j}(f, t, v) e^{\left[-2\pi f \left(t_{Ref} + \frac{(x_j - x_i)}{v} \right) \right]} \quad (3.8)$$

So done, it is now possible to use such covariance matrix estimate to compute the f - k power spectrum with classic beamforming algorithms.

3.2.3 Covariance matrix stacking and phase-averaging

The classic acquisition protocol for active seismic includes the stack of consecutive recordings to improve the signal-to-noise ratio. This is particularly suitable for reflection/refraction seismic, where only the correct identification of the travel-times is of primary importance, but it might not be strictly necessary for surface wave analysis and in case of continuous recordings. Averaging the phase over different shots implies the assumption that each wave excitation will produce exactly the same phase spectrum at the source. This assumption, however, might not be perfectly fulfilled in reality when simple artificial sources

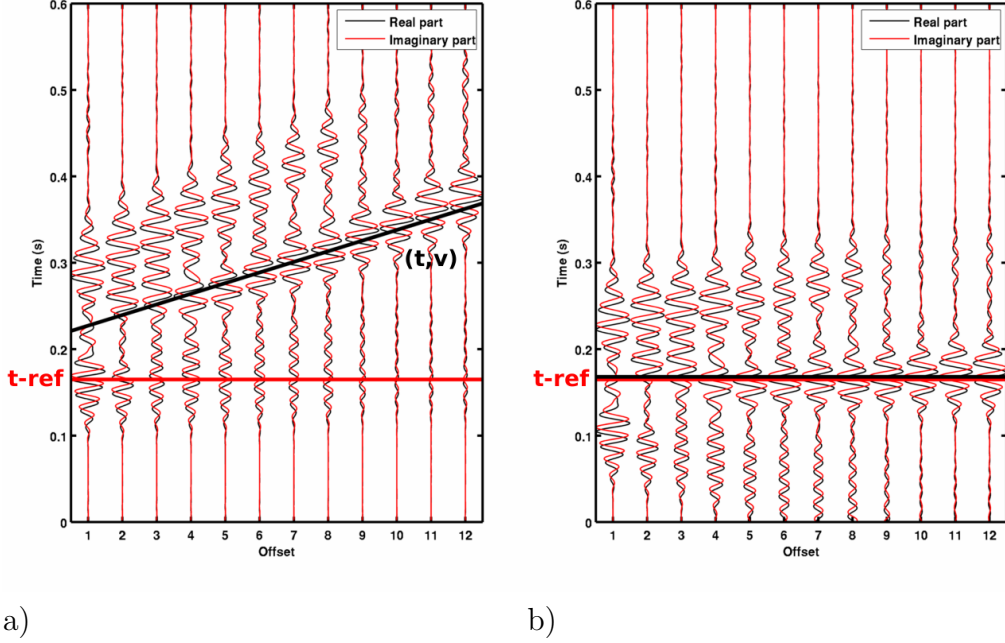


Figure 3.5: a) Wavelet transformed traces (real and imaginary part) of a 12 stations seismic record (here filtered at 30Hz). It is possible to follow the single components propagating with different source delay-time and phase velocity (t,v) . b) The triggered reference time (t_{Ref}) is used for travel-time correction of the covariance matrix elements, assuming a phase velocity.

are used, like mini-gun or the sledge hammer. For those kind of devices it is indeed difficult to ensure that they will always operate in a repeatable fashion. This is particularly evident at rather high frequency ranges, where we can observe phase cancellation.

To enhance the final resolution of the f - k estimate, instead of averaging the single phase estimates, we average the phase-differences between receiver pairs. This can be done by stacking the travel-time corrected covariance matrix over consecutive N shots:

$$\left[\hat{\mathbf{R}}^\phi(f, t, v) \right]_{TOT} = \sum_{m=1}^{N(\text{shots})} \frac{\left[\hat{\mathbf{R}}^\phi(f, t, v) \right]_m}{N}. \quad (3.9)$$

Such procedure minimizes the effect of uncorrelated noise, enhances the phase-delay estimation and stabilizes the covariance matrix in the use with high resolution f - k algorithms based on eigen-decomposition.

3.2.4 Note on amplitude normalization

Due to geometrical and intrinsic attenuation, the wave amplitude decrease with increasing distance to the source. If the maximum inter-distance between receivers is too large, an offset normalization procedure might be necessary to emphasize the information at far offset. We tested different approaches to equalize the signal's energy content at the different receiver locations.

As first attempt, we applied a simple geometrical decay correction approach, assuming that in first approximation surface waves attenuate with the distance r as $1/\sqrt{r}$. Such approach, however, doesn't take into account the influence of anelasticity and explains geometrical spreading on vertically heterogeneous media only as first approximation. A second possibility consists in normalizing the single traces with respect to their relative energy level. This can be done by dividing for the maximum amplitude or, more accurately, by normalizing to the whole energy content of a trace:

$$w(f, x, t) = \frac{w(f, x, t)}{[\int |w(f, x, t)|^2 dt]^{1/2}}. \quad (3.10)$$

In such a case the correction is independent from prior assumption but, when the energy content of body waves is too large (e.g. at close offset), it might lead conversely to an underestimation of surface wave contribution. Thus it is preferable to be used at intermediate to large offsets only.

Such procedures have been tested both on raw and wavelet filtered traces, for comparison. As expected, correcting for geometrical attenuation provides the comparable results in the two cases, as only a constant multiplicative factor is applied to a linear transformation. However, differences are relevant in case of amplitude/energy equalization, that provides better results when used on wavelet filtered traces. This is most probably related to the removal of uncorrelated noise by the filtering, that is thus not subsequently amplified by the correction as it would be on raw traces.

Finally, an interesting alternative consists in directly normalizing the signal covariance matrix using the simple approach proposed by Capon [1969]. In this case, the normalization is based on the relative amplitude of each pair of cross-correlated signals:

$$\hat{\mathbf{R}}_{i,j}^{\phi}(f, t, v) = \frac{\hat{\mathbf{R}}_{i,j}^{\phi}(f, t, v)}{[\hat{\mathbf{R}}_{i,i}^{\phi}(f, t, v)\hat{\mathbf{R}}_{j,j}^{\phi}(f, t, v)]^{1/2}} \quad (3.11)$$

for $i \neq j$, and:

$$\hat{\mathbf{R}}_{i,j}^{\phi}(f, t, v) = 1 \quad (3.12)$$

for $i = j$.

After testing, we found this last approach convenient in combination with energy normalization to enhance the detectability of higher modes. This procedure is therefore used in all following tests.

3.2.5 The f-v-t power spectrum and grid search

Applying the procedures described above, we obtained an estimation of the signal covariance matrix that depends, other than on frequency, on the analyzed phase-velocity and source time of surface-waves. The f - v - t power spectrum, then, can directly be computed using the classic tools for f - k analysis, e.g. like classic beamforming:

$$P(f, t, v) = \frac{\mathbf{e}(f, v)^h \hat{\mathbf{R}}^{\phi}(f, t, v) \mathbf{e}(f, v)}{N^2}, \quad (3.13)$$

high-resolution beamforming:

$$P(f, t, v) = \frac{1}{\mathbf{e}(f, v)^h \left[\hat{\mathbf{R}}^{\phi}(f, t, v) \right]^{-1} \mathbf{e}(f, v)}, \quad (3.14)$$

or MUSIC:

$$P(f, t, v) = \frac{1}{\mathbf{e}(f, v)^h \left[\hat{\mathbf{U}}(f, t, v) \hat{\mathbf{U}}(f, t, v)^h \right] \mathbf{e}(f, v)} \quad (3.15)$$

where $\hat{\mathbf{U}}(f, t, v)$ consists of the subset of eigenvectors of the covariance matrix $\hat{\mathbf{R}}^{\phi}(f, t, v)$ that span the noise subspace.

However, the results from all high-resolution methods strongly depends on specific site-related conditions, like the amount of uncorrelated noise and the local accuracy in the phase-estimation. These methods, moreover, do not always provide accurate results in case of multiple overlapping signals, that is the case for higher modes identification. Therefore, to better stress the possibilities and limitations of our methodology, in the following sections we will present the results from using classical beamforming algorithm only.

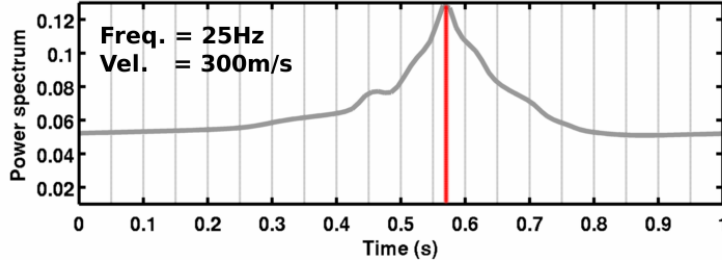


Figure 3.6: Power-spectrum search over surface-wave source time, fixed velocity and frequency. In this example, the maximum of correlation is reached after about 0.57 seconds after the triggered t_{Ref} of the shots. This corresponds to a second higher mode.

From the implementation point of view, identifying and extracting the surface dispersion curves is done by means of a power-spectrum local maxima search over a three-dimensional parameter space. For simplicity, we first perform a grid search over t , fixed v and f (Fig. 3.6). The procedure is then repeated for all combinations of v and f , respectively. Obviously, such processing is computationally more expensive than the classic approaches for surface wave analysis. However, the entire procedure can be conducted automatically and, even for a high number of shots, without the supervision of the user.

3.3 The raised-cosine mother wavelet

To compute the time-frequency spectrogram, the continuous wavelet transform is used. Since we are dealing with phase-delay estimation, a complex mother wavelet has to be consequently adopted. Between the possible choices, a very common mother wavelet in seismology is the Morlet [Goupillaud et al., 1984]. This can easily be obtained from the convolution between a harmonic complex signal of given frequency, with a Gaussian envelope, whose width controls the trade off between time and frequency resolution of the wavelet. Its non-dimensional time η representation is:

$$w_m(\eta) = \pi^{-1/4} e^{-\eta^2/2} e^{jC_0\eta} \quad (3.16)$$

and in normal time t :

$$w_m(t) = \pi^{-1/4} e^{-\frac{1}{2}\left(\frac{\omega_0 t}{C_0}\right)^2} e^{j\omega_0 t}. \quad (3.17)$$

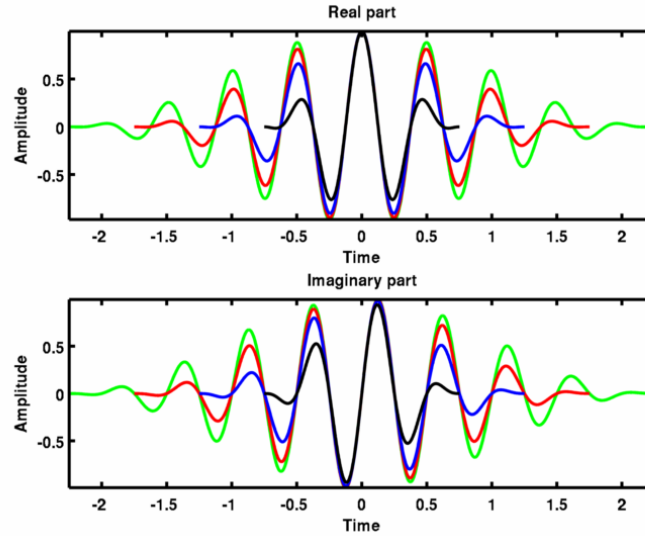


Figure 3.7: Real (on top) and imaginary (on bottom) part of the raised-cosine mother wavelet, computed for non-dimensional central frequency C_0 values of 1, 2, 3, 4 (black, blue, red and green respectively).

It is well known however, that the Morlet wavelet do not always satisfy the admissibility conditions [Farge, 1992] for any value of the Morlet coefficient C_0 (or the non-dimensional central frequency). For value of C_0 lower than 6, the wavelet spectrum start to diverge. Consequently, such wavelet presents a lower resolution bound in time, that makes difficult the analysis of extremely narrow impulsive transients. This is generally not an issue in most seismological application, but can be a limitation when separation of short transients close in time is required.

To partially overcome this problem, we propose an alternative although similar type of complex wavelet, based on a simple raised-cosine tapering window (or Hanning type) applied to a complex exponential function (Fig. 3.7). The wavelet can be expressed in the non-dimensional time η as:

$$w_{rc}(\eta) = \frac{1}{2} (1 + \cos(\eta)) e^{jC_0\eta} \quad (3.18)$$

for $-\pi \leq \eta \leq \pi$, and in normal time t as:

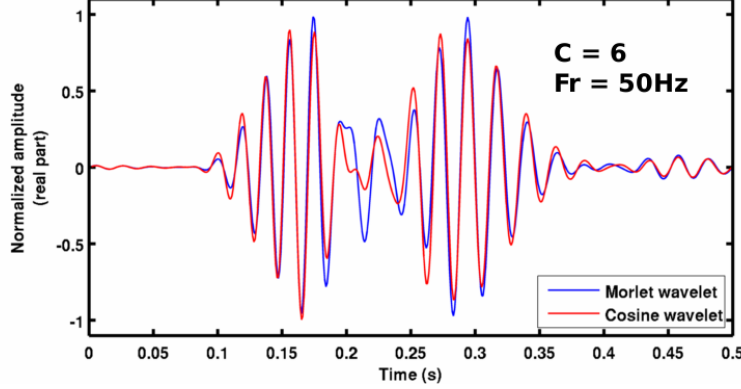


Figure 3.8: Comparison of wavelet-filtered trace (imaginary part) using the classic Morlet and the raised-cosine wavelets. A relatively low value of the non-dimensional central frequency C_0 is used.

$$w_{rc}(t) = \frac{1}{2} \left(1 + \cos \left(\frac{\omega_0 t}{C_0} \right) \right) e^{j\omega_0 t} \quad (3.19)$$

for $-\pi C_0/\omega_0 \leq t \leq \pi C_0/\omega_0$, where ω_0 is the dimensional central frequency.

With respect to the Morlet wavelet, the proposed one presents some differences. As first, its energy is entirely bounded in time ($-\pi \leq \eta \leq \pi$) and has admissibility condition satisfied for any value of C_0 being integer and higher than 1:

$$\int_{-\pi}^{\pi} w_{rc}(\eta) d\eta = 0 \quad (3.20)$$

for $C_0 \in (\mathbb{N} \geq 2)$. Therefore, it allows an increased time resolution, that is indeed not possible with the Morlet wavelet. For values of C_0 equal and higher than 6, nevertheless, the results from the two wavelets becomes progressively comparable (e.g. Fig. 3.8).

The Fourier spectrum of such wavelet can be easily obtained in the following analytical form as:

$$w_{rc}(\omega) = - \left[\frac{\omega_0^2}{(\omega_0 - \omega)^3 C_0^2 - \omega_0^2 (\omega_0 - \omega)} \right] \sin \left(\frac{(\omega_0 - \omega) C_0 \pi}{\omega_0} \right). \quad (3.21)$$

Compared to the Morlet wavelet, the spectrum is in this case sharper, for the

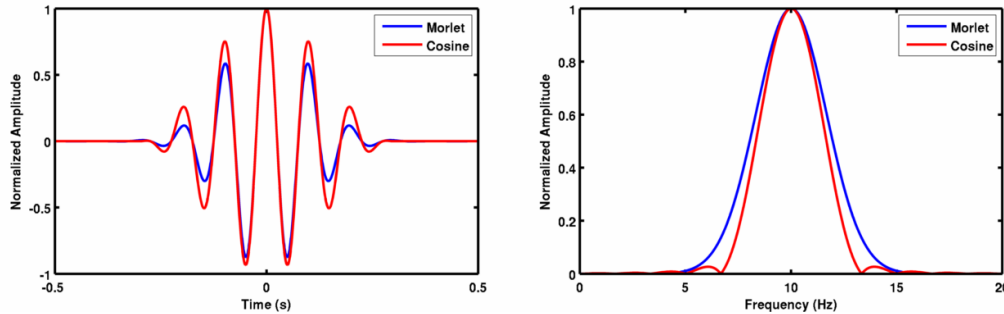


Figure 3.9: Comparison in time (on left, real part) and frequency (on right, absolute value) domains between the Morlet and the raised-cosine wavelets. In the example are used $C_0 = 10$ and $\omega_0 = 10Hz$.

same values of the central frequency C_0 (Fig. 3.9), even though it presents typical low energy side-lobes and zeros.

3.4 Results

To test the robustness of the proposed algorithm, both synthetic and real datasets were processed. In all cases, three components recordings were used, in order to analyze the different surface wave contributions.

3.4.1 The synthetic dataset

A set of synthetic seismograms were generated by Sabine Latzel for a previous active seismic study [Schuler, 2008]. For the modeling, an algorithm originally written by Friederich and Dalkolmo [1995] was used. The model, taken from literature [Dal Moro et al., 2006], consists of three horizontal layers with seismic velocities (V_s and V_p) progressively increasing with depth (Table 3.1). A point (delta) source located at the surface was employed, with frequency bandwidth of 1-60Hz. Each synthetic consists in the continuous recording of 4 consecutive shots, spaced about 2 seconds each. To emulate realistic field conditions, an amount of white (uncorrelated) noise was applied to the traces before processing. Synthetics seismograms were generated for 40 receivers locations with 1m spacing.

For comparison, we processed the recordings using both the classic Fourier-based method and the wavelet approach (Fig. 3.10 and 3.11) using beamforming. We avoided using MUSIC for the testing, since the results from such approach strongly depend on the noise characteristics, and do not always provide

	<i>Thickness</i> (m)	V_p (m/s)	V_s (m/s)	<i>Density</i> (kg/m ³)
<i>Layer1</i>	8	340	140	1700
<i>Layer2</i>	8	2770	1570	2050
<i>Layer3</i>	–	5200	3000	2400

Table 3.1: Parameters of the one-dimensional models employed to generate active seismic synthetics.

stable results for higher modes identification. In particular, the two methods always provide comparable results in the case of single shot and in absence of noise disturbances. However, when multiple consecutive shots are used and Gaussian noise applied, the wavelet method produces more stable results (Fig. 3.10-3.11, b) in comparison to the classic approach (Fig. 3.10-3.11, a). In more detail, the higher modes are emphasized, even at high velocities, and therefore better identifiable (Fig. 3.12). This can be explained by the more robust estimation of phase-delays obtained with the t - v - f grid search combined with the previously discussed procedures of covariance matrix stacking and normalization, in presence of strong uncorrelated noise.

3.4.2 Testing real data: Lucerne (Switzerland)

To test the method on a real case, a mixed active/passive seismic survey was performed in Lucerne (Switzerland). The target of our analysis is a well studied area, that has been extensively investigated with passive seismic techniques within a previous microzonation study [Poggi et al., 2011, in review]. However, the sole use of passive techniques did not provide sufficient resolution on shallow depths, that are significant to characterize the high frequency seismic response during an earthquake. Together with the analysis of boreholes logs, an uppermost low seismic velocity layer was identified. Such layer appears to be continuous along great part of the area, but with a variable thickness. Due to the velocity contrast to the deeper structure, this layer suits the conditions for generating a sufficient amount of surface waves during an active seismic experiment.

A test was performed combining a passive and an active seismic acquisition survey. For the experiment, 12 seismological stations were used, equipped with triaxial velocity sensors (5s eigen frequency). For the active seismic test, a linear configuration was implemented, with 4 meter spacing between receivers. According to the available number of stations, this configuration limited considerably the resolution on dispersion curves at high frequencies (roughly 40 Hz

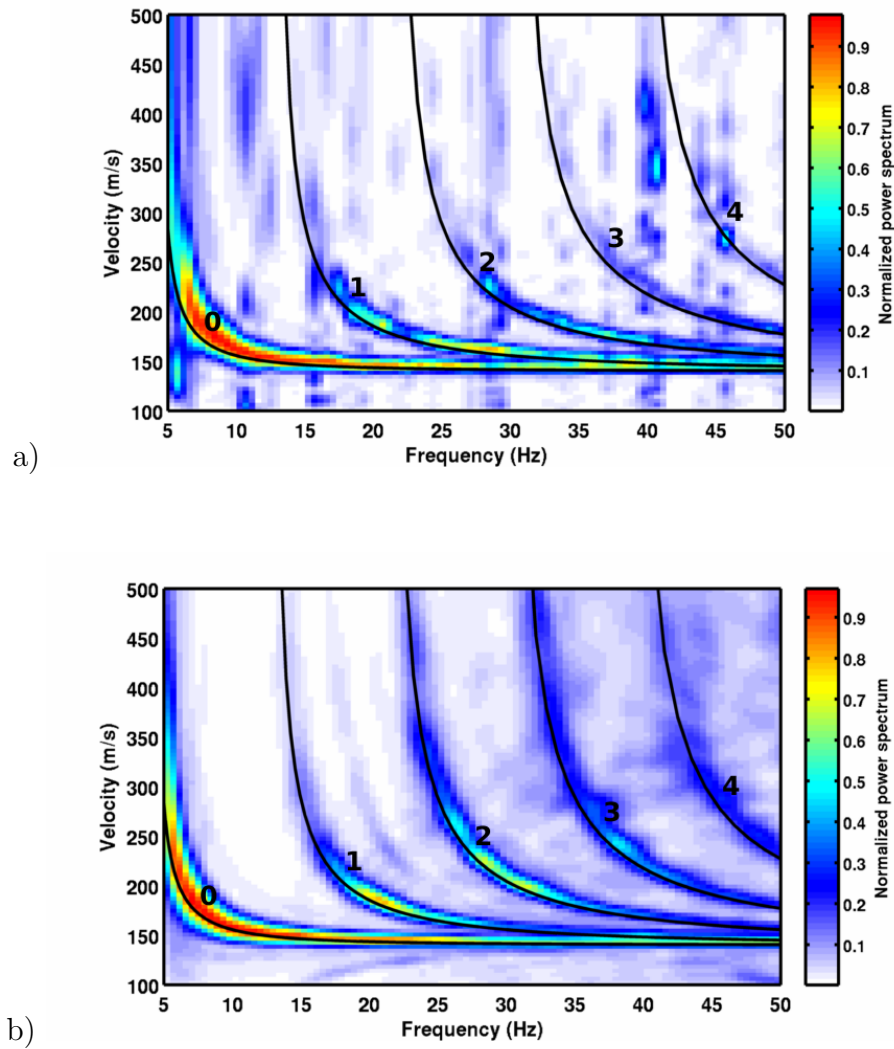


Figure 3.10: Frequency-velocity power spectrum of the synthetic dataset using the classic Fourier-based beamforming (a) and the wavelet method (b). In this example, the transversal (SH) component is shown, using 40 receivers with 2.5m inter-distance. Four shots were performed. Here, other than the fundamental mode of Love waves, additional four higher modes can be clearly identifiable (analytical solution in black solid line).

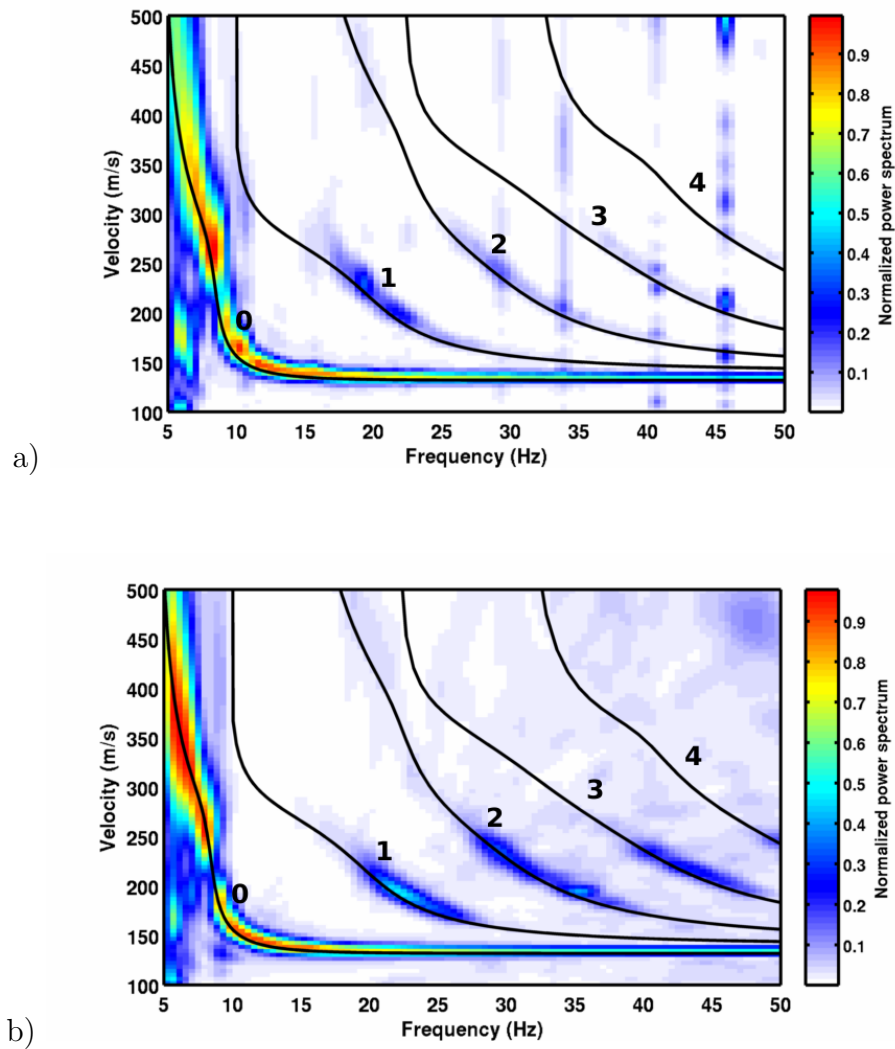


Figure 3.11: Frequency-velocity power spectrum of the synthetic dataset using the classic Fourier-based beamforming (a) and the wavelet method (b). In this example, the vertical (PSV) component is shown, using 40 receivers with 2.5m inter-distance. Four shots were performed. In comparison to the transversal component in Fig. 3.10, the higher modes are here less energetic with respect to the fundamental, and consequently more difficult to track.

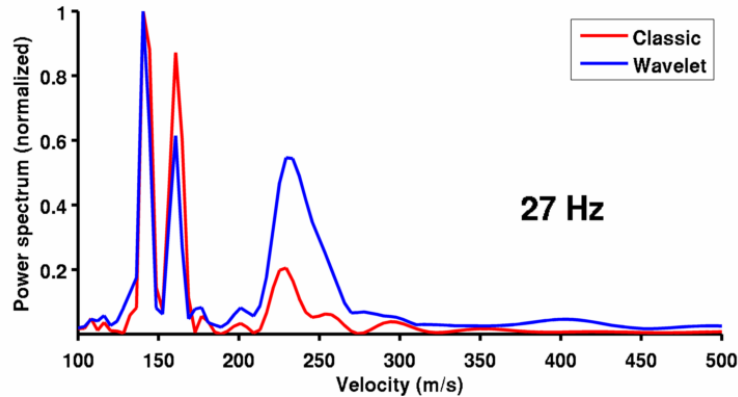


Figure 3.12: Comparison of the power-spectrum computed with different approaches. It is possible to notice how the proposed wavelet-based method emphasizes the energy content of the higher modes (here of the transversal component), making them more visible (e.g. the second higher mode at 230m/s).

for the expected phase-velocity range), but gives on the opposite the possibility to extend the analysis to a frequencies range close to that of the passive acquisition. We tested different shot-offset locations (2, 5, 10, 20m). Due to the length of the deployment, however, the shorter offset provided the better results. Within each shot location, 5 consecutive wave-field excitations were performed, with about 2 seconds delay between. As artificial source, we used a sledging hammer impacting on a special triangular support that give the possibility of reproducing a 45° point source. When aligned to the array deployment, such device allows the generation of Rayleigh waves, including the radial component.

For the passive seismic acquisition, the stations were reorganized in a crossed configuration (see Fig. 3.13) along two main directions. Such configuration is usual in urban environments, because it adapts to available space along cross-roads. The total diameter of the array deployment was about 140m, that results, with the high-resolution f - k method, in a low resolution limit of about 3Hz (see Poggi and Fäh 2010 for more details about the resolution in the f - k processing).

The processing of the vertical and radial component provides comparable results. For both cases, the power spectrum has been computed in a frequency range between 5 and 40Hz using the wavelet approach to estimate the covariance matrix, together with classical beamforming (Fig. 3.14). This frequency range is sufficient for the identification of five Rayleigh waves modes, that can correctly be addressed at least up the 4^{th} overtone. Surprisingly the fundamen-

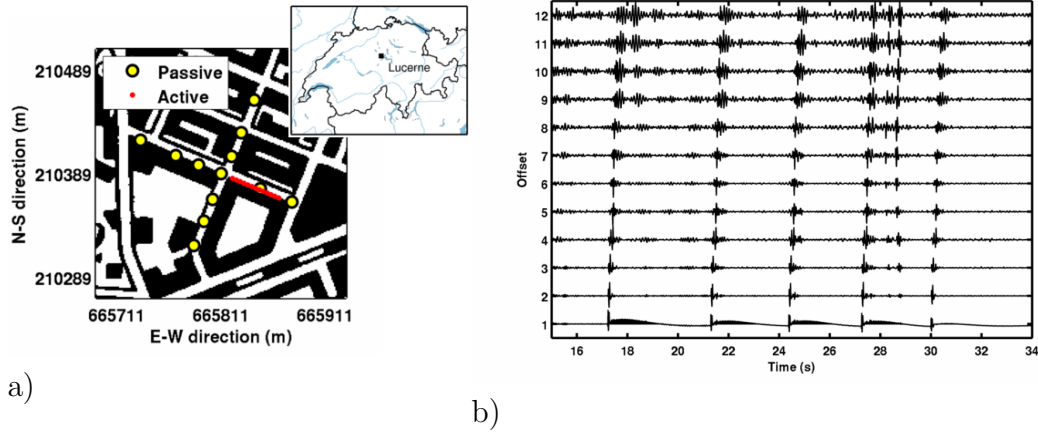


Figure 3.13: a) Array geometry for the passive and active (linear) seismic acquisition. b) Example of continuous recording from the seismicological stations during the active experiments. Five consecutive shots were performed, with about 2 seconds delay between, using a sledge hammer.

tal mode, that is generally the most energetic over a broad range of frequencies, lacks of energy above 10Hz and cannot be followed anymore. Conversely, the energy progressively distributes to the higher modes, that can easily be tracked up to 40Hz .

The result of the active seismic experiment has been compared with that from passive acquisition (Fig. 3.15). The processing of ambient vibration was made using the three-component high-resolution beamforming algorithm, as explained in Poggi and Fäh [2010]. Unfortunately, the processing of the two horizontal components (radial and transversal) did not provide usable results, probably caused by the difficult measurement environment. On the vertical component, however, it was possible to clearly identify the fundamental mode of Rayleigh waves in a frequency range roughly between 3.5 and 6.5Hz . The curve is consistent with that portion of the fundamental mode identified by active seismic. The phase velocity jump at 7Hz can be addressed to the aforementioned presence of the low-velocity layer.

3.5 Discussion and conclusions

In this paper we presented a new approach to surface wave analysis of active seismic experiments, based on the continuous recordings of seismicological stations. The method is therefore suitable in combination with passive seismic

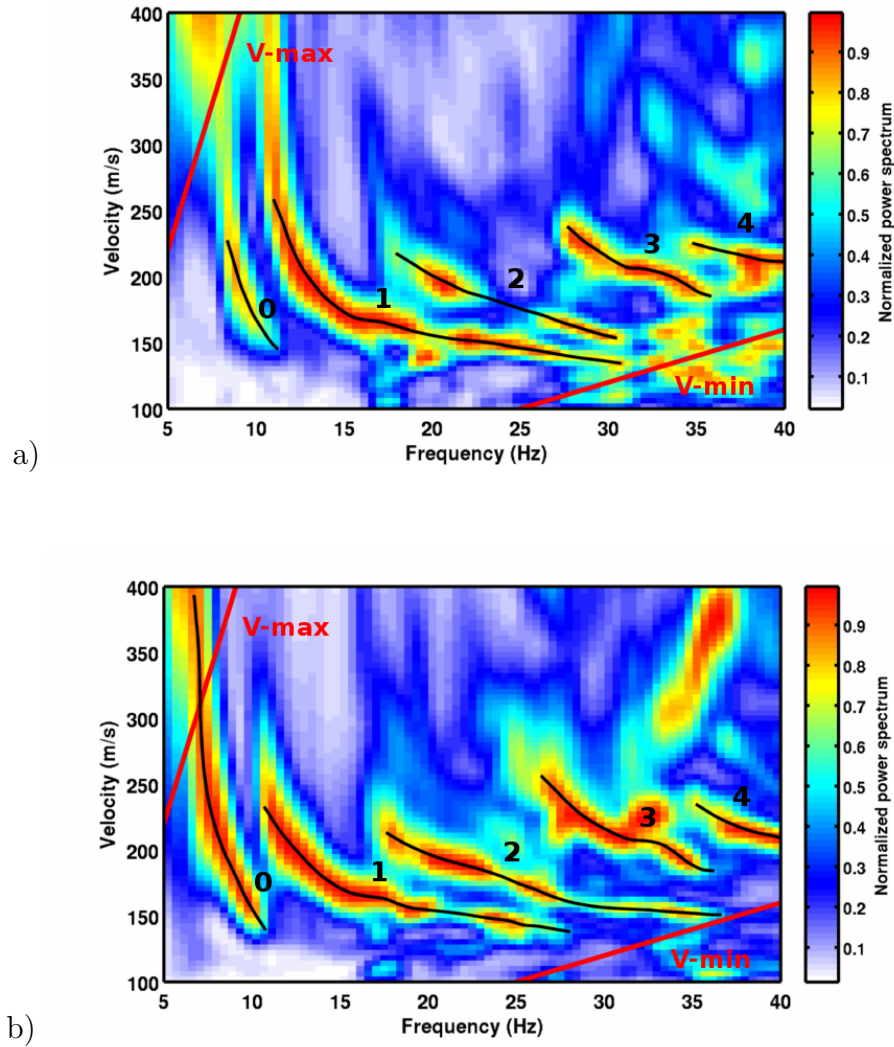


Figure 3.14: Frequency-velocity plot of the seismic survey performed in Lucerne (Switzerland). The elaborations for the vertical (a) and the radial (b) components are presented. The array consisted in a linear configuration of 12 seismological stations with 4m inter-distance. Five shots were recorded continuously, in this case with an shot-offset of 2m. The identified Rayleigh modes are consistent between the two processed components, but they clearly show a different energy content. V-min and V-max indicate, respectively, the lower and the higher resolution limits for this array geometry, using the classical beamforming.

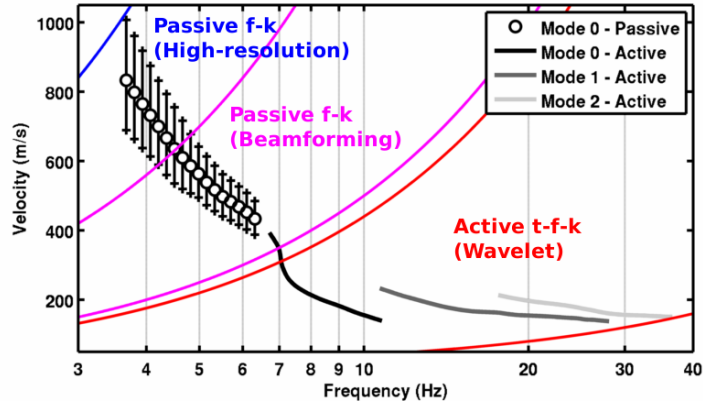


Figure 3.15: Comparison between Rayleigh wave dispersion curves obtained with active and passive seismic techniques. Resolution bounds of the different methods are presented. The velocity jump in the fundamental mode is induced by the presence of a large seismic impedance contrast at about $10m$.

acquisition. We use the continuous wavelet transform to extend the capability of beamforming techniques in detecting short transients that propagate in space with specific phase velocities. In practice, the proposed approach relies on the estimation of surface-wave travel-times to enhance the estimation of the signal covariance matrix. Moreover, stacking the covariance matrix over consecutive wave-filed excitation improves the resolution on surface wave dispersion imaging in noisy environments. The method is therefore particularly advantageous for higher modes detection, that are generally more affected by the disturbance of uncorrelated noise.

To compute the continuous wavelet transform we propose the use of a simple alternative mother wavelet. Such wavelet is similar to the Morlet wavelet and produces comparable results for same values of the non-dimensional frequency. However, with respect to the classical Morlet base function, the proposed is stable and satisfy the admissibility conditions also for value of C_0 small than 6, condition that ensure the achievement of an higher theoretical temporal resolution.

We tested the technique on synthetics records, as well as on a real case in the city of Lucerne. In both cases, multiple modes of the surface waves were detected. For the Lucerne experiment, moreover, the results are consistent with an estimation of the Rayleigh wave fundamental mode dispersion curve obtained from a passive acquisition survey performed on the same location. Therefore, this example shows the advantage of combining active seismic with

ambient noise processing to compensate for the reciprocal limitations of the two methods.

As main disadvantage, however, the presented approach is computationally more expensive if compared to previous $f-k$ methods, since it requires the re-computation of the covariance matrix for any permutation of the analyzed frequencies, phase velocities and source delay-times. Furthermore, such procedure has to be repeated for all recorded shots before stacking. Nevertheless all the search parameters are here independent, and thus the algorithm is easily parallelizable and scalable. It suits therefore for distributed computing on multi-core/multi-processor machines.

To decompose the wave-field, a time-frequency-wavenumber analysis based on the wavelet-transform has been applied to the active seismic records. With few modifications, we are confident that the presented method might also be successfully extended to ambient noise processing, to enhance the capability of separating out the different wave contributions (e.g. body and surface waves). As future development, moreover, we plan to extract and analyze, other than dispersion, the surface wave amplitude information from $t-f-k$ power spectrum estimates. On three-component recordings, for example, this might allow the estimation of the Rayleigh wave ellipticity function in active seismic experiments.

Chapter 4

Derivation of a Reference Shear-Wave Velocity Model from Empirical Site Amplification

Published in Bulletin of the Seismological Society of America as:
Poggi, V., Edwards, B. and Fäh, D. (2010),
Derivation of a Reference Shear-Wave Velocity Model from Empirical Site
Amplification, BSSA, 101-1, DOI number 10.1785/0120100060

Abstract

The definition of a reference bedrock condition representative of a region of interest is of great significance in seismic hazard assessment. It is highly beneficial when ground-motion prediction equations are referenced to a specific site condition, particularly in the case of site-specific seismic hazard analyses. When known, the effect of any given site with respect to the reference can then be applied to the predicted ground-motion. However, the choice of a reference velocity profile is not straightforward, mainly due to the high variability of the velocity structure in the shallower layers.

A new method to define the regional reference rock profile is proposed. The method relates quarter-wavelength average velocity at a site to frequency-dependent amplification. A reference bedrock velocity profile can then be directly defined in relation to expected amplification characteristics over a number of sites. We compare 27 quarter-wavelength velocity profiles from seismic station locations in Switzerland with empirical amplification functions derived from spectral modelling. From this comparison, a set of frequency-dependent calibration relationships is established. Assuming that the reference profile is defined by a lack of any relative amplification, the quarter-wavelength velocity profile that corresponds to unitary spectral amplification can be extracted. The reference velocity profile can then be obtained through an inversion procedure and defines the reference for the ground motion prediction equation (GMPE).

The proposed reference velocity profile is compared with previous reference velocity profiles. A good agreement is found between the different methods. Additionally, an estimation of the transfer function for the Swiss reference rock condition is provided. This can be used to correct recorded or estimated spectral amplitudes for the local response of the reference site. Finally, it is shown that the coefficients from the aforementioned correlations can be used to estimate a generic amplification function at any site with known quarter-wavelength velocity profile.

4.1 Introduction

It is well known that local site conditions can strongly influence the amplitude and duration of ground motion during an earthquake [e.g. Bard et al., 1988; Aki, 1993]. In particular, soft sediments with low seismic velocities with respect to the underlying bedrock can lead to large amplification of ground-motion at the surface [e.g. Bonilla et al., 1997; Pratt et al., 2003]. In site-specific proba-

bilistic seismic hazard assessment (PSHA), predicted ground motion must be referenced to a specific site condition such it can be subsequently corrected to the site of interest [Kawase, 2006]. The use of an incorrect reference condition for a ground-motion prediction equation (GMPE) may lead to an over- or under-estimation of the final computed seismic hazard [Steidl et al., 1996].

The correction for, or application of, site amplification is usually performed through a deconvolution or convolution of earthquake recordings with a soil response function. This can be done in either the time or frequency domain. The latter is the most common approach. Site amplification can be computed analytically [e.g. Abbiss, 1989], if sufficient knowledge of the velocity structure is available, or measured, for example by using site-to-reference spectral ratios [e.g Borchardt, 1970; Borchardt and Gibbs, 1976]. Correcting for the site amplification, however, always relies on the definition of a reference velocity profile, for which amplification phenomena are well known. The choice of a common reference is not always straightforward. Over small areas, the average characteristics of the rock basement can be used, and the reference can be defined based on direct geological or geophysical knowledge [e.g Romero and Rix, 2001]. Over large areas, however, the selection might be more problematic. In such a case, due the large variability of ground conditions, more general criteria of selection are necessary [Yu and Haines, 2003].

Reference rock conditions have previously been defined using simplified site geology classes or by directly estimating average velocities for the upper few tens of meters (e.g. NEHRP (National Earthquake Hazards Reduction Program, BSSC, 2001), EC8 (EuroCode 8, CEN, 2004)). The main disadvantage of using such approaches is the lack of a clear physical justification as to how the reference conditions are selected. In some cases, the reference is extrapolated beyond the depths directly measured using regional models [Douglas et al., 2009], for example, those computed using travel-time seismic tomography. This is partially correct, because tomographic models are sufficiently accurate at depth (i.e., of the order kilometers), but the interpolation between the upper most velocity (e.g., V_{s30}) and the velocity at depth is rather arbitrary. Local amplification, however, strongly depends on the velocity contrasts within the shallower layers. Several attempts have been made to improve the accuracy of the reference profiles at shallow depths, for example through the use of simplified gradient models [Boore and Joyner, 1997]. However, the choice of the correct parametrization to constrain these models still remains an open issue.

An alternative method to retrieve the reference velocity profile for hazard computation is proposed. Our approach focuses on the definition of a reliable

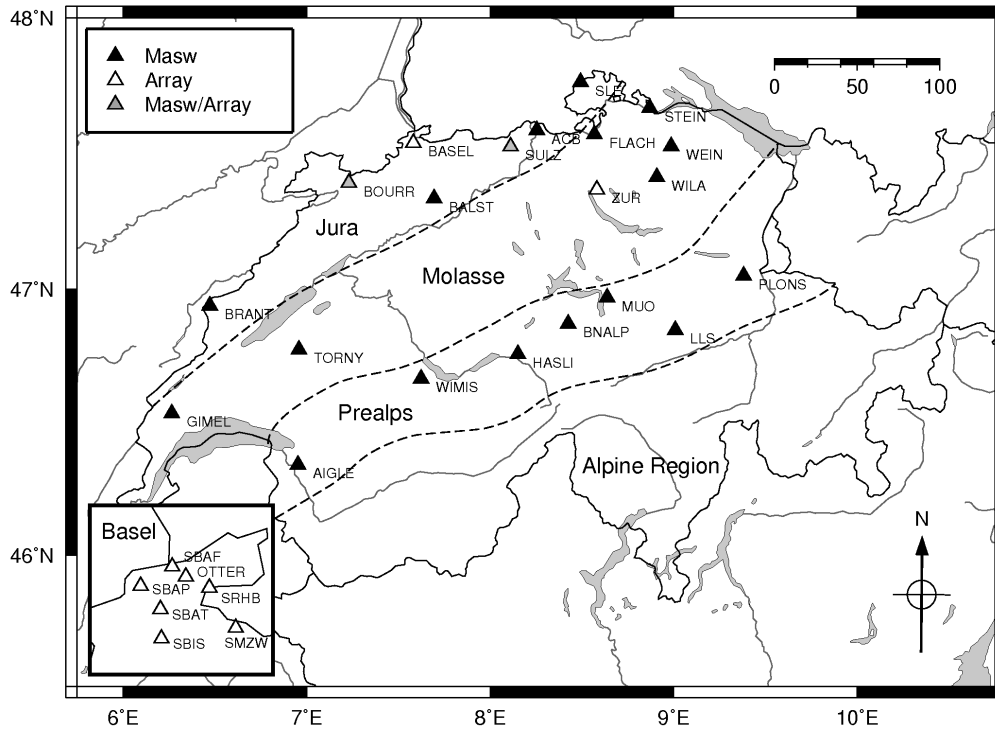


Figure 4.1: Location of the 27 seismic stations investigated during the PEGASOS Refinement Project. Of these stations, 17 were characterized using an active MASW technique, 8 using array analysis of ambient noise recordings and stations BOURR and SULZ with both the techniques. The stations shown are part of the Swiss Digital Seismic Network (SDSNet) and the Swiss Strong Motion Network (SSMNet). The approximate limits between main geological domains are shown.

way to constrain the first few hundred meters of the reference model. The method is based on the comparison of average velocities at specific seismic station locations with the corresponding amplification obtained from spectral modelling [e.g. Edwards et al., 2008; Drouet et al., 2008]. To relate the frequency-dependent amplification functions to the velocity information, the quarter-wavelength approximation [Joyner et al., 1981] is used. The advantage of such a procedure is the possibility of relating the depth over which the average velocity will be computed to a specific wavelength. As such, each average velocity estimates (versus depth) will be uniquely associated to a specific amplification factor at a defined frequency.

From the ensemble of measurement locations (Fig. 4.1), amplification versus average velocity relationships were computed for a set of discrete frequen-

cies between 1 and 15 Hz. From these relations, the quarter-wavelength average velocities corresponding to unitary amplification were extracted and collected. In this way, a quarter-wavelength representation of the reference velocity profile is established. However, for site characterization, a representation of the shear wave velocity profile versus depth is required. This is subsequently obtained through an inversion procedure. As a last step, a reference SH-wave amplification function was computed from the retrieved velocity profile to correct to the source condition. This transfer function can then be used as part of a stochastic model [e.g. Boore, 2003; Atkinson and Boore, 2006], which can simulate ground motion at the reference profile given a defined source and the attenuation characteristics of the propagation medium.

As an additional outcome, it is shown how the generic amplification function at a site with known quarter-wavelength average velocity can be estimated using the coefficients from the frequency-dependent correlations. The comparison between the reconstructed amplification and theoretical one-dimensional amplification models at test sites are consistent with observed amplification.

4.2 Selection of V_s velocity profiles for specific station locations

Twenty seismic stations of the Swiss Digital Seismic Network (SDSNet, Baer et al. 2007) and the Swiss Strong Motion Network (SSMNet) have been investigated within the PEGASOS Refinement Project - PRP [Fäh et al., 2009a]. The PRP is a seismic hazard assessment project coordinated by swissnuclear [Renault et al., 2010]. The locations of the investigated sites were defined in order to sample the most typical rock site conditions of the Swiss Alpine Foreland (Fig. 4.1). Seven additional stations were investigated during a previous microzonation study [Havenith et al., 2007]. In particular, of the total 27 investigated sites, 7 were selected in the Molasse Basin (GIMEL, TORNY, ZUR, WILA, WEIN, FLACH and STEIN), 7 were spread along the northern flank of the Alpine chain (AIGLE, WIMIS, HASLI, BNALP, MUO, LLS and PLONS), and 13 in the Jura region. Of these last, 7 stations (OTTER, SBAF, SBAP, SBAT, SBIS, SMZW and SRHB) are located inside the city of Basel, while the remaining 6 are distributed along the Jura chain (BRANT, BOURR, BALST, SULZ, ACB and SLE). For all these sites a large number of recordings exist, which are used to derive the empirical site amplification terms.

The main target of the PRP investigations was the characterization of the first 50 to 100 meters of the ground beneath each selected station. However,

not all the stations were equally accessible for surveying. In some cases (e.g., sensors located in tunnels or on steep topography) the measurement point did not match the sensor location. In such situations some corrections were therefore necessary. For example, the removal of the upper few meters of soft sediments from the measured profiles, in order to account for a buried sensor at the station [Fäh et al., 2009a].

In order to obtain the shear-wave velocity profiles, non-intrusive active and passive seismic techniques, such as multichannel analysis of surface waves (MASW) and high-resolution f - k analysis (HRFK) were applied. The MASW method [Park et al., 1999] is based on the analysis of the dispersion characteristics of surface waves (specifically Rayleigh waves), which are artificially generated by an active source located at the surface. The main advantage in using such a technique is the possibility of obtaining reliable estimations of the local velocity structure in a fast and cost-effective way. Consequently, large areas can be covered by a single survey. For each location where MASW was applied, several velocity profiles were provided, along sections of about 50m in length. In order to facilitate the interpretation, P- and S-wave seismic investigations were also carried out along the same profile (GeoExpert AG, 2009, technical report). From selected portions of these sections, mean 1D velocity profiles were then calculated (Fig. 4.2). This approach gave us the possibility of accounting for the local variability of the soil conditions and produce statistics on the final results. The main limitation of the MASW technique, however, is its low resolution at large depths. The resolution is controlled by the frequency band and the energy of the active source employed (in this case a sledgehammer).

The HRFK is an array technique for surface wave analysis, originally proposed by [Capon, 1969] and subsequently optimized by [Fäh et al., 2008] and [Poggi and Fäh, 2010] to analyse the full-ground motion (both Love and Rayleigh waves) from one- or three-component recordings of ambient noise. Unlike MASW, the use of passive-natural micro-vibration allows the investigation of greater depths [Yamanaka et al., 1994], but conversely yields limited resolution in the few upper meters. This limitation is mainly due to the few number of receivers usually employed during a survey, but also to the moderate energy content of the ambient vibration wave-field at high frequencies. This kind of survey produces a single one-dimensional velocity profile as output, which is representative of the average conditions over the whole area covered by the array. It is possible to define uncertainties on the measured velocity profile if the uncertainties of the surface wave dispersion information are propagated to the inverted velocity profile.

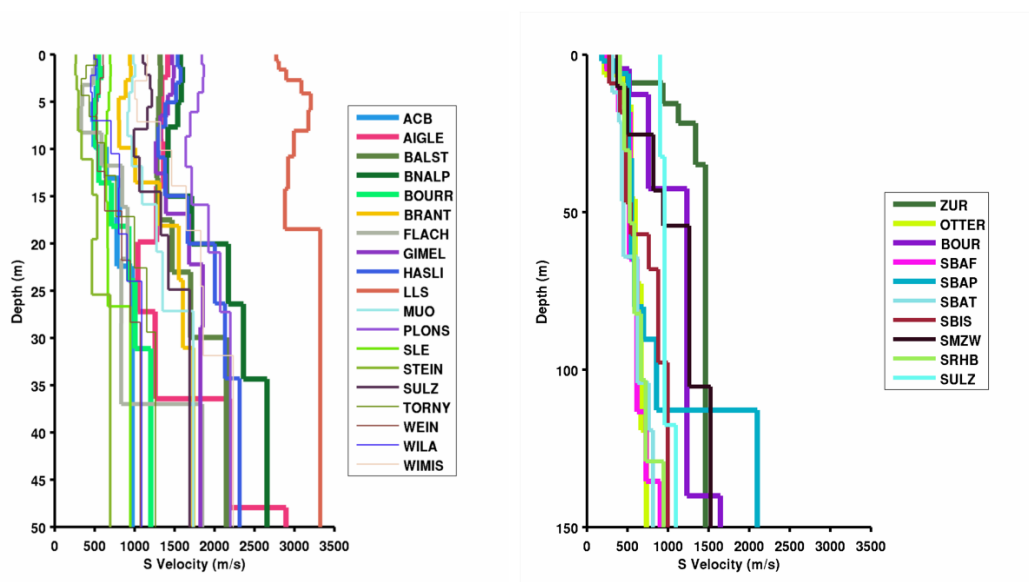


Figure 4.2: Velocity profiles from the 27 selected seismic station locations in Switzerland. Each velocity profile has been obtained from the inversion of surface wave dispersion (from active MASW, on the left, and passive array f - k analysis, on the right), and extrapolated beyond the resolution of the measurements.

Of the twenty-seven selected station locations, 10 were investigated using HRFK analysis (all Basel stations, plus ZUR, SULZ and BOURR), while 19 were investigated using MASW. Only stations BOURR and SULZ were surveyed using both techniques in order to verify the consistency of the results.

4.3 The quarter-wavelength velocity approximation

The quarter-wavelength approximation was initially proposed by Joyner et al. [1981], and subsequently optimized by Boore [2003] to compute amplification factors for generic rock profiles. The method is based on the estimation of the average seismic parameters (velocity and density) up to a depth that corresponds to one quarter of the wavelength of interest. For a specific frequency, amplification factors can then be computed as square root of the impedance ratio between average depth and reference.

The physical justification of using $1/4$ of the wavelength of interest as the averaging depth is that, in the simplified one-dimensional case (with one layer

over a homogeneous half space), a maximum in SH-wave amplification is observed at a defined frequency - the fundamental frequency of resonance f_0^{SH} - that corresponds to:

$$f_0^{SH} = \frac{V_{s_{Layer}}}{4 \cdot z_{Layer}} \quad (4.1)$$

(Roesset 1970), where $V_{s_{Layer}}$ and z_{Layer} are the shear-wave velocity and thickness of the layer respectively. Conversely, given any frequency, the largest amplification will occur at a specific layer depth, corresponding to 1/4 of the wavelength of resonance λ_0^{SH} :

$$z_{Layer} = \frac{V_{s_{Layer}}}{4 \cdot f_0^{SH}} = \frac{\lambda_0^{SH}}{4}. \quad (4.2)$$

Following this, the quarter-wavelength method assumes that, at any given frequency f , a vertically heterogeneous soil profile can be seismically characterized by its average velocity computed down to a depth $z(f)$ corresponding to 1/4 of the wavelength of interest. The quarter-wavelength velocity (V_s^{QWL}), can then be obtained for a specific frequency by travel-time averaging over the input profile, through the minimization of:

$$\underset{z(f)}{\operatorname{argmin}} \left\| z(f) - \frac{V_s^{QWL}(z(f))}{4f} \right\| \quad (4.3)$$

given that:

$$V_s^{QWL}(z(f)) = z(f) \left[\int_0^{z(f)} \frac{1}{V_s(z(f))} dz(f) \right]^{-1}. \quad (4.4)$$

This is achieved through a direct search approach over z in order to recursively converge to the solution of the minimization problem. Upon obtaining $z(f)$, the average quarter-wavelength density $\rho^{QWL}(z(f))$ can also be computed:

$$\rho^{QWL}(z(f)) = \frac{1}{z(f)} \left[\int_0^{z(f)} \rho(z(f)) dz(f) \right]. \quad (4.5)$$

To compute the final amplification, however, the quarter-wavelength method does not rely on the computation of the SH-wave transfer function. To avoid the inclusion of the characteristic resonance peaks (from the interference of up-

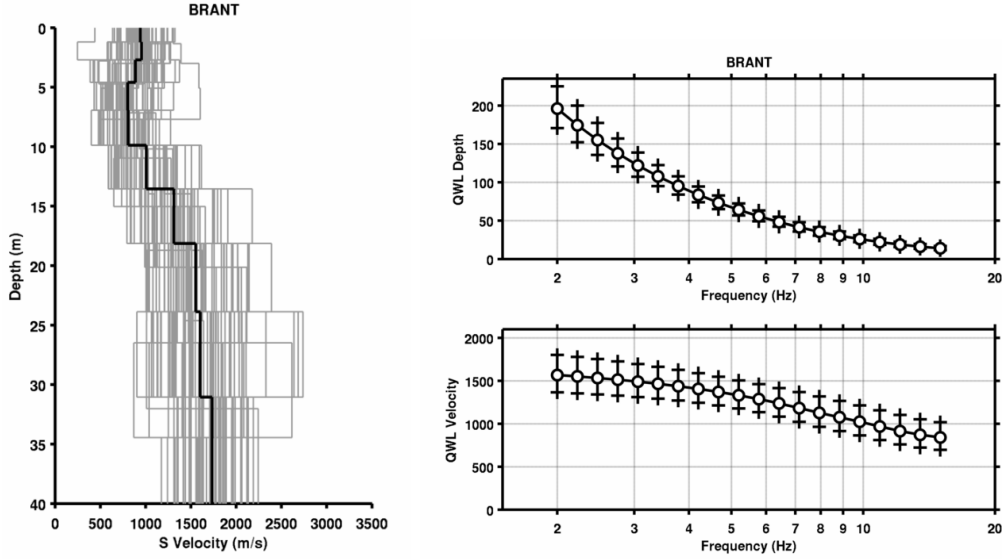


Figure 4.3: Example of measured V_s velocity profiles at the station BRANT (on the left) and its quarter-wavelength representation (on the right). Statistics are computed over the ensemble of all inverted velocity profiles from surface wave analysis.

and down-going reflected waves), the amplification is calculated as the square root of the ratio between the seismic impedance from the quarter-wavelength approximation and that of the source reference (generally the bedrock in the case of sedimentary basins):

$$A(z(f)) = \sqrt{\frac{\rho^C V_s^C}{\rho^{QWL}(z(f)) V_s^{QWL}(z(f))}}. \quad (4.6)$$

This approach always results in a smoothed amplification function. The quarter-wavelength method might therefore be advantageous, since in most cases these resonance amplification maxima result only as consequence of the discretization of the velocity profile for modelling. Following this procedure, then, quarter-wavelength curves were calculated from the ensemble of all available velocity profiles at each station location. For each dataset, finally, the mean value and standard deviation at discrete frequencies of 1 to 15 Hz were computed (Fig. 4.3).

4.4 Obtaining site specific amplification

The problem of separating source, path and site effects in terms of physical phenomena is a non-trivial and non-linear problem [e.g. Scherbaum, 1990]. Whilst the problem can be simplified in a way similar to that commonly used in engineering applications [e.g. Akkar and Bommer, 2007], such that the problem is linear, it is our opinion that the interpretation of such a model is more difficult to justify in a physical sense.

The Brune [1970, 1971] source model has been frequently shown to be a powerful way of modelling the far-field spectra of small earthquakes [Anderson and Hough, 1984; Boore, 1983, 2003; Hanks and McGuire, 1981]. In fact, Randal [1973] found that the Brune far-field model can be used to describe observed far-field earthquake spectra even in the case where the exact method of dislocation is unknown. The Brune [1970, 1971] source model is therefore commonly used in the deconvolution of source, site and path effects for small to moderate earthquakes and the simulation of ground-motion in regions of low to moderate seismicity [e.g. Atkinson and Boore, 2006].

An initial fit of the Brune [1970, 1971] source to each event, allowing for path variable attenuation and source specific stress-drop, is performed following a modification of the spectral deconvolution procedure presented in Edwards et al. [2008] and Edwards and Rietbrock [2009]. We adopt this model such that site-specific amplification functions can be obtained through a combination of residual analysis and direct inversion of numerous earthquake recordings. As a consequence of the model formulation, the amplification terms derived from this spectral fitting method are referenced to an unknown condition that represents the reference rock profile. Previous work by Drouet et al. [2008] showed that amplification functions derived following the spectral deconvolution approach were consistent with site-to-reference spectral ratios. Furthermore, we later show that the amplification functions derived using this approach are consistent with theoretical SH-amplification functions derived from measured Vs profiles.

It is assumed that the Fourier velocity spectrum, $\Omega_{ij}(f, r)$, observed at a recording station, j , originating from an earthquake, i , can be represented as:

$$\Omega_{ij}(f, r) = 2\pi f E_i(f, f_{ci}) B_{ij}(f, t_{ij}^*) S_{ij}(r, r_{0\dots n-1}, \lambda_{1\dots n}) T_j(A_j, f, \kappa_j) I_j(f), \quad (4.7)$$

where f is the frequency, r is the hypocentral distance, $E_i(f, f_{ci})$ is the source model (the far-field displacement spectrum), $B_{ij}(f, t_{ij}^*)$ is the attenuation along the ray path, $S_{ij}(r, r_{0\dots n-1}, \lambda_{1\dots n})$ is the frequency independent amplitude decay

with distance, $T_j(A_j, f, \kappa_j)$ is the site amplification function at the station and $I_j(f)$ is the instrument response function. The source spectrum is modelled by:

$$E_i(f, f_{ci}) = \Psi_{0i} \frac{1}{\left(1 + \left(\frac{f}{f_{ci}}\right)^2\right)}, \quad (4.8)$$

[Brune, 1970, 1971], where Ψ_{0i} is the long-period plateau value at the source and f_{ci} is the source corner frequency. Assuming whole path attenuation, the attenuation along the path of propagation is:

$$B_{ij}(f, t_{ij}^*) = e^{\left(-\pi f \frac{\tau_{ij}}{Q_{0ij}}\right)} = e^{(-\pi f t_{ij}^*)} \quad (4.9)$$

where τ_{ij} is the travel time, Q_{0ij} is the dimensionless quality factor [e.g. Ritbrock, 2001], and t_{ij}^* is the whole path attenuation operator. We choose to model frequency independent Q , as the frequency dependence of Q is difficult to derive and may introduce further trade-offs. For instance, Drouet et al. [2010] show that there are negligible differences in the residual misfit to data recorded in France for eight independently derived Q models (with $Q(f) = Q_0 f^\alpha$) with frequency dependence ranging between $\alpha = 0$ and 1.1. In fact Q is well known to trade-off with other parameters in spectral deconvolution methods. However, it is important to note that we are interested in this case in relative variations at individual stations. On average, and by definition, the inversion residuals are flat over the ensemble of recordings at all stations. It is only site-specific variations that are later extracted for analysis. Therefore, regardless of what we choose to predefine (e.g., frequency dependence of Q), other parameters (such as the source corner frequency) may accommodate the changes due to trade-offs and result in flat residuals over the ensemble of recordings. However, site to site variations extracted from the residuals will be relatively unaffected by this trade-off due to the averaging over many earthquakes, distances, and depths.

The apparent geometrical spreading function, which may include factors such as phase interference and dispersion, focusing or defocusing and scattering [e.g. Atkinson and Mereu, 1992], is described by a piecewise function comprising of segments of constant exponential decay:

$$S_{ij}(r, r_{0\dots n-1}, \lambda_{1\dots n}) = \left\{ \begin{array}{ll} \left(\frac{1}{r}\right)^{\lambda_1} & r \leq r_1 \\ S(r_1) \left(\frac{r_1}{r}\right)^{\lambda_2} & r_1 \leq r \leq r_2 \\ \dots & \dots \\ S(r_1) \left(\frac{r_n}{r}\right)^{\lambda_n} & r \geq r_n \end{array} \right\}. \quad (4.10)$$

Finally, the local site transfer function is given by:

$$T_j(A_j, f, \kappa_j) = A_j a_j(f) e^{-\pi f \kappa_j}, \quad (4.11)$$

where A_j is the average site amplification relative to the unknown reference rock profile (the average amplification over all frequencies), κ_j is a constant, site-related attenuation operator [e.g Anderson and Hough, 1984] and $a_j(f)$ is the frequency dependent site amplification function. The data are carefully corrected for instrument response such that $I_j(f) = 1$.

The deconvolution of the model parameters is therefore solved in a two-stage approach. First the frequency dependent model components are obtained: that describing the source model, controlled by f_{ci} , the path attenuation, controlled by $t_{ij}^* + \kappa_j$, and normalized site amplification $a_j(f)$, along with a combined amplitude parameter, the signal moment:

$$\hat{\Omega}_{ij} = \Psi_{0i} A_j S_{ij}(r, r_{0\dots n-1}, \lambda_{1\dots n}). \quad (4.12)$$

The following minimization function is used:

$$\xi = \sum_{f=f_{start}}^{F_{end}} \frac{(\log(\Omega_{ij}^o(f)) - \log(\Omega_{ij}^m(f)))}{f}, \quad (4.13)$$

where o refers to the observed data and m the modelled data. The use of $1/f$ down-weights the higher frequency content of the spectra in favor of fitting the low-frequency plateau and source corner-frequency. This is a subjective choice taken in order to reduce the influence of more numerous high frequency data and is similar to transforming the parameter space into the log-log domain [e.g. Ide et al., 2003]. A grid search around f_{ci} is performed with a Powell's minimization [Press et al., 1997] of equation 4.13 to find $t_{ij}^* + \kappa_j$ and the signal moment. Using the minimum misfit model, the factorial residuals, given by:

$$\theta_{ij}(f) = \frac{\Omega_{ij}^o(f, r)}{\Omega_{ij}^m(f, r)}, \quad (4.14)$$

can then be used to reconstruct the frequency-dependent site function by taking the log-space mean of the factorial residuals at discrete frequencies over all events ($i = 1, 2, 3 \dots n$) at a specific station, j :

$$\log(a_j(f)) = \frac{1}{f} \left(\sum_{i=1}^n \log(\theta_{ij}(f)) \right). \quad (4.15)$$

The signal moments are used in a second stage to separate the frequency-independent parameters: Ψ_{0i} , A_j and $S_{ij}(r, r_{0\dots n-1}, \lambda_{1\dots n})$. The geometrical spreading term $S_{ij}(r, r_{0\dots n-1}, \lambda_{1\dots n})$ is assumed to be consistent with initial spherical decay followed by trapped surface wave (cylindrical) spreading after $150km$ from the source: $r_0 = 1km$, $r_1 = 150km$; $\lambda_1 = 1.0$ and $\lambda_2 = 0.5$. The signal moments can be expressed as a sum by taking the logarithm of equation 4.12:

$$\log(\hat{\Omega}_{ij}) = \log(\Psi_{0i}) + \log(A_j) + \log(S_{ij}(r, r_{0\dots n-1}, \lambda_{1\dots n})). \quad (4.16)$$

Which can be solved using a least-squares (L2) minimisation with a singular value decomposition (SVD) algorithm [Press et al., 1997; Pozo, 2004]. The inversion is constrained by assuming:

$$\sum_{j=1}^n \log(A_j) = 0, \quad (4.17)$$

such that the parameter A_j is defined as an amplification relative to the reference rock. Data constraints are applied to prevent poorly determined parameters: the number of observations of one event, and the overall number of observations at a station must both be greater than or equal to 10. In reality the number of recordings at the stations used in this study ranged from 13 to 360.

In order to assess whether the assumption that the geometrical decay can be described by spherical - followed by cylindrical - spreading, as defined by equation 4.10, we first compute the residual misfit of the far-field long-period plateau of the spectra ($\hat{\Omega}_{ij}$). In this preliminary test, we invert for the long-period plateau of the spectra whilst accounting for this simple geometrical decay function, but without the use of site terms (A_j). The resultant misfit is shown in Fig. 4.4. On average there are no significant trends apparent with

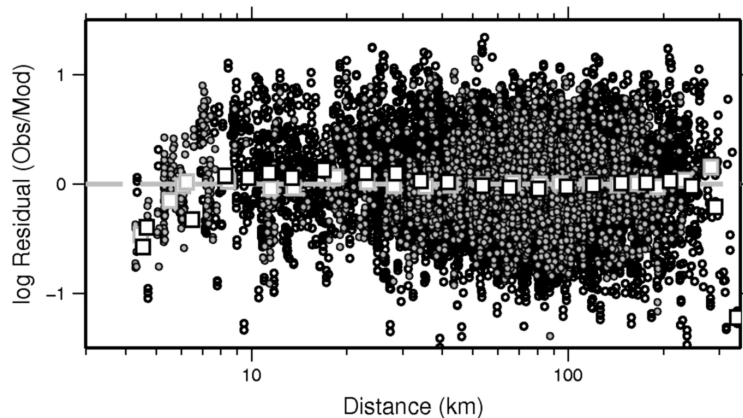


Figure 4.4: Residual misfit of $\hat{\Omega}_{ij}$ (the far-field long period displacement plateau) for magnitudes greater than 3 and distances greater than 10km after being fit with the geometrical decay function described by equation 4.10 and $r_0 = 1km$, $r_1 = 150km$; $\lambda_1 = 1.0$ and $\lambda_2 = 0.5$. Gray symbols: from events occurring in the Swiss foreland. Black symbols: from events occurring in the Swiss Alps. Squares indicate average residual at a given hypocentral distance.

distance. We therefore use this decay function when inverting for the site terms (A_j) in order to avoid any trade-off between the parameters.

In this application the site terms $\bar{T}_j(A_j, f)$ were required, independent of attenuation, so they were reconstructed from A_j and $a_j(f)$ such that:

$$\bar{T}_j(A_j, f) = A_j a_j(f), \quad (4.18)$$

e.g., Fig. 4.5. The uncertainty was propagated into $\bar{T}_j(A_j, f)$ from A_j and $a_j(f)$. 17300 records (including both horizontal components) from 585 earthquakes occurring in Switzerland with $M_L > 2.0$ were used to define the $\bar{T}_j(A_j, f)$ for 77 sites in Switzerland, including the 27 used in this study [Edwards et al., 2009]. The multi-taper algorithms [Lees and Park, 1995; Park et al., 1987] with $5-3\pi$ prolate tapers were used to compute the Fourier spectra of the combined S-wave and coda of these earthquakes. The analysis window was defined following the method proposed by Raoof et al. [1999] to encapsulate 5% to 75% of the cumulative squared velocity of the record (a measure of significant shaking). A noise window is chosen to be as long as possible in order to enable the correct recovery of any long-period noise. It starts at the beginning of the trace, and continues over a duration equal to 75% of the time until the P-wave arrival. This also ensures that potentially inaccurate P-wave arrival time picks (or estimates) do not lead to the noise window being

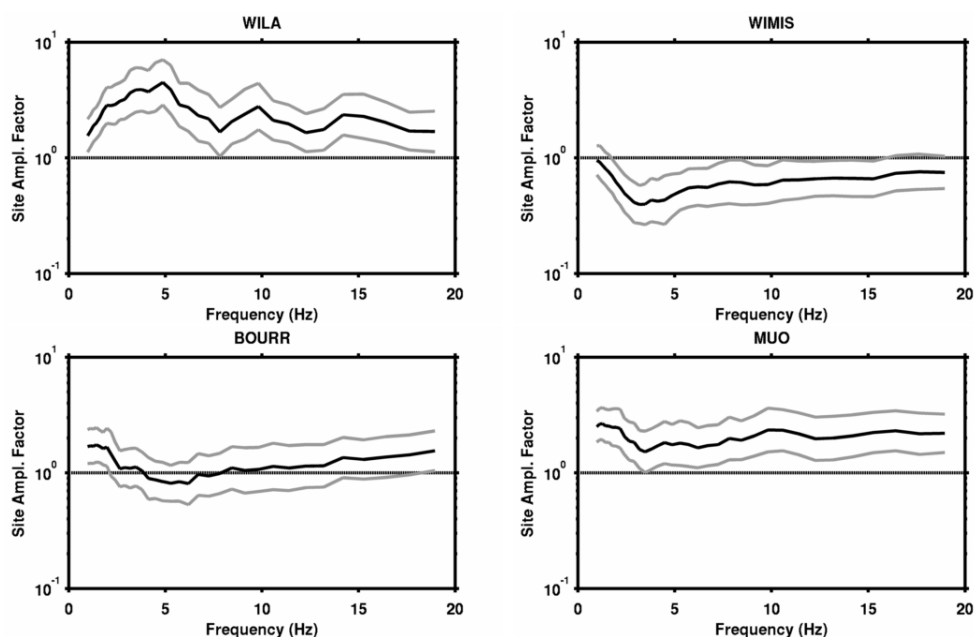


Figure 4.5: Examples of amplification function from spectral modelling. The black line shows the mean amplification, whilst the grey lines indicate the standard deviation. The amplification functions are referenced to an unknown site condition that is later defined as part of this study.

contaminated by the P-arrival. A signal to noise ratio of over three was then required to include the data in the inversion.

In a future stage of our research, we plan to free more of the parameters of the spectral modelling, in order to assess the robustness of the results. One possibility is to follow a two-step non-parametric generalized inversion, as proposed by Castro et al. [1990] and used by other authors [e.g. Parolai et al., 2004; Bindi et al., 2006]. This might help in reducing the number of assumptions used to constrain the inversion procedure, such as using $1/R$ geometrical spreading or modelling attenuation using a simple exponential function.

4.5 Quarter-wavelength velocity versus computed amplification

At each station location, quarter-wavelength velocity curves were correlated with the estimated amplification functions from the spectral modelling ap-

proach. The correlation was made over a set of discrete frequencies in the range between 1 and 15 Hz. The choice of using 1 Hz as the lowest resolvable frequency for the computation comes from the fact that the velocity profiles from both MASW and array analysis are optimistically reliable only down to a depth range between 50 and 150 m. This limitation can be partially overcome by the smoothing effect of the quarter-wavelength representation and introducing some a-priori constraint, such as forcing the extended profile to have a gradient. However including frequencies lower than 1 Hz might lead to erroneous results, as was experienced. For each frequency a relationship between the average quarter-wavelength velocity and expected amplification was defined in the log-space using a weighted orthogonal linear least-squares regression over the station samples [Krystek and Anton, 2008]. The regression facilitates the estimation of amplification for average velocity classes that are not covered by direct measurement (Fig. 4.6). The weighting scheme used allows the consideration of uncertainty in both parameters. Finally, for each relationship, confidence bounds are computed from the orthogonal standard deviation of the residuals.

For most of the frequencies, a clear linear correlation is observed. However, in some cases (e.g. 3-5 Hz) the correlation between low velocity values (300 to 750 m/s) and amplification is less well defined. This may be due to a lack of resolution of the MASW measurements at greater depths. More likely, however, is that this is due to the irregular shape of the amplification functions at these frequencies: typically a resonance minimum is present (Fig. 4.5, e.g. stations BOURR at 5 Hz and WIMIS at 3 Hz) or a resonance maximum (e.g. station WILA at 5 Hz). Consequently the correlation functions exhibit some scatter with respect to the empirical amplification (Fig. 4.7).

For each analysed frequency relation, it was assumed that the reference condition's average velocity corresponds to amplification equal to unity in the regression. Consequently, a quarter-wavelength representation of the whole reference profile could be reconstructed (as $\bar{V}_s^{QWL}(f)$ and $\bar{z}^{QWL}(f)$), extracting the ensemble of selected quarter-wavelength velocities that show null amplification over the range of different frequencies (Fig. 4.8). The resulting profile shows a clear trend, with average velocity of about 1000 m/s at the surface, progressively increasing with increasing depth.

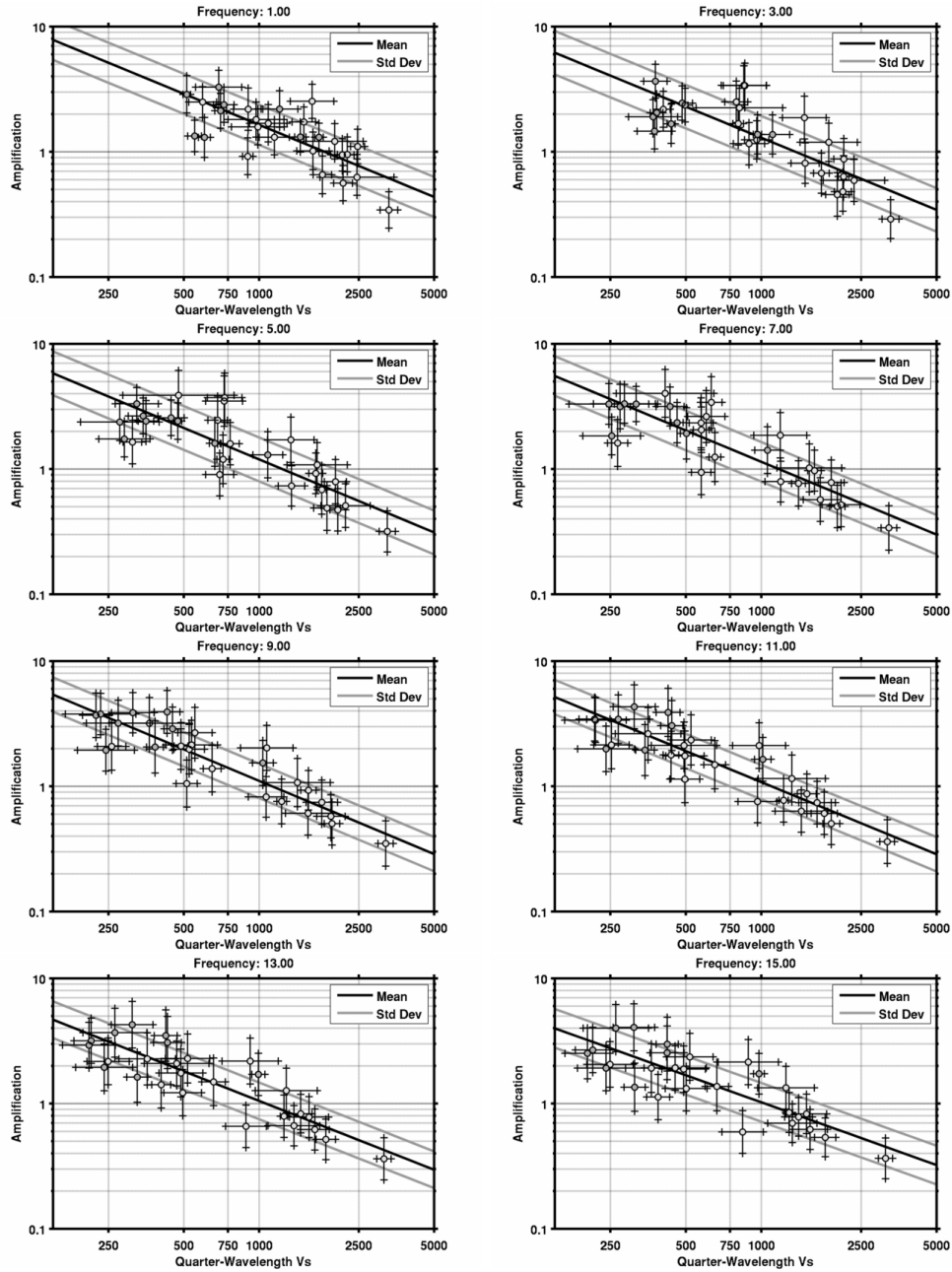


Figure 4.6: Correlation between quarter-wavelength average velocities (MASW with dots in light grey, ambient noise in dark grey) and amplification factors from spectral modelling of earthquake spectra. A linear least-squares regression is applied in log-log scale to estimate parameter correlation.

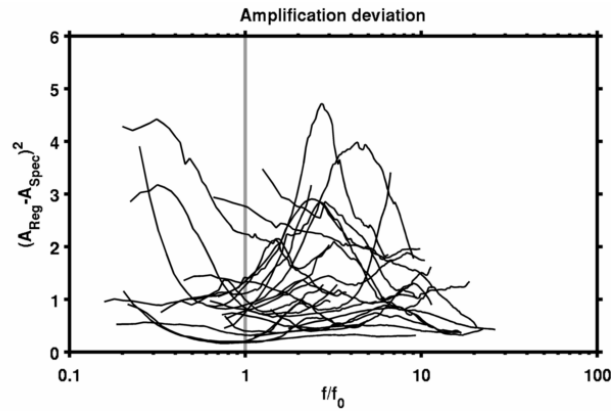


Figure 4.7: Quadratic residuals (in log-statistics) from the comparison of the empirical amplification functions and the mean amplification from the regression with quarter-wavelength average velocities. For each curve, the frequency axis has been normalized to the SH fundamental frequency of resonance of the site (f_0). It is clear that deviations generally increase before and after the f_0 value ($f/f_0 = 1$).

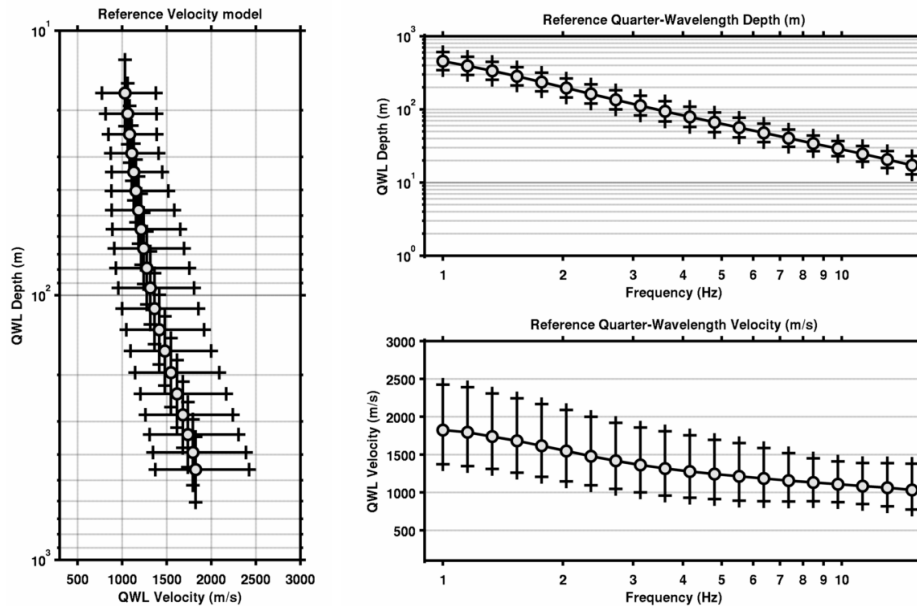


Figure 4.8: Quarter-wavelength representation of the reference velocity profile. On the left the profile is presented with average velocity versus depth; on the right the frequency dependency of the QWL parameters is emphasized.

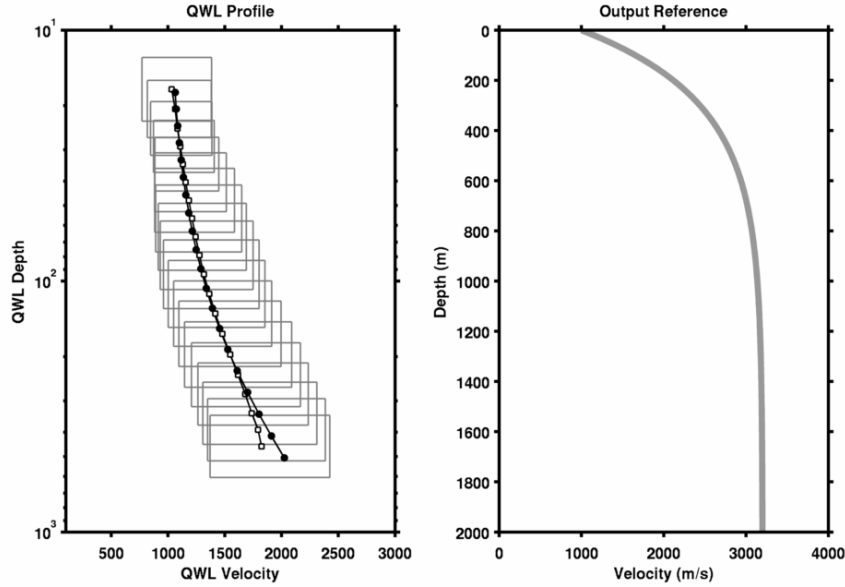


Figure 4.9: Reconstruction of the reference velocity profile from its quarter-wavelength representation. On the left, the fit between the observed (white dots) and the inverted (black dots) profiles. On the right, the corresponding best fitting model in gradient form.

4.6 Inverting for a gradient model

The previous analysis provided a reference quarter-wavelength velocity profile that was defined to have null average amplification of the sites relative to the reference. However, this profile cannot be directly used for computing the site-to-reference SH amplification function. Reconstructing the standard V_s velocity profile from its corresponding quarter-wavelength representation is achieved by means of a global optimization procedure. A simplified gradient velocity profile is used for the inversion. The proposed equation is exponential, but differs with respect to other gradient models in literature [e.g. Faust, 1951] in the use of the coefficients to define the gradient bending (curvature parameters a and b) along with the possibility of including a-priori information about the lower bedrock velocity.

$$V_s(z) = (V_{s_{max}} - V_{s_{min}}) \left[1 - a \left(\frac{z_{top} - z}{b} \right) \right] + V_{s_{min}}. \quad (4.19)$$

This last point is fundamental, because no information about depths greater than about few hundreds meters (here roughly higher than $200 \sim 250m$) can be extrapolated from the measurements. Consequently, a velocity constraint

must be defined. In our approach the lower bedrock velocity ($V_{s_{max}}$) is based on the estimation of the V_s velocity at $4000m$ obtained from P-wave crustal travel-time tomography [Husen et al., 2003], assuming a V_p/V_s ratio of 1.73 (or Poisson's ratio 0.25 for the upper-crust). The estimated value is around $V_{s_{max}} = 3200m/s$. The link depth has been determined according to the resolution limits of tomographic models at shallower depths, which typically provide unreliable estimations coarsely above $2000m$ depth. Using this reference lower bedrock velocity, the inversion routine fits the best gradient model with curvature (a and b) and upper-link velocity ($V_{s_{min}}$ estimate at the depth z_{top}) to the quarter-wavelength data obtained previously.

Inverting a quarter-wavelength profile consists of a double dataset-fitting problem. Both quarter-wavelength velocity and depth ($\bar{V}_s^{QWL}(f)$ and $\bar{z}^{QWL}(f)$) curves versus frequency of the reference have to be fit simultaneously. A cost function is calculated over the frequency range from 1 to $15Hz$ using L2 norm assuming log-normal statistics:

$$M_{V_s} = \sum_{f=1}^{15Hz} \left(\frac{\log \left(\bar{V}_{s_f}^{QWL,Obs} \right) - \log \left(\bar{V}_{s_f}^{QWL,Syn} \right)}{\sigma \left(\bar{V}_{s_f}^{QWL,Obs} \right)} \right)^2. \quad (4.20)$$

$$M_z = \sum_{f=1}^{15Hz} \left(\frac{\log \left(\bar{z}_f^{QWL,Obs} \right) - \log \left(\bar{z}_f^{QWL,Syn} \right)}{\sigma \left(\bar{z}_f^{QWL,Obs} \right)} \right)^2. \quad (4.21)$$

where *obs* indicates the reference profile derived from the $V_s^{QWL}(f)$ – amplification correlations at discrete frequencies f , and *syn* the inverted profile. Uncertainties on both parameters are taken into account. A global misfit is then computed as a simple sum:

$$M_{Global} = M_{V_s} + M_z. \quad (4.22)$$

The results of the optimization are shown in Fig. 4.9, with best fit for the profile parameters $a = 1.30$, $b = 78.16$ and $V_{s_{min}} = 1000m/s$. Some discrepancies between the data and model are apparent below $300m$. However, the deviation is within the error bounds of the input.

4.7 Comparison with previous reference profiles

In Fig. 4.10, the reference profile is presented together with shear-wave velocity profiles from P-wave regional tomography [Husen et al., 2003] at three selected stations: HASLI, WEIN and LLS. For the conversion, a P:S velocity ratio of 1.73 is used. The purpose of this comparison is to show how the proposed reference integrates and extends the tomographic profiles at shallow depths. As mentioned, profiles from crustal travel-time tomography have no resolution at shallower depths due to the lack of crossing ray-paths in this region. Moreover, the spacing between grid nodes is generally insufficient to produce a sufficiently detailed representation of the structure in the upper layers. Unfortunately, shallower velocities have an important influence on the modification of the final ground motion. For this reason, the sole use of tomographic profiles should be avoided in the calibration of ground motion prediction equations. However, as in the present work, the velocity values from these profiles at greater depths are useful for the calibration of the reference profile, since no reliable constraint can be obtained at these depths from direct low-cost measurements.

The reference profile computed using the quarter-wavelength approximation has also been compared with previous reference velocity profiles from ambient noise recordings constrained by borehole measurements [Takahashi and Suzuki, 2001] and an interpretation of reflection and refraction studies [Campus and Fäh, 1997; Fäh et al., 2003] in selected regions of Switzerland (Fig. 4.11). It should be noted that, within the group, the models *Zentralschweiz*, *Innerschweiz 01* and *Innerschweiz 02* are solely representative of the Alpine and pre-Alpine regions, while only *Mittelland* and *Basel* (named *Average Model* in Fäh et al. 2003) describe the Swiss Alpine Foreland. The proposed reference is generally in agreement with the measurements. It generally matches the average trend of the whole set of profiles. Some discrepancies are present at very shallow depths, where the velocities in our model (about 1000m/s) are slightly higher than the average from ambient noise recordings (around 600m/s), but lower than those from the interpretation of seismic surveys (greater than 2000m/s in some models). This can be explained by considering that ambient noise techniques are generally sensitive to the uppermost low-velocity layers such as soft sediment cover or weathered rock soils, while seismic surveys tend to be more insensitive to the uppermost structure. Ambient noise profiles are also subject to a progressive lack in resolution with increasing depth. This might result in a biased estimation of the seismic velocity at greater depths, especially when very-soft sediments are present at the

surface. Apart from the fact that the profiles are all located in the Northern Swiss Foreland, such “smoothing” effects might also explain the discrepancies in gradient slopes between the presented datasets. Note however that the proposed reference profile has to be considered as the solution that “explains” the data in term of amplification. It is solely representative of a pure theoretical rock condition, averaged over the different sites used to define the predicted ground motion. Consequently, it might not necessarily match an existing profile from a specific area.

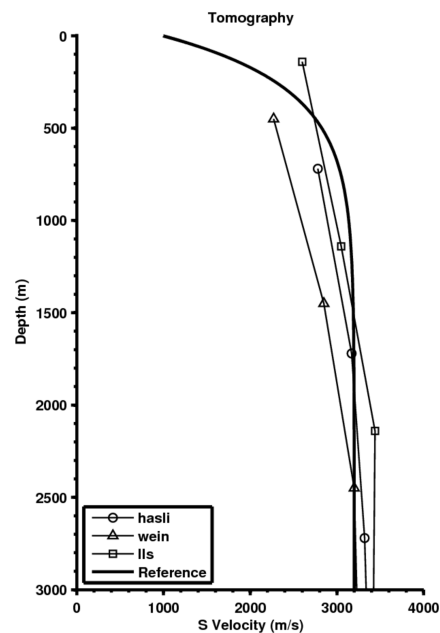


Figure 4.10: Comparison between profiles from converted P-wave travel time tomography in selected regions of Switzerland with the proposed reference. Tomographic profiles have been used to constrain the bedrock velocity of the reference at a large depths during the inversion.

The retrieved reference was compared with two generic rock velocity models proposed by Boore and Joyner [1997] for North America. These profiles are often used in practice as reference for the GMPEs and are based on two different assumptions. The first profile (Fig. 4.12, curve A) was established to represent the average condition for rock sites of engineering significance, while the second (Fig. 4.12, curve B) is specifically representative of very hard rock sites, such as those where glacial erosion removed the uppermost weathered part. If compared with the proposed reference, some differences are noticeable.

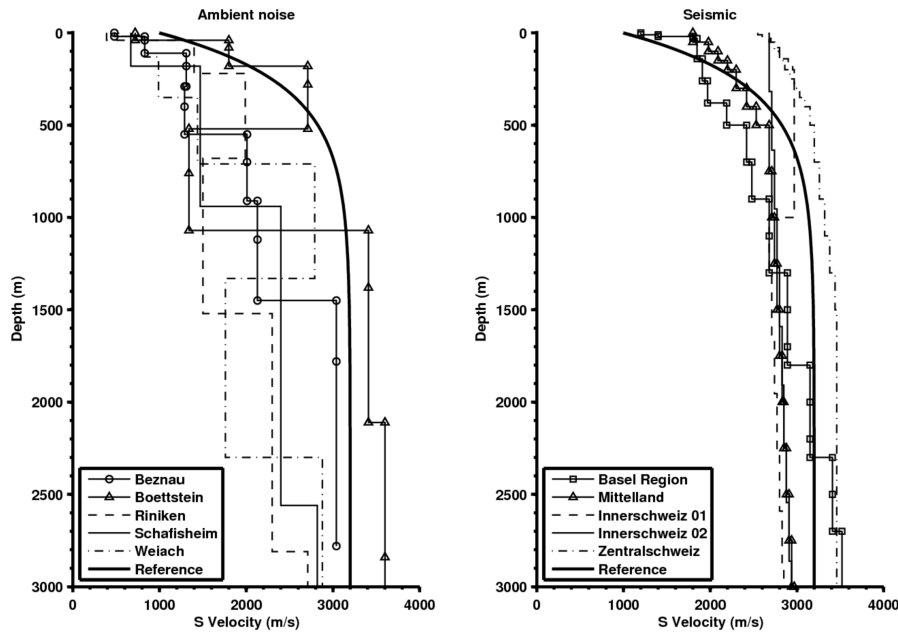


Figure 4.11: Comparison of the proposed reference velocity profile with previous references from independent studies in Switzerland; on the left, profiles from array processing of ambient noise [Takahashi and Suzuki, 2001] and, on the right, interpretation of seismic refraction and reflection studies [Campus and Fäh, 1997; Fäh et al., 2003].

In particular, the presented reference profile shows considerably higher velocity at shallow depths ($V_{s30} = 1106\text{m/s}$) than profile A ($V_{s30} = 618\text{m/s}$), but remarkably lower than profile B ($V_{s30} = 2880\text{m/s}$). This intermediate condition might be explained by the differences in lithology and dynamic setting between the study areas. Differences in the gradient slope are also evident. However, this is probably induced by the different forms of the equations used to model the profiles and, as mentioned before, by the velocity constraints imposed at depth.

4.8 Reference amplification model

From the inverted velocity profile, amplification functions were computed. Two distinct approaches were followed. First, the one-dimensional SH-wave transfer function was computed for vertical wave propagation following the Knopoff layer-matrix formulation [Knopoff, 1964]. Unfortunately, no reliable estima-

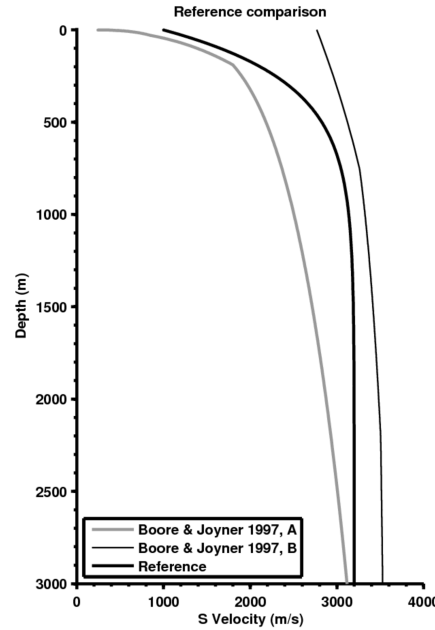


Figure 4.12: Comparison between the reference S-wave velocity profile proposed for Switzerland with the results from Boore and Joyner [1997] for North America. Profile A is representative of a generic rock condition, while in B the reference is computed for very-hard rock sites.

tion of density was obtained from direct measurements (dispersion curve inversions have virtually no resolution on this parameter). Consequently, it was not possible to reconstruct and use any reference density profile with the proposed method. For this reason, a constant value of $2500\text{kg}/\text{m}^3$ has been established for the whole reference profile. Such approximation is acceptable if no large density variations are expected. In fact, the relative amplification is weakly affected by this parameter. As an example, a density contrast between $2100\text{kg}/\text{m}^3$ (at the top) and $2900\text{kg}/\text{m}^3$ (at the bottom) will affect the maximum amplification, with respect to the proposed constant model, by a factor 1.16 only. As the crustal reference, a homogeneous half-space with a constant shear-wave velocity of $3200\text{m}/\text{s}$ and density of $2500\text{kg}/\text{m}^3$ is assumed. The model is purely elastic and no attenuation has been considered, as this can be applied separately. Next, the spectral amplification from quarter-wavelength approximation was computed, as described in Boore and Joyner [1997]. Following this approach, amplification is given as the square root of the ratio between the average seismic impedance at the corresponding quarter-wavelength depth

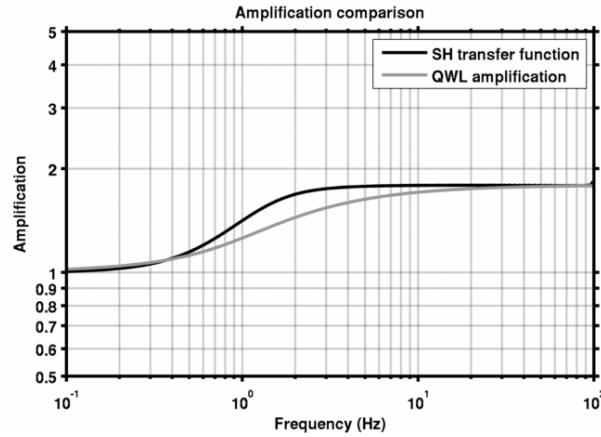


Figure 4.13: Absolute value of the 1D SH transfer function and the amplification from the quarter-wavelength method computed for the proposed reference rock profile, assuming a common constant crustal reference of 3200m/s . Some differences in the amplification level are noticeable in a frequency band between 0.5 and 10Hz .

and the impedance of the reference (equation 4.6). As in the previous case, a constant S-velocity (V_s^C) of 3200m/s and density (ρ^C) of 2500kg/m^3 were assumed as a reference.

In comparison, the amplification functions from the two approaches look similar and partially overlap (Fig. 4.13). This is expected in the case of a simplified gradient model with no large contrasts of impedance at depth, which would, if present, give rise to the characteristic resonance peaks in the SH transfer function representation. However, some differences are present around 1Hz , where the SH transfer function is higher than is computed from simple impedance ratios. In order to be conservative, it was therefore decided to adopt the SH-wave model as a more reliable representation of the reference amplification. In more detail, the amplification function is a ramp function, which asymptotically converges to a stable value of about 1.78 at high frequencies (the plateau level). The bending of the curve is controlled by the curvature of the inverted gradient profile. The stronger variation of amplification occurs over a range between 0.5 and 10Hz .

In comparison to the amplification functions of reference profiles derived from interpretation of seismic refraction and reflection surveys of Fig. 4.11, the SH wave amplification of the proposed reference shows some differences (Fig. 4.14). The average level of amplification is generally higher for frequencies greater than 1Hz . The *Basel* profile is the most similar in terms of amplification, especially in the plateau region. Conversely, *InnerSchweiz*

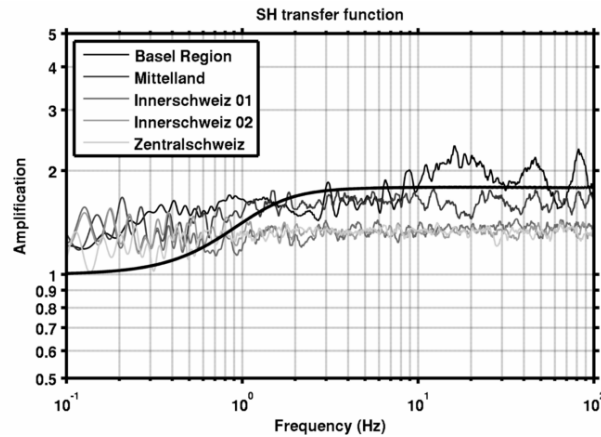


Figure 4.14: Comparison between SH amplification function of the reference profile (thick line) and those from the interpretation of seismic refraction and reflection studies in Switzerland. The proposed amplification model is representative of the Swiss Foreland and is therefore more consistent with the amplification models for the *Basel* region and the *Mittelland*.

and *ZentralSchweiz* profiles are models representative of the Alpine and pre-Alpine areas and give rise to considerably lower amplification. As previously described, this is induced by higher near-surface velocities in the Alpine region. Such high velocities are thought not to be representative of the average reference condition of Switzerland.

Finally, the amplification function of the reference is compared with those from the two rock profiles proposed for North America by Boore and Joyner [1997] (in Fig. 4.12). As in the previous cases, no attenuation was considered for the computation. Specifically, the amplification function for the generic rock site condition of North America (Fig. 4.15, curve A) is always higher than the one computed for the proposed reference. Differences are consistent especially at high frequencies ($> 20\text{Hz}$), where profile A shows amplification up to 2 times higher than the Swiss reference. This is clearly induced by the choice of very low velocities ($< 600\text{m/s}$) at shallow depths, which appear to be not applicable for Switzerland. On the other hand, profile B has amplification nearly flat and close to 1 for all frequencies. This is expected for very hard rock conditions, but might be inappropriate as use for a standard reference, where the average effect of weathered and fractured rock conditions should be taken into account.

The maximum level of amplification of the reference transfer function is controlled by the velocity contrast between the uppermost part of the profile and the crustal basement. However, since the velocities at shallow depths

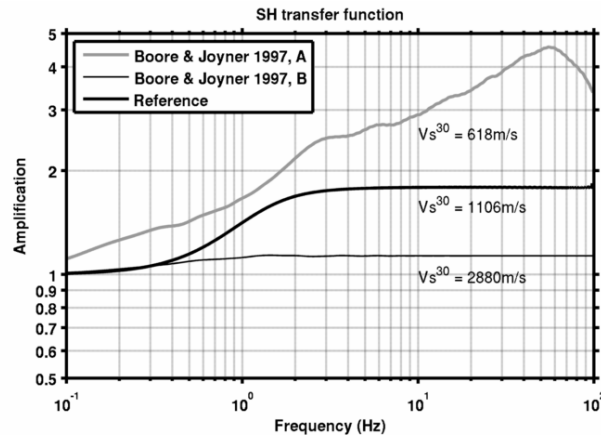


Figure 4.15: Amplification function of the proposed reference compared to the results from Boore and Joyner [1997] for North America. In A is given the amplification for a generic rock site, while in B for very hard-rock conditions. V_{s30} estimations for each profile are also presented to emphasize the differences in average amplification, especially at high frequencies.

are constrained by direct measurement, the amplification at high frequencies (the plateau region) will be strictly conditioned by the choice of the lowermost velocity constraint. Clearly, some uncertainties are present in the definition of both parameters, and this may be reflected in the average level of amplification. We tested the variability in the amplitude of the plateau by changing the upper and lower velocity links of the reference profile (Fig. 4.16). The upper velocity was allowed to vary between 940 and 1060 m/s , and the lower between 3000 and 3400 m/s . This led to variations in the amplification factors between 1.68 and 1.89, corresponding to an uncertainty of less than 10% in the proposed reference value.

4.9 Back-computation of the amplification functions

Coefficients from the correlation between quarter-wavelength average velocities and empirical amplification from spectral modelling can be used to reconstruct the frequency-dependent amplification function for sites with a quarter-wavelength velocity profile (Table 4.1). To assess the consistency of the results, we compare the reconstructed amplification with the empirical and theoretical amplification functions for those sites that have been surveyed with passive

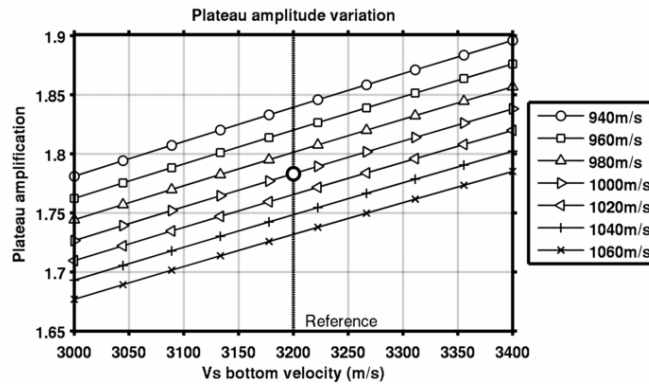


Figure 4.16: Variations in the amplitude of the plateau region of the reference amplification function induced by different bottom (on x axes) and upper layer velocities (marked curves). The actual reference is marked with a circle at the corresponding bottom V_s velocity of 3200m/s .

array analysis. The choice of using this set of locations is driven by the fact that ambient noise processing provides higher resolution of the velocity structure at depth. A more accurate theoretical amplification function can then be modelled.

A good agreement is generally present when comparing the reconstructed amplification functions with those from the empirical spectral modelling approach. Amplifications reconstructed from the QWL Velocity - amplification correlations are incapable of reproducing the small features typical of an empirical function, such as peaks and troughs (e.g. SMZW, Fig. 4.17c), at sites with unconsolidated sediments. The trend is nevertheless clearly preserved. Sometimes, an offset is exhibited between the two functions (e.g. SULZ, Fig. 4.17b). Such a discrepancy, however, can be easily explained by the fact that the linear regression produces a common least-square solution, but the local amplification at a site can be locally deviated from the retrieved average. The local amplification, moreover, might be influenced by a velocity jump at depths not resolved by the S-wave measurements.

As mentioned, amplification factors reconstructed from the correlation have also been compared with theoretical 1D amplification functions, using SH transfer function formalism. For the computation of amplification using SH-wave site response, the proposed reference profile was used. The comparison shows good agreement between the amplification curves for sites with larger V_{s30} . Some discrepancies between the empirical amplification and the reconstructed amplification are noticeable (Figure 4.14c), but most of times the curve falls within the error bounds of the regression.

Qwl-Vs (m/s)	Frequency (Hz)									
	1	2	3	4	5	6	7	8	9	10
200	6.18	5.05	4.88	4.66	4.57	4.36	4.36	4.34	4.24	4.24
300	4.42	3.67	3.49	3.33	3.26	3.12	3.11	3.09	3.02	3.01
400	3.49	2.92	2.75	2.62	2.56	2.45	2.45	2.42	2.38	2.37
500	2.9	2.45	2.29	2.18	2.13	2.04	2.03	2.01	1.97	1.96
600	2.5	2.12	1.97	1.88	1.83	1.75	1.75	1.72	1.69	1.68
800	1.97	1.69	1.56	1.48	1.44	1.38	1.37	1.35	1.33	1.32
1000	1.64	1.42	1.29	1.23	1.19	1.15	1.14	1.12	1.1	1.1
1250	1.37	1.19	1.08	1.02	0.99	0.95	0.95	0.93	0.92	0.91
1500	1.17	1.03	0.93	0.88	0.85	0.82	0.81	0.8	0.79	0.78
2000	0.93	0.82	0.73	0.69	0.67	0.65	0.64	0.62	0.62	0.61
2500	0.77	0.69	0.61	0.58	0.56	0.54	0.53	0.52	0.51	0.51
3000	0.66	0.59	0.52	0.5	0.48	0.46	0.46	0.44	0.44	0.44

Table 4.1: Mean amplifications computed from the regression between quarter-wavelength velocities and amplification factors from spectral modelling of earthquakes.

4.10 Summary and conclusions

A new method to estimate the reference shear-wave velocity profile to be used in probabilistic seismic hazard assessment is proposed. The procedure is based on the comparison between in-situ direct measurements and amplification factors from earthquake spectral modelling. The quarter-wavelength approximation was used to isolate average velocities to be related with frequency dependent amplification.

The reference profile that was retrieved consists of a simplified gradient model with monotonically increasing velocity from about 1000m/s to 3200m/s . Our result is in agreement with studies conducted using different approaches, such as measurements using ambient noise recordings constrained by borehole measurements and interpretation of seismic reflection and refraction techniques. From this profile, the SH-wave transfer function was computed assuming a constant reference of 3200m/s for use in a stochastic model.

The amplification functions derived from spectral modelling of earthquakes were shown to be generally consistent with the results from 1D SH-wave transfer function for stiff soils to rock sites. However, these functions also included small-scale local features that were not possible to model with a simplified approach. It was shown that amplification functions for specific sites in Switzerland with a quarter-wavelength velocity profile could be reconstructed using

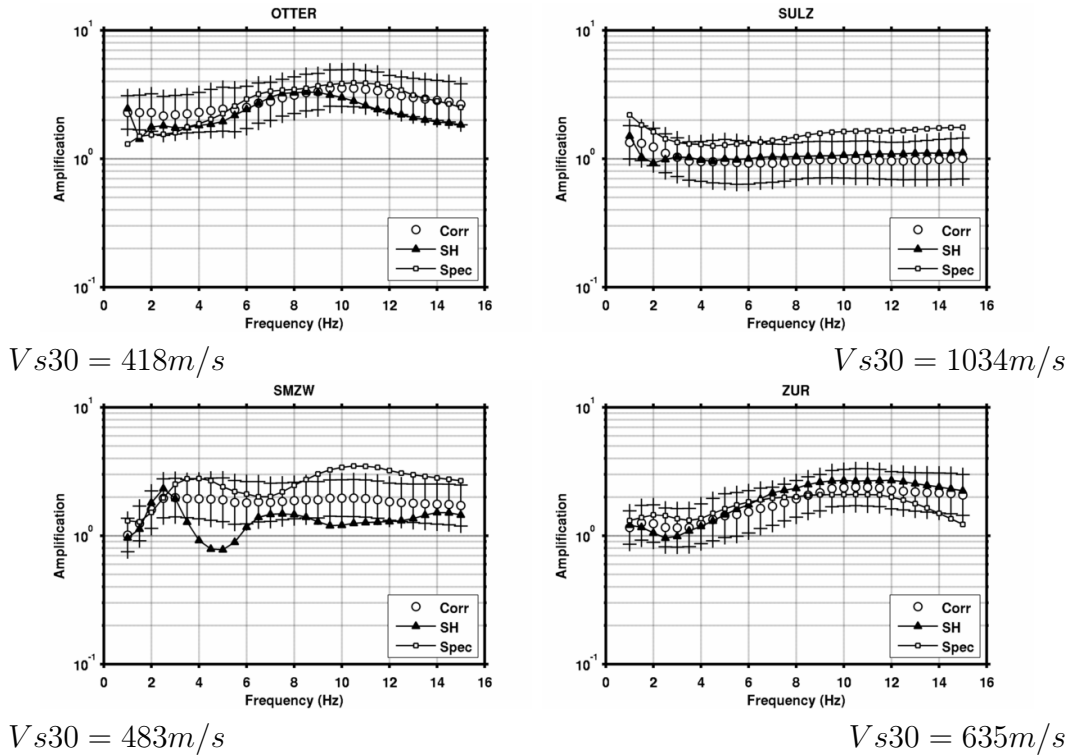


Figure 4.17: Generic amplification functions (Corr) can be reconstructed from the coefficients of the correlations between average QWL-velocities and empirical amplifications at all stations. The empirical amplification for the specific station is also given (Spec). The result is consistent with the modelled site-specific amplification using the SH-transfer function (SH), especially for the sites with higher S-wave velocity at the surface.

the correlation relations defined in this study. The general trend of the amplification functions was recovered when compared to those derived from the SH transfer function for real sites. The reconstructed amplification relations provide a useful alternative method for assessing the site amplification in the absence of earthquake recordings without the necessity of using SH-wave modelling. However, there is space for improvement when the influence of very strong velocity contrasts is included.

The uncertainties in the resulting amplification function have been taken into account. These are mostly induced by the limited extension of our measurement dataset. We are confident that including additional data will improve the statistics. To do this, it is planned to perform additional measurements at seismological station locations for which amplification functions are available from spectral modelling. Moreover, other than active seismic measurements, a

progressively increasing number of results from ongoing and planned ambient noise recording measurements will be added to the dataset. This will increase resolution especially at greater depths. Furthermore, once a larger dataset is available, it is suggested to develop different reference profiles for the main geological domains of Switzerland. This will include the Molasse Basin, the Alpine (including the Prealps) and the Jura regions. It is important to underline that these domains shows considerable differences from the tectonic and lithological point of view, and it would be more appropriate to treat them separately in the context of probabilistic seismic hazard assessment.

4.11 Data and resources

Velocity profiles from ambient noise and MASW analysis are part of the site characterization database of the Swiss Seismological Service (SED). The database will be released to the public in December 2010. Restricted access, however, can be granted before this date upon direct request to donat.faeh@sed.ethz.ch. The 585 earthquake events used for site specific amplification computation have been extracted from the recording database of SED. These data are available for the public through AutoDRM, last accessed May 2010). Other data are available for the public from sources referenced in the paper.

Acknowledgments

This research was supported by the project HAZARD 2010 (S.N.F. No. 200021-112284) and also by the projects PRP (PEGASOS Refinement Project) and SHARE (Seismic Hazard Harmonization in Europe). We acknowledge Geoexpert AG who performed the MASW surveys. We also acknowledge John Douglas, the BSSA anonymous reviewer and the Associated Editor Stefano Parolai, for their helpful comments and suggestions. A final thanks goes to Stefan Fritsche and Gabriela Gassner-Stamm for their help in compiling the measurement database.

Conclusions and Outlook

The analysis of surface waves from active and passive surveys can be advantageous for local seismic hazard estimation and microzonation. The main benefit is the relatively low cost of implementation of such techniques, if compared to more invasive exploration approaches such as borehole logging. I presented new approaches for the analysis of surface waves, together with practical examples of their implementation, and demonstrated the improvements made. In the following, the main findings of this PhD study are summarized.

A method to compute the Rayleigh wave ellipticity function from array analysis of three-component ambient noise recordings was presented. The computation of the signal's power spectrum using the frequency-wavenumber transform is used to correctly estimate the polarization function of Rayleigh waves for the fundamental and, with some limitations, higher modes. This approach minimizes the influence of interfering wave types present in the total wave-field, which is not always possible with common techniques based on single station H/V analysis. In comparison to single-station H/V spectral ratios, we can now distinguish and separate the influence of Love waves. The effect of vertically propagating body wave contributions is also automatically removed by the beamforming.

Reliable results are obtainable for the fundamental mode of Rayleigh waves. Results are also achievable for higher modes, whenever the corresponding dispersion curve is well identified in the slowness-frequency plane and sufficiently energetic. The quality of retrievable ellipticity curves depends on the complexity of the structural model, the array geometry and the noise level. I showed that dispersion curves close to apparent intersection can produce deviations of the amplitude values, due to the difficulty that the adaptive filter has in separating the different contributions. Signals with low energy content, hardly resolvable in the slowness-frequency plane, can lead to unreliable ellipticity values. A progressive reduction in the number of employed seismic receivers drastically restricts the resolution of the method. Sparse spatial sampling can lead to insufficient minimization of body waves, as well as progressively

increased distortion induced by uncorrelated noise.

Slight differences between the values of ellipticity obtained from separately identifying the Rayleigh wave dispersion on the vertical and the horizontal components were noticed. This result is probably due to some residual influence of SH and Love waves. Amplitude ratios from signals picked on vertical components are generally more stable over the whole frequency range and closer to theoretical ellipticity. On the horizontal components, however, the identification of higher mode dispersion is generally more accurate.

A practical example of the ambient noise techniques developed was given for the Lucerne area, a densely populated city. The experiment was carried out in the part of city with thick layers of unconsolidated sediments, for which an estimate of the expected seismic amplification was then provided. To reconstruct the 3D velocity model of the sedimentary basin beneath the city, I optimized the use of the Rayleigh wave ellipticity function obtained from single- and multi-station techniques, in combination with the surface wave dispersion information. The main goal was to improve the level of accuracy in assessing the velocity structure of sedimentary basins, in particular the bedrock depth. As a direct consequence, more realistic amplification could then be modeled. This amplification still needs confirmation from observations using the very recently installed strong motion station in the sedimentary basin of Lucerne.

Two techniques to evaluate the Rayleigh ellipticity function have been tested, a single station method, based on time-frequency analysis, and the frequency-wavenumber method. The two approaches provide comparable results, within the limit of resolution of the methods. The use of wavelet time-frequency analysis to perform H/V polarization analysis has an advantage in that it minimizes the effect of the SH-wave contribution, compared to the classical H/V method. In cases of large velocity contrasts between sediments and bedrock, the result can be reasonably considered representative of the Rayleigh-wave ellipticity function, specifically for the right flank of the fundamental mode Rayleigh wave close to f_0 . The method, however, was not capable to separate the contribution from different modes. By comparing the classical method of computing H/V ratios with the wavelet-based one, it was possible to estimate the relative energy contribution between the SH and PSV components. This result is considered of practical importance, since the relative portion of the SH component is generally unknown when performing H/V measurements. Moreover, I provided a confirmation of the imperfect equivalence between f_0 from ellipticity and f_0 from the SH-wave transfer-function.

A two-step approach was then presented for the combined use of dispersion and ellipticity information from ambient noise recordings. Such an approach

enhances the resolution of deep structures, especially the depth of the bedrock, when compared to classical array techniques. This is particularly suitable in densely populated areas, where only single station measurements are possible and more complex techniques are generally difficult or even impossible to implement. The evaluation of the local seismic response was based on the inverted velocity model using a 1D approximation. Effects such as those due to basin edges or 3D resonances might play a major role in the Luzern area, and are not modeled by 1D site response. Further studies will focus on modeling wave propagation in 3D. Two permanent strong motion sensors are presently installed in Lucerne that will further help to improve the structural model. In dealing with strong motion events, non-linear behavior of the soils is expected which needs geotechnical measurement and techniques that will allow us to model non-linear phenomena.

The frequency band of the dispersion curves was extended with a new approach for surface wave dispersion analysis using active seismic experiments. The proposed method is optimized specifically for use with seismological stations and continuous recordings. It is therefore advantageous in mixed active and passive acquisition surveys, for which single set of equipment can be used. The technique is based on wavefield decomposition using the continuous wavelet transform to perform f-k analysis. This gave the possibility of following the propagation of a surface wave in space with specific phase velocities. In practice, the proposed approach relies on the estimation of surface-wave travel-times to enhance the estimation of the signal covariance matrix. Moreover, stacking the covariance matrix over consecutive wave-field excitations improves the imaging resolution of surface wave dispersion in noisy environments. It was shown that such an approach enhances the resolution of higher modes, which is particularly evident in case of high levels of uncorrelated noise, as observed in urban environments. Combining active seismics with the processing of ambient noise recordings, I improved the resolution at high frequencies, where ambient vibrations generally do not have a coherent wavefield. A disadvantage, however, is that the presented method is computationally more expensive if compared to previous f-k methods, since it requires the re-computation of the covariance matrix for any permutation of the analyzed frequencies, phase velocities, source delay-times and shot number.

I tested the technique on synthetic records, as well as on a real case in the city of Lucerne. In both cases, multiple modes of surface waves were detected. For the Lucerne experiment, the results are consistent with an estimation of the Rayleigh wave fundamental mode dispersion curve obtained from the passive acquisition survey performed at the same location. In this example it was

shown that the combination of active seismics with ambient noise processing compensates for the limitations of the two individual methods. As a future development I am confident that the presented method can be successfully extended, with few modifications, to ambient noise processing, to enhance the capability of separating out the different wave contributions (e.g. body and surface waves). We plan to extract and analyze, other than dispersion, the surface wave amplitude information from t-f-k power spectrum estimates. On three-component recordings, for example, this might allow the estimation of the Rayleigh wave ellipticity function in active seismic experiments.

Finally a method for the definition of the reference rock velocity profile for a stochastic ground motion prediction equation and probabilistic seismic hazard assessment is introduced. The method is based on the comparison between in-situ measurements of average shear wave velocity at recording sites and empirical amplification functions from spectral modeling of earthquakes. The quarter-wavelength representation is used to describe average velocities that can be related to frequency dependent amplification. The derived reference rock profile is in agreement with studies conducted using different approaches, such as measurements using ambient noise recordings on very large arrays constrained by borehole measurements and interpretation of seismic reflection and refraction techniques.

The amplification functions derived from spectral modeling of earthquakes were shown to be generally consistent with the results from 1D SH-wave transfer function modeling of stiff soils to rock sites. However, these functions also included small-scale local features that were not possible to model with a simplified approach. It was shown that amplification functions for specific sites in Switzerland with a quarter-wavelength velocity profile could be reconstructed using the correlation relations defined in this study. The general trend of the amplification functions was recovered when compared to those derived from the SH transfer function for real sites. The reconstructed amplification relations provide a useful alternative method for assessing the site amplification in the absence of earthquake recordings without the necessity of using SH-wave modeling. However, there is space for improvement when the influence of very strong velocity contrasts is included. The uncertainties in the resulting amplification function were taken into account. They are mostly induced by the limited measurement dataset. I am confident that including additional data will improve the statistics. It is therefore planned to perform additional measurements at seismological station sites for which amplification functions are available from spectral modeling.

Figures and Tables

List of Figures

1.1	Signal identification using classical beamforming	17
1.2	Signal identification using high-resolution beamforming	21
1.3	Example of three-component f - k processing on synthetics	24
1.4	Maxima picking on the slowness-azimuth plane	25
1.5	Ellipticity values in three dimensions	26
1.6	Statistical analysis of ellipticity values	27
1.7	Selected receiver configurations	31
1.8	Dispersion and ellipticity of the model M2.1	34
1.9	Dispersion and ellipticity of the model M10.2	35
1.10	Dispersion and ellipticity of the model M11.2	37
1.11	Array measurement location in Visp	38
1.12	Single-station H/V spectral ratios in Visp	39
1.13	Dispersion and ellipticity of the Visp array	41
2.1	Historical evolution of the city of Lucerne	49
2.2	Ambient noise measurements in the city of Lucerne	50
2.3	Example of the orientation error	53
2.4	Noise-wavefield decomposition with wavelet transform	56
2.5	SH to PSV contribution ratio of synthetics	57
2.6	Example of wavelet based H/V ratio in Lucerne	58
2.7	Ensemble of all H/V curves measured in Lucerne	59
2.8	SH to PSV contribution ratios in the Lucerne area	60
2.9	Ellipticity- f_0 map of Lucerne	61
2.10	Wave-field decomposition using f - k	63
2.11	Summary of dispersion information	64
2.12	Comparison with small arrays	65
2.13	Ellipticity from three-component array analysis	66

2.14	Wavelet H/V spectral ratio from the SBB array	67
2.15	Inverted Vs and Vp velocity models	69
2.16	Combined inversion of dispersion and ellipticity	70
2.17	Gradient velocity profile approximation	72
2.18	Inverting the bedrock depth and velocity	74
2.19	Globally inverting the ellipticity peaks	75
2.20	Correlation between ellipticity and bedrock depth	77
2.21	Bedrock depths from ellipticity	78
2.22	SH-wave transfer function amplification model	80
2.23	Maximum expected amplification at f_0	82
2.24	f_0 -Ell to f_0 -SH comparison	83
2.25	Quarter-wavelength amplification function	84
2.26	Quarter-wavelength amplification map	85
3.1	Mixed active/passive acquisition survey	92
3.2	Automatic triggering of the reference time	94
3.3	Multiple shots detection	95
3.4	Wavelet spectrogram of the four shots	96
3.5	Travel time correction of the wavelet transform	98
3.6	Power-spectrum search over source time	101
3.7	Raised-cosine mother wavelet	102
3.8	Wavelet transform comparison	103
3.9	Mother wavelets comparison	104
3.10	Frequency-velocity spectrum: SH component	106
3.11	Frequency-velocity spectrum: PSV component	107
3.12	Power-spectrum comparison	108
3.13	Array geometry for the passive and active acquisition	109
3.14	Results of the Lucerne test: vertical and radial	110
3.15	Comparison between active and passive seismic	111
4.1	Location of the 27 PEGASOS stations	116
4.2	Velocity profiles from the 27 PEGASOS stations	119
4.3	Example of quarter-wavelength velocity profile	121
4.4	Residual misfit $\hat{\Omega}_{ij}$	126
4.5	Amplification function from spectral modelling	127
4.6	Velocity vs. amplification correlations	129
4.7	Quadratic residuals from the comparison	130
4.8	Quarter-wavelength representation of the reference	130
4.9	Reconstruction of the reference velocity profile	131
4.10	Comparison between reference profiles (1)	134

4.11 Comparison between reference profiles (2) 135
4.12 Comparison between reference profiles (3) 136
4.13 Amplification function of the reference 137
4.14 Comparison between amplification functions (1) 138
4.15 Comparison between amplification functions (2) 139
4.16 Amplification level variability 140
4.17 Generic amplification functions form correlations 142
4.18 Distribution of the array measurements in Switzerland 157

List of Tables

1.1 Model parameters of the ambient noise synthetics 30
3.1 Parameters of the active seismic synthetics 105
4.1 Mean amplification factors from average velocity 141

Appendix

The database of average V_s velocity

Numerous single station and array measurements of ambient vibration have been carried out in this PhD project. The results from all these measurements, together with the results obtained from previous studies, were collected in a homogeneous site-characterization database. The database includes a selection of the most characteristic velocity profiles for the investigated sites, the average velocities using travel time averaging over depth (5-10-15-20-25-30-40-50-75-100-150m) and quarter-wavelength representation (from 0.5 to 50Hz) and the V_{s30} derived from the slope-topography using the Wald and Allen (2007) relationships. The database also includes the modeled amplification functions using both the SH transfer function formalism and the quarter-wavelength approximation. The integration of additional parameters that characterize the sites is under development, like the empirical amplification factors from spectral modeling. In the following we present an extraction of this database.

Station Name	Station parameters									
	Coordinates		Vs-Slope	Vs-z (m/s)			QWL-Vs (m/s)			
	X(m)	Y(m)	m/s	10m	30m	50m	0.5Hz	1Hz	5Hz	10Hz
Aesch	611405	256882	596	163	247	307	1179	542	143	136
Allschwil1	606296	266264	391	231	320	379	953	502	227	215
Allschwil2	606782	266306	361	222	294	333	865	422	211	199
Augusta	620538	264248	382	551	461	577	2507	1996	474	528
Beznau	659553	267347	400	513	594	694	2139	1436	586	505
BOURR1	584274	249358	602	331	509	648	2224	1427	448	288
BOURR2	584556	249446	709	279	477	631	2460	1796	380	152
ABRA2	596572	120798	297	715	741	748	822	756	744	732
ABRAL	596652	120797	297	473	586	637	786	738	564	459
ABRAS	596626	120946	297	809	809	809	2076	809	809	809
Bruderholz2	610949	264289	369	226	293	346	805	453	218	211
Dornach	613258	258584	527	492	550	549	1643	1002	522	480
Ergolz1	622690	257939	475	523	644	702	2144	1430	642	528
ErgolzN	621522	261704	327	404	620	793	2572	2136	621	373
ErgolzS	622947	259080	394	336	482	583	2108	1334	401	305
GoesgenInnen	639787	246281	380	375	489	712	2604	2160	391	369
Grenzach	617837	265979	449	301	461	596	2356	1338	393	217
Hard1	615815	266015	358	421	449	492	2307	1596	438	422
Kannenfeld	609940	268301	305	226	365	397	1234	536	226	226
Kannen	609950	268350	305	391	414	427	1583	558	406	388
Lucerne	666322	210986	384	121	192	248	702	300	117	116
AMAR2	572901	105460	692	269	392	462	1971	743	288	263

AMART	573795	107799	306	174	229	269	330	293	162	139
Mels	751159	211995	473	195	255	354	1638	796	194	194
AMURR	561592	126203	205	286	289	308	713	335	286	286
Otterbach	612497	269609	245	277	418	469	1126	604	350	218
PrattelnE	619590	263259	501	295	447	542	2061	1229	352	253
PrattelnM	619090	263087	501	395	470	586	2398	1834	353	313
Reinach1	611257	258711	357	380	463	474	1322	529	446	363
ASAIL	580504	112500	258	330	330	334	357	342	330	330
SARG	661902	194548	484	380	614	672	1693	1217	599	368
SBAE	613176	269178	220	255	375	454	1155	681	280	228
SABF	611562	270322	289	268	378	429	1301	552	287	242
SBAJ	610767	268550	311	379	421	471	1378	600	381	329
SBAP	609334	269033	306	260	383	432	1692	687	276	224
SBAT	610877	267592	362	320	380	404	1103	514	343	312
SBEG	617012	268939	568	311	439	618	2352	1778	315	266
SBIF	614247	267127	292	331	437	509	1127	717	378	296
SBIS	610741	265675	361	300	378	427	1312	722	323	270
Schuetzenmatte	610252	266882	276	330	426	479	1329	559	363	310
ASIES	608468	126224	426	415	448	527	1350	1111	423	410
ASIO1	593768	120248	760	283	483	676	2789	2276	357	262
ASIO2	593279	119538	492	401	401	401	485	430	401	401
ASIOM	594073	119796	318	729	729	734	980	795	677	678
ASIOO	595647	120054	543	864	863	773	766	714	820	861
ASIOV	594276	120398	621	592	1138	1608	4057	3895	2577	929
SLE	679132	290980	534	249	398	543	2104	1444	276	207

SMAV	572851	105486	692	269	392	462	1971	743	288	263
SMZW	615574	266278	358	444	484	515	2334	1733	473	444
Baeumli	614040	268770	276	427	464	504	1471	701	444	426
Reinach	612515	262260	427	502	523	571	1194	807	517	501
SULZ	650686	264268	619	952	1035	1078	1779	1205	1082	1022
AVETL	588052	118331	214	163	247	276	434	326	158	158
AVIS2	633923	127856	760	229	230	291	966	376	229	229
Wyhlen	619742	266551	566	518	678	833	2646	2253	703	529
YverdonA2	538762	180909	205	207	260	288	829	316	175	170
ZUR	686250	247080	614	374	635	806	1909	1459	658	354

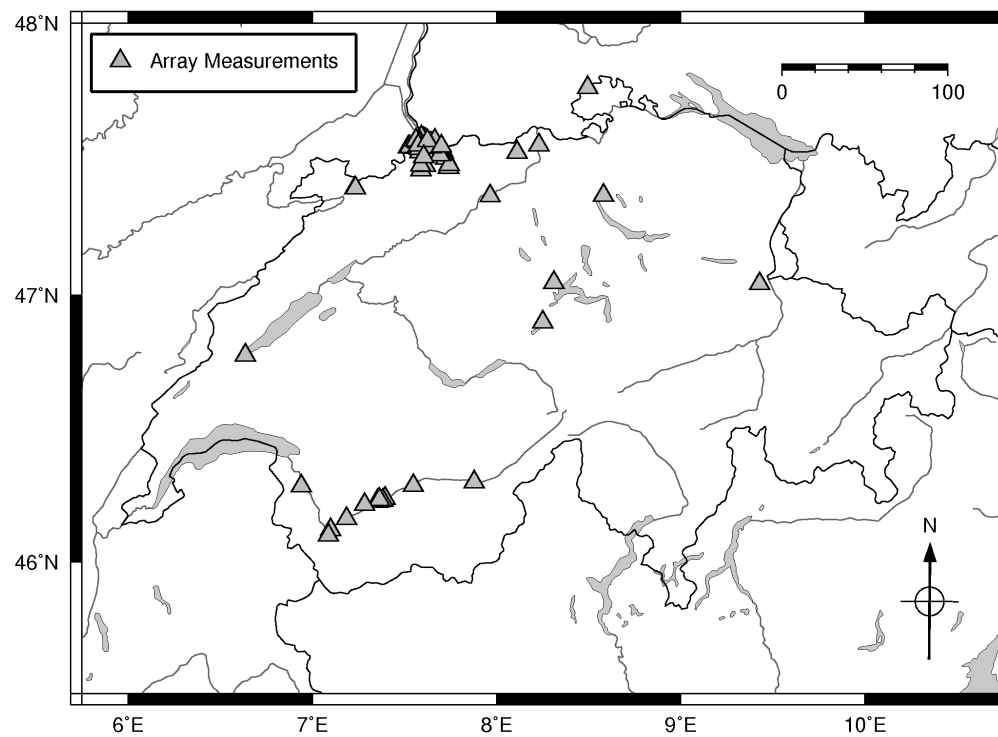


Figure 4.18: Distribution of the array measurements of ambient vibration used to compile the database of average V_s velocity for Switzerland.

Bibliography

- C.-P. Abbiss. Seismic amplification-mexico city. *Earthquake Engineering and Structural Dynamics*, 18:79–88, 1989.
- K. Aki. Local site effects on weak and strong motion. *Tectonophysics*, 218: 93–111, 1993.
- K. Aki and P.-G. Richards. Quantitative seismology. theory and methods. *W.H. Freeman and Company, New York*, 1980.
- S. Akkar and J.-J. Bommer. Prediction of elastic displacement response spectra in europe and the middle east. *Earthquake Engineering and Structural Dynamics*, 36:1275–1301, 2007.
- D. Albarello and E. Lunedei. Alternative interpretations of horizontal to vertical spectral ratios of ambient vibrations: new insights from theoretical modelling. *Bull. Earthquake Eng.*, DOI 10.1007/s10518-009-9110-0, 2009.
- J.-G. Anderson and S.-E. Hough. A model for the shape of the fourier amplitude spectrum of acceleration at high frequencies. *Bull. Seism. Soc. Am.*, 74:1969–1993, 1984.
- H. Arai and K. Tokimatsu. S-wave velocity profiling by joint inversion of microtremor dispersion curve and horizontal-tovertical (h/v) spectrum. *Bull. Seism. Soc. Am.*, 95 (5):1766–1778, 2005.
- H. Arai and K. Tokimatsu. Three-dimensional v-s profiling using microtremors in kushiro, japan. *Earthquake Engineering and Structural Dynamics*, 37: 845–859, 2008.
- M.-W. Asten. The use of microseisms in geophysical exploration. *PhD thesis, Macquarie University, Australia*, 1976.

- M.-W. Asten. On bias and noise in passive seismic data from finite circular array data processed using spac methods. *Geophysics*, 71, 6:153–162, 2006.
- M.-W. Asten and J.-D. Henstridge. Array estimators and the use of microseisms for reconnaissance of sedimentary basins. *Geophysics*, 49:1828–1837, 1984.
- M.-W. Asten, T. Dhu, and N. Lam. Optimised array design for microtremor array studies applied to site classification; observations, results and future use. *Proceedings of the 13th World Conference of Earthquake Engineering, Vancouver*, Paper 2903, 2004.
- G. Atkinson and R. Mereu. The shape of ground motion attenuation curves in south-eastern canada. *Bull. Seism. Soc. Am.*, 82:2014–2031, 1992.
- G.-M. Atkinson and D.-M. Boore. Earthquake ground-motion prediction equations for eastern north america. *Bull. Seism. Soc. Am.*, 96:2181–2205, 2006.
- M. Baer, N. Deichmann, J. Braunmiller, J. Clinton, S.-D. Husen, D. Giardini, P. Kästli, U. Kradolfer, and S. Wiemer. Earthquakes in switzerland and surrounding regions during 2006. *Eclogae Geologicae Helvetiae*, 100 (3): 517–528, 2007.
- P.-Y. Bard and M. Bouchon. The two-dimensional resonance of sediment-filled valleys. *Bull. Seism. Soc. Am.*, 75 (2):519–541, 1985.
- P.-Y. Bard, M. Campillo, F.-J. Chavez-Garcia, and F.-J. Sanchez-Sesma. Strong ground motion in mexico city during the great michoacan earthquake. part b: A theoretical investigation of large- and small-scale amplification effects. *Earthquake Spectra*, 4:609–633, 1988.
- Basler and Partner. Sicherheitsbericht für die stadt luzern. *Stadt Luzern, Sicherheitsdirektion*, 2007.
- D. Bindi, S. Parolai, H. Grosser, C. Milkereit, and S. Karakisa. Crustal attenuation characteristics in northwestern turkey in the range from 1 to 10 hz. *Bull. Seism. Soc. Am.*, 96:200–214, 2006.
- L. F. Bonilla, J.-H. Steidl, G.-T. Lindley, A.-G. Tumarkin, and R.-J. Archuleta. Site amplification in the san fernando valley, california: Variability of site-effect estimation using the s-wave, coda, and h/v methods. *Bull. Seism. Soc. Am.*, 87:710–730, 1997.

- S. Bonnefoy-Claudet, C. Cornou, P.-Y. Bard, F. Cotton, P. Moczo, J. Kristek, and D. Fäh. H/v ratio: a tool for site effects evaluation. results from 1d noise simulation. *Geophys. J. Int.*, 167:827–837, 2006a.
- S. Bonnefoy-Claudet, F. Cotton, and P.-Y. Bard. The nature of noise wavefield and its applications for site effects studies. a literature review. *Earth-Sci. Rev.*, 79:205–227, 2006b.
- S. Bonnefoy-Claudet, A. Köhler, C. Cornou, M. Wathelet, and P.-Y. Bard. Effects of love waves on microtremor h/v ratio. *Bull. Seism. Soc. Am.*, 98: 288–300, 2008.
- D. Boore. Simulation of ground motion using the stochastic method. *Pure and applied Geophysics.*, 160 (3-4):635–676, 2003.
- D.-M. Boore. Stochastic simulation of high-frequency ground motions based on seismological models of the radiated spectra. *Bull. Seism. Soc. Am.*, 73: 1865–1894, 1983.
- D.-M. Boore and W.-B. Joyner. Site amplifications for generic rock sites. *Bull. Seism. Soc. Am.*, 87:327–341, 1997.
- R.-D. Borchardt. Effects of local geology on ground motion near san francisco bay. *Bull. Seism. Soc. Am.*, 60:29–81, 1970.
- R.-D. Borchardt and J.-F. Gibbs. Effects of local geological conditions in the san francisco bay region on ground motions and the intensities of the 1906 earthquake. *Bull. Seism. Soc. Am.*, 66:467–500, 1976.
- J.-N. Brune. Tectonic stress and the spectra of seismic shear waves from earthquakes. *Geophys. Res. Lett.*, 75:4997–5010, 1970.
- J.-N. Brune. Correction: Tectonic stress and the spectra of seismic shear waves from earthquakes. *J. Geophys. Res.*, 76:5002, 1971.
- J.-P Burg. Maximum entropy spectral analysis. *37th Annual International SEG Meeting, Oklahoma City*, 1967.
- P. Campus and D. Fäh. Seismic monitoring of explosions: A method to extract information on the isotropic component of the seismic source. *Journal of Seismology*, 1:205–218, 1997.

- J. Capon. High resolution frequency wavenumber spectrum analysis. *Proc. IEEE*, 57:1408–1418, 1969.
- R.-R. Castro, J.-G. Anderson, and S.-K. Singh. Site response, attenuation and source spectra of s waves along the guerrero, mexico, subduction zone. *Bull. Seism. Soc. Am.*, 80:1481–1503, 1990.
- G. Dal Moro, E. Forte, M. Pìpan, and M. Sùgan. Velocity spectra and seismic-signal identification for surface-wave analysis. *Near Surface Geophysics*, 4: 243–251, 2006.
- I. Daubechies. The wavelet transform, time-frequency localization and signal analysis. *IEEE Transaction on. Information Theory*, 36, 1990.
- R. Dobry, I. Oweis, and A. Urzua. Simplified procedures for estimating the fundamental period of a soil profile. *Bull. Seism. Soc. Am.*, 66:1293–1321, 1976.
- J. Douglas, P. Gehl, L.-F. Bonilla, O. Scotti, J. Regnier, A.-M. Duval, and E. Bertrand. Making the most of available site information for empirical ground-motion prediction. *Bull. Seism. Soc. Am.*, 99 (3):1502–1520, 2009.
- S. Drouet, P. Triantafyllidis, A. Savvaidis, and N. Theodulidis. Comparison of site-effects estimation methods using the lefkas greece 2003 earthquake aftershocks. *Bull. Seism. Soc. Am.*, 98 (5):23492363, 2008.
- S. Drouet, F. Cotton, and P. Guguen. Vs30, kappa, regional attenuation and mw from accelerograms: application to magnitude 3 to 5 french earthquakes. *Geophys. J. Int.*, In press, 2010.
- B. Edwards and A. Rietbrock. A comparative study on attenuation and source-scaling relations in the kanto, tokai, and chubu regions of japan,using data from hi-net and kik-net. *Bull. Seism. Soc. Am.*, 99:doi: 10.1785/0120080292, 2009.
- B. Edwards, A. Rietbrock, J.-J. Bommer, and B. Baptie. The acquisition of source, path and site effects from micro-earthquake recordings using q tomography: Application to the uk. *Bull. Seism. Soc. Am.*, 98:19151935, 2008.
- B. Edwards, B. Allmann., D. Föh, and V. Poggi. Stochastic model for switzerland, swiss seismological service technical report: Sed/prp/r/006/20091130. *Swissnuclear Pegasos Refinement Project*, 2009.

- B. Endrun. Love wave contribution to the ambient vibration h/v amplitude peak observed with array measurements. *Journal of Seismology*, doi:10.1007/s10950-010-9191-x, 2010.
- D. Fäh, F. Kind, and D. Giardini. A theoretical investigation of average h/v ratios. *Geophys. J. Int.*, 145:535–549, 2001.
- D. Fäh, F. Kind, and D. Giardini. Inversion of local s-wave velocity structures from average h/v ratios and their use for the estimation of site-effects. *Journal of Seismology*, 7:449–467, 2003.
- D. Fäh, G. Stamm, and H.-B. Havenith. Analysis of three-component ambient vibration array measurements. *Geophys. J. Int.*, 172:199–213, 2008.
- D. Fäh, S. Fritsche, V. Poggi, G. Gassner-Stamm, P. Kstli, J. Burjanek, P. Zweifel, S. Barman, J. Clinton, L. Keller, P. Renault, and S. Heuberger. Determination of site information for seismic stations in switzerland, swiss seismological service technical report: Sed/prp/r/004/20090831. *Swissnuclear Pegasos Refinement Project*, 2009a.
- D. Fäh, M. Wathelet, M. Kristekova, H. Havenith, B. Endrun, G. Stamm, V. Poggi, J. Burjanek, and C. Cornou. Using ellipticity information for site characterisation. *NERIES JRA4 “Geotechnical Site Characterization”, taskB2-D4, final report*, 2009b.
- M. Farge. Wavelet transforms and their applications to turbulence. *Ann. Rev. Fluid Mech.*, 24:395–457, 1992.
- L.-Y. Faust. Seismic velocity as a function of depth and geologic time. *Geophysics*, 16 (2):192–206, 1951.
- W. Friederich and J. Dalkolmo. Complete synthetic seismograms for a spherically symmetric earth by a numerical computation of the greens function in the frequency domain. *Geophys. J. Int.*, 122:537–550, 1995.
- M. Gisler, D. Fäh, and P. Kästli. Historical seismicity in central switzerland. *Eclogae Geol. Helv.*, 97:221–236, 2004.
- P. Goupillaud, A. Grossman, and J. Morlet. Cycle-octave and related transforms in seismic signal analysis. *Geoexploration*, 23:85–102, 1984.

- E. Haghshenas, P.-Y. Bard, N. Theodulidis, and SESAME WP04 Team. Empirical evaluation of microtremor h/v spectral ratio. *Bull. Earthq. Eng.*, 6: 75–108, 2008.
- T. C. Hanks and R.-K. McGuire. The character of high frequency strong ground motion. *Bull. Seism. Soc. Am.*, 71:2071–2095, 1981.
- R.-I. Haubrich. Array design. *Bull. Seism. Soc. Am.*, 58, 3:977–991, 1968.
- H.-B. Havenith, D. Fäh, U. Pollom, and A. Roulle. S-wave velocity measurements applied to the seismic microzonation of basel, upper rhine graben. *Geophys. J. Int.*, 170:346–358, 2007.
- K.-G. Hinzen, B. Weber, and F. Scherbaum. On the resolution of h/v measurements to determine sediment thickness, a case study across a normal fault in the lower rhine embayment, germany. *Journal of Earthquake Engineering*, 8 (6):909–926, 2004.
- Y. Hisada. An efficient method for computing green’s functions for a layered half-space with sources and receivers at close depth. *Bull. Seism. Soc. Am.*, 84:1456–1472, 1994.
- M. Horike. Inversion of phase velocity of long-period microtremors to the s-wave-velocity structure down to the basement in urbanized areas. *J. Phys. Earth*, 33:59–96, 1985.
- S. Husen, E. Kissling, N. Deichmann, S. Wiemer, D. Giardini, and M. Baer. Probabilistic earthquake location in complex three-dimensional velocity models: Application to switzerland. *J. Geophys. Res.*, 108 (B2), 2003.
- S. Ide, G.-C. Beroza, S.-G. Prejean, and W.-L. Ellsworth. Apparent break in earthquake scaling due to path and site effects on deep borehole recordings. *J. Geophys. Res.*, 108(B5):2271, doi:10.1029/2001JB001617, 2003.
- D. Jongmans, M. Ohrnberger, and M. Wathelet. Recommendations for quality array measurements and processing. *Final Report of the SESAME Project, WP13*, 2005.
- W.-B. Joyner, R.-E. Warrick, and T.-E. Fumal. The effect of quaternary alluvium on strong ground motion in the coyote lake, california, earthquake of 1979. *Bull. Seism. Soc. Am.*, 71:1333–1349, 1981.

- H. Kawase. Site effects on strong ground motions, international handbook of earthquake and engineering seismology, part b. *W.H.K. Lee and H. Kanamori (eds.), Academic Press, London*, 6:1013–1030, 2006.
- F. Kind, D. Fäh, and D. Giardini. Array measurements of s-wave velocities from ambient vibrations. *Geophys. J. Int.*, 160:114–126, 2005.
- L. Knopoff. A matrix method for elastic wave problems. *Bull. Seism. Soc. Am.*, 54:431, 1964.
- S.-M. Kogon. Eigenvectors, diagonal loading and white noise gain constraints for robust adaptive beamforming. *Signals, Systems and Computers*, pages 1853–1857, 2003.
- A. Köhler, M. Ohrnberger, F. Scherbaum, M. Wathelet, and C. Cornou. Assessing the reliability of the modified three-component spatial autocorrelation technique. *Geophys. J. Int.*, 168 (2):779–796, 2007.
- K. Konno and T. Omachi. Ground motion characteristics estimated from spectral ratio between horizontal and vertical components of microtremors. *Bull. Seism. Soc. Am.*, 88:228–241, 1998.
- M. Krystek and M. Anton. A weighted total least-squares algorithm for fitting a straight line. *Measurement Science & Technology.*, 18:3438–3442, 2008.
- C. Lachet and P.-Y. Bard. Numerical and theoretical investigations on the possibilities and limitations of nakamura’s technique. *J. Phys. Earth*, 42: 377–397, 1994.
- R.-T. Lacoss, E.-J. Kelly, and M.-N. Toksz. Estimation of seismic noise structure using arrays. *Geophysics*, 34:21–38, 1969.
- J.-M. Lees and J. Park. Multiple-taper spectral analysis: A stand-alone c-subroutine. *Computers & Geosciences*, 21:199–236, 1995.
- T.-M.-C. Li, J.-F. Ferguson, E. Herrin, and H.-B. Durham. High-frequency seismic noise at lajitas, texas. *Bull. Seism. Soc. Am.*, 74:2015–2033, 1984.
- P.-G. Malischewsky and F. Scherbaum. Love’s formula and h/v-ratio (ellipticity) of rayleigh waves. *Wave motion*, 40:57–67, 2004.
- T. Marzetta. A new interpretation for capon’s maximum likelihood method of frequency-wavenumber spectral estimation. *Proc. of. ICASSP 84*, 31: 445–449, 1983.

- G.-A. McMechan and M.-J. Yedlin. Analysis of dispersive wave by wave field transformation. *Geophysics*, 46:869–874, 1981.
- Mengis and Lorenz AG. Geotechnik geologie hydrogeologie, lucerne. *Missing Link*, 2007a.
- Mengis and Lorenz AG. Geotechnik geologie hydrogeologie, lucerne. *Geologische Karte Luzern, unpublished*, 2007b.
- Y. Nakamura. A method for dynamic characteristics estimation of subsurface using microtremor on the ground surface. *Rep. Railway Tech. Res. Inst.*, 30,1:25–33, 1989.
- M. Nogoshi and T. Igarashi. On the amplitude characteristics of microtremors, part 2 (in japanese with english abstract). *J. Seism. Soc. Japan*, 24:26–40, 1971.
- G. Nolet and G.-F. Panza. Array analysis of seismic surface waves: limits and possibilities. *Pure and Applied geophysics*, 114:776–790, 1976.
- H. Okada. The microseismic survey method: Society of exploration geophysicists of japan. translated by koya suto, geophysical monograph series, no. 12,. *Society of Exploration Geophysicists, Tulsa*, 2003.
- C.-B. Park, R.-D. Miller, and J. Xia. Multichannel analysis of surface waves. *Geophysics*, 64:800–808, 1999.
- C.-B. Park, R.-D. Miller, N. Ryden, J. Xia, and J. Ivanov. Combined use of active and passive surface waves. *Journal of Environmental and Engineering Geophysics*, 10, 3:323–334, 2005.
- J. Park, C.-R. Lindberg, and F.-L. Vernon. Multitaper spectral analysis of high frequency seismograms. *J. Geophys. Res*, 92:12675–12684, 1987.
- S. Parolai, P. Bormann, and C. Milkereit. New relationships between vs, thickness of sediments, and resonance frequency calculated by the h/v ratio of seismic noise for the cologne area (germany). *Bull. Seism. Soc. Am.*, 92 (6): 2521–2527, 2002.
- S. Parolai, D. Bindi, M. Baumbach, H. Grosser, C. Milkereit, S. Karakisa, and S. Zbnl. Comparison of different site response estimation techniques using aftershocks of the 1999 izmit earthquake. *Bull. Seism. Soc. Am.*, 94: 1096–1108, 2004.

- S. Parolai, M. Picozzi, S.-M. Richwalski, and C. Milkereit. Joint inversion of phase velocity dispersion and h/v ratio curves from seismic noise recordings using a genetic algorithm, considering higher modes. *Geophys. Res. Lett.*, 32, 1, L01303, 2005.
- V. Poggi and D. Fäh. Estimating rayleigh wave particle motion from three-component array analysis of ambient vibrations. *Geophys. J. Int.*, 180:251–267, 2010.
- V. Poggi, D. Fäh, J. Burjanek, and D. Giardini. The use of rayleigh wave ellipticity for site-specific hazard assessment and microzonation. application to the city of lucerne, switzerland. *Geophys. J. Int.*, In review, 2011.
- R. Pozo. Template numerical toolkit. Available from: <http://math.nist.gov/tnt/>, [cited May 2009], 2004.
- T.-L. Pratt, T.-M. Brocher, C.-S. Weaver, K.-C. Miller, A.-M. Trhu, K.-C. Creager, R.-S. Crosson, and C.-M. Snelson. Amplification of seismic waves by the seattle basin, northwestern u.s. *Bull. Seism. Soc. Am.*, 93:533–545, 2003.
- W.-H. Press, S.-A. Teukolsky, W.-T. Vetterling, and B.-P. Flannery. Numerical recipes in c: The art of scientific computing second edition. *Cambridge University Press*, pages pp. 278–281; pp. 288–290; pp. 417–424; and pp. 515–518, 1997.
- M.-J. Randal. The spectral theory of seismic sources. *Bull. Seism. Soc. Am.*, 63:1133–1144, 1973.
- M. Raoof, R. Herrmann, and L. Malagnini. Attenuation and excitation of three-component ground motion in southern california. *Bull. Seism. Soc. Am.*, 89:888–902, 1999.
- P. Renault, S. Heuberger, and N.-A. Abrahamson. Pegasos refinement project: An improved psha for swiss nuclear power plants. *Proceedings of 14ECEE - European Conference of Earthquake Engineering, Ohrid, Republic of Macedonia*, Paper ID 991, 2010.
- A. Rietbrock. P wave attenuation structure in the fault area of the 1995 kobe earthquake. *J. Geophys. Res.*, 106:4141–4154, 2001.

- J.-M. Roesset. Fundamentals of soil amplification. *Seismic Design for Nuclear Power Plants*, R. J. Hansen, Editor, M.I.T. Press, Cambridge, Mass., pages 183–244, 1970.
- S.-M. Romero and G.-J. Rix. Ground motion amplification of soils in the upper mississippi embayment. report no. git-cee/geo-01-1. *Georgia Institute of Technology, Atlanta, Georgia*, 2001.
- D. Roten, D. Fäh, C. Cornou, and D. Giardini. Two-dimensional resonances in alpine valleys identified from ambient vibration wavefields. *Geophys. J. Int.*, 165:889–905, 2006.
- D. Roten, D. Fäh, K.-B. Olsen, and D. Giardini. A comparison of observed and simulated site response in the rhöne valley. *Geophys. J. Int.*, 173:958–978, 2008.
- F. Scherbaum. Combined inversion for the three-dimensional q structure and source parameters using microearthquake spectra. *J. Geophys. Res*, 95: 12423–12438, 1990.
- F. Scherbaum, K.-G. Hinzen, and M. Ohrnberger. Determination of shallow shear wave velocity profiles in the cologne germany area using ambient vibrations. *Geophys. J. Int.*, 152:597–612, 2003.
- R.-O. Schmidt. Multiple emitter location and signal parameter estimation. *IEEE Trans. Antennas Propagation*, AP-34:276–280, 1986.
- J. Schuler. Joint inversion of surface waves and refracted p- and s-waves. *Master Thesis, Swiss Federal Institute of Technology (ETH), Zurich*, 2008.
- G. Schwarz-Zanetti, D. Fäh, R. Schibler, V. Masciadri, P. Kästli, and D. Giardini. The earthquake in unterwalden and the rockslide from the bürgenstock into lake lucerne on september 18, 1601. *Eclogae geol. Helv.*, 96:441–450, 2003.
- N.-M. Shapiro, M. Campillo, L. Stehly, and M.-H. Ritzwoller. High-resolution surface-wave tomography from ambient seismic noise. *Science*, 307, Issue 5715:1615–1618, 2005.
- Y. Sheng. Wavelet transform, in "the transforms and applications handbook". *A.D. Poularikas Ed. Chap. 10, CRC and IEEE Press, Boca Raton*, 1995.

- L.-H. Sibul. Application of singular value decomposition to adaptive beamforming. *Proc. of ICASSP 84*, 9:750–753, 1984.
- J.-H. Steidl, A.-G. Tumarkin, and R.-J. Archuleta. What is a reference site? *Bull. Seism. Soc. Am.*, 86:1733–1748, 1996.
- K.-H. Stokoe and S. Nazarian. Use of rayleigh wave in liquefaction studies. *Proc. Of the Measurement and Use of shear wave velocity for evaluating dynamic soil properties, ASCE, N.Y.*, pages 1–17, 1985.
- M. Strasser, F. Anselmetti, D. Fäh, D. Giardini, and M. Schnellmann. Magnitudes and source areas of large prehistoric northern alpine earthquakes revealed by slope failures in lakes. *Geology*, 34 (12):1005–1008, 2006.
- C. Strobbia. Surface wave method: acquisition, processing and inversion. *PhD thesis, Politecnico di Torino*, 2003.
- T. Takahashi and H. Suzuki. A study on technical methodologies underpinning site selection process for geological disposal. a study on site screening system for geological disposal. microtremor measurements. radioactive waste management center (rwnc). *Nagra project report*, pages 01–28, 2001.
- K. Tokimatsu. Geotechnical site characterization using surface waves. *In Proc. 1st Intl. Conf. Earthquake Geotechnical Engineering*, pages 1333–1368, 1997.
- M. Wathelet. Array recordings of ambient vibrations: surface-wave inversion. *PhD thesis, University of Liege, Belgium*, 2005.
- M. Wathelet, D. Jongmans, M. Ohrnberger, and S. Bonnefoy-Claudet. Array performances for ambient vibrations on a shallow structure and consequences over vs inversion. *Journal of Seismology*, 12, 1:1–19, 2008.
- J.-W. Woods and P.-L. Lintz. Plane waves at small arrays. *Geophysics*, 38: 1023–1041, 1973.
- J. Xia, R.-D. Miller, and C.-B. Park. Estimation of near-surface shear-wave velocity by inversion of rayleigh waves. *Geophysics*, 64:691–700, 1999.
- J. Xia, Y. Xu, and R.-D. Miller. Generating an image of dispersive energy by frequency decomposition and slant stacking. *Pure and Applied geophysics*, 164:941–956, 2007.

- H. Yamanaka, M. Takemura, H. Ishida, and M. Niwa. Characteristics of long-period microtremors and their applicability in exploration of deep sedimentary layers. *Bull. Seism. Soc. Am.*, 84, 6:1831–1841, 1994.
- J. Yu and J. Haines. The choice of reference sites for seismic ground motion amplification analyses: case study at parkway, new zealand. *Bull. Seism. Soc. Am.*, 93:713–723, 2003.
- D.-J. Zywicki. Advanced signal processing methods applied to engineering analysis of seismic surface waves. *PhD thesis, Georgia Institute of Technology, Atlanta, USA*, 1999.

Curriculum Vitae

PERSONAL INFORMATION

Surname/First name: Poggi Valerio

Address: Wehntalerstrasse 584, 8046 Zurich, Switzerland

E-mail: poggi@sed.ethz.ch

Date of birth: September 19, 1976

Nationality: Italian

EDUCATION

2006-2011: Doctoral student, Inst. of Geophysics, ETH Zurich, Switzerland.

April 2006: Degree in *Geology* at the *Universita' degli Studi di Milano* (Italy), with marks 110/110 cum Laude.

July 1995: School-leaving certificate awarded in a 5 years scientific college in Milano (Italy).

SUMMER SCHOOLS

September 2007: 16th CINECA summer school of parallel computing. Bologna, Italy.

July 2007: Using Ambient Vibration Array Techniques for Site Characterization. Algiers, Algeria.

LANGUAGES

Italian: Mother tongue.

English: Fluent.

German: Basic.

COMPUTING SKILLS

Platform: GNU Linux, Mac OSX, Windows operative systems.

Programming: ANSI C, C++, MPI, GTK+, MATLAB, Bash.

PUBLICATIONS

- 1 - **Poggi, V., Edwards, B., Fäh, D. 2010.** Derivation of a Reference Shear-Wave Velocity Model from Empirical Site Amplification. *Bull. Seim. Soc. Am.*, DOI: 10.1785/0120100060.
- 2 - **Burjánek, J., Gassner-Stamm, G., Poggi, V., Moore, J. R., Fäh, D. 2010.** Ambient vibration analysis of an unstable mountain slope, *Geophys. J. Int.*, Volume 180 Issue 2, 820-828.
- 3 - **Poggi, V., Fäh, D., 2009.** Estimating Rayleigh wave particle motion from three-component array analysis of ambient vibrations. *Geophys. J. Int.*, Volume 180 Issue 1, 251-267.
- 4 - **Poggi, V., Fäh, D., Burjanek, J., Giardini, D., 2010.** The use of Rayleigh wave ellipticity for site-specific hazard assessment and microzonation. An application to the city of Luzern (Switzerland). Submitted to *Geophys. J. Int.*
- 5 - **Bard, P.-Y., Cadet, H., Endrun, B., Hobiger, M., Renalier, F., Theodulidis, N., Ohrnberger, M., Fäh, D., Sabetta, F., Teves-Costa, P., Duval, A.-M., Cornou, C., Guillier, B., Wathelet, M., Savvaidis, A., Köhler, A., Burjanek, J., Poggi, V., Gassner-Stamm, G., Havenith, H. B., Hailemichael, S., Almeida, J., Rodrigues, I., Veludo, I., Lacave, C., Thomassin, S. and Kristekova, M. 2010.** From non-invasive site characterization to site amplification: recent advances in the use of ambient vibration measurements. In: M. Garevski, A. Ansal (eds.), *Earthquake Engineering in*

Europe. Geotechnical, Geological, and Earthquake Engineering, 17, 105-123, Springer, doi:10.1007/97890481954425. (book chapter)

- 6 - **Poggi, V., and D Fäh**, T-f-k analysis of surface waves using the continuous wavelet transform, to be submitted to *Pure and Applied Geophysics*

CONFERENCE PRESENTATIONS

- 1 - **Poggi, V., Edwards, B., Fäh, D.**, Derivation of a Reference Bedrock Model for Switzerland from Empirical Site Amplification and Direct Measurements, 32th General assembly of the European Seismological Commission (ESC), Montpellier (France), 6-10 September 2010.
- 2 - **Poggi, V., Fäh, D., Burjanek, J., Giardini, D.**, The use of Rayleigh wave ellipticity for sitespecific hazard assessment and microzonation with application to the city of Luzern, Switzerland, 32th General assembly of the European Seismological Commission (ESC), Montpellier (France), 6-10 September 2010.
- 3 - **Poggi, V., Fäh, D.**, The use of Rayleigh wave ellipticity for site-specific hazard assessment and microzonation with application to the city of Luzern, Switzerland. ETH Institute colloquium, Zurich, (CH), 17 November 2009.
- 4 - **Poggi V., Fäh D.**, Estimating Rayleigh Wave Particle Motion from Three-Component Array Analysis of Ambient Vibrations and Its Application to Seismic Local Response Analysis, Annual meeting of the Seis. Society of America (SSA), Monterey (CA), 8-10 April 2009.
- 5 - **Poggi, V., Fäh, D.**, Assessing the 1d velocity structure of Visp using three components hv-fk analysis of ambient vibration. COGEAR 1st annual meeting, Visp (CH), 28-30 January 2009.
- 6 - **Poggi, V., Fäh, D.**, Rayleigh wave particle motion estimation through three-component array analysis of ambient vibrations, 31th General assembly of the European Seismological Commission (ESC), Crete (Greece), 7-12 September 2008.

Acknowledgments

Dear reader, I know this page is at the end of the thesis, but I hope you start reading from here. If something useful or interesting is written in this thesis, it's also due to the people I mention here.

First of all, I would like to express my gratitude to Dr. Donat Fäh, my supervisor, for his endless patience in assisting, supporting and guiding me throughout all these years. He gave me all the time to follow my interests and a lot of freedom in choosing my personal research strategy. Thanks for believing in me.

I would like also to thank Prof. Domenico Giardini for referring this thesis and for making this Ph.D. project possible. He gave me the opportunity to work on the field of engineering seismology.

I am grateful to Dr. Pierre-Yves Bard for accepting to be co-examiner of this thesis. Thanks also to Cecile Cornou, Matthias Ohrnberger, Marc Wathelet and Miriam Kristekova for their invaluable collaboration in the project.

A special thanks to all my colleagues (and friends), together with I shared time in and out of the institute: Ben, Jan, Damiano, Steve, Carlo, Stefan, Philipp, Stefano, Clotaire, Monika, Hans, Gabriela G.S., Daniel. Thank you all for the fruitful scientific (and sometimes not-so-scientific) discussions. Thanks a lot to Gabriela S.Z. for the hours spent trying to teach me some german.

Thanks to my parents, Giovanna e Bruno. There is no need to explain why.

Lastly, and most importantly, I wish to thank Sonia. She guided me, supported me, encouraged me, put up with me, and loved me. To her I dedicate this thesis.

Zurich, January 2011

